Evaluating degraded ballast and track geometry variability along a Canadian freight railroad through ballast maintenance records and ground-penetrating radar

by

Kirk Michael Scanlan

A thesis submitted in partial fulfillment of the requirements for the degree of

Doctor of Philosophy

in

Geotechnical Engineering

Civil and Environmental Engineering
University of Alberta

Abstract

The majority of track comprising Canada's large railway network is constructed on ballasted foundations. As such, the accumulation of fines within the void space between the ballast aggregate, referred to as ballast degradation, is considered to be a significant factor contributing to the development of long-term track geometry variability (roughness). The relationship is so prevalent that current maintenance practices designed to control the accumulation of fines within ballast are considered equivalent to the management of long-term track roughness. This spatial relationship between degraded ballast and increased long-term geometrical track roughness is based on laboratory test results and limited field evidence. A rigorous, subdivision-scale investigation into the effectiveness of current ballast degradation maintenance practices as well as the degree in which degraded ballast influences track geometry has yet to be performed.

As part of this research, the influence of ballast degradation on long-term trends in track geometry is investigated by analyzing historical ballast undercutting (renewal) records. As undercutting alters only the fines content within the ballast, while the remaining track components (subgrade, ties, rails, and fasteners) are not affected, any change in long-term track roughness can be associated with the improved ballast conditions. The importance of improved ballast degradation levels on long-term trends in track geometry is also contrasted between segments of track founded on different subgrade materials.

This research also investigates the spatial association between degraded ballast and prolonged or increasing track roughness using 400 megahertz (MHz) ground-penetrating radar (GPR) measurements of a 335 km-long section of Canadian heavy-haul railway. GPR is one of the only methods capable of generating ballast degradation levels across extended (100's of kilometer long) sections of track in a non-destructive and efficient manner. The methodologies employed

to infer ballast degradation from the GPR datasets are based on those gathered during a thorough literature review of current standard railway engineering practices.

The results of this research demonstrate that the management of ballast fines is a significant factor related to the management of long-term track geometry for sections of track constructed on mineral-based subgrades. However, for track constructed on relatively softer, organic subgrades, long-term reductions in track roughness after ballast renewal are not as prevalent. This result suggests that, from a subdivision-scale track geometry management perspective, the accumulation of fines within the ballast void space, while important, is not the only factor to consider when preparing ballast maintenance campaigns in response to observed track geometry variability.

The spatial association results derived from field measurements demonstrate no widespread, subdivision-scale correlation between track roughness and GPR-based ballast degradation estimates. Significant spatial correlations only exist when the datasets are compared at local scales (100's of meters). Numerical modelling of 400 MHz GPR measurements demonstrate that the attributes used to infer ballast degradation are ambiguous in the presence of variable track foundations (including variable ballast thicknesses, saturations, conductivities and subballast materials) and investigating spatial correlations in the field datasets at a local-scale attempts to limit that ambiguity. However, GPR attribute ambiguity continues to be problematic even at the local-scale as significant spatial correlations are rare. Improved correlation results may be achievable considering ballast degradation levels inferred from a joint interpretation of multiple GPR datasets utilizing multiple operating frequencies.

Preface

This is a "paper-format" style dissertation, with Chapters 3, 4, and 5 either accepted for publication or published as detailed below. Versions of the individual manuscripts as presented in this thesis may differ slightly from the published versions.

Chapter 3 is accepted (May 22 2017) for publication in the ASTM Selected Technical Papers 1605: Symposium on Railroad Ballast Testing and Properties as: Scanlan, K.M., Hendry, M.T., Martin, C.D., and Schmitt, D.R. "A Review of Methods for Estimating Ballast Degradation using Ground-Penetrating Radar".

Chapter 4 is published in the Proceedings of the Institution of Mechanical Engineers Part F: Journal of Rail and Rapid Transit as: Scanlan, K.M., Hendry, M.T., and Martin, C.D. "Evaluating the impact of ballast undercutting on the roughness of track geometry over different subgrade conditions", in press, online, DOI: 10.1177/0954409717720347.

Chapter 5 is published in the Proceedings of the Institution of Mechanical Engineers Part F: Journal of Rail and Rapid Transit as: Scanlan, K.M., Hendry, M.T., Martin, C.D., and Schmitt, D.R. "Evaluating the sensitivity of low-frequency ground-penetrating radar attributes to estimate ballast fines in presence of variable track foundations through simulation", in press, online DOI: 10.1177/0954409717710408.

Chapter 6 is accepted (December 12 2017) for publications in the Proceedings of the Institution of Mechanical Engineers Part F: Journal of Rail and Rapid Transit as: Scanlan, K.M., Hendry, M.T., Martin, C.D., and Schmitt, D.R. "The spatial correlation between track roughness and ground-penetrating radar inferred ballast degradation".

I was responsible for all data analysis, data interpretation, discussion, and manuscript composition. Dr. M.T. Hendry and Dr. C.D. Martin were involved in data collection, developing the concept for the dissertation, and as supervisors; each has reviewed all parts of the work. Dr. D.R. Schmitt was involved in developing the ground-penetrating radar concepts presented in Chapters 3, 5 and 6 and has also reviewed all components of this work.

Acknowledgement

I am extremely grateful to my supervisors Dr. Michael T. Hendry and Dr. C. Derek Martin, Associate Director and Director of the Canadian Rail Research Laboratory (CaRRL) respectively, and Dr. Doug R. Schmitt from the Department of Physics for their support, patience, and guidance throughout this research. The completion of this research would not have been possible without their tireless efforts.

Furthermore, this research would not have been possible without the support provided by CaRRL. CaRRL is funded by the Natural Sciences and Engineering Research Council of Canada (NSERC), Canadian Pacific Railway, Canadian National Railway, the Association of American Railways – Transportation Technology Center Inc., the National Research Council of Canada, Transport Canada and Alberta Innovates – Technology Futures. Sincere thanks to both Tom Edwards and Eddie Choi for their support during this research.

I am grateful to my fellow CaRRL students as well as those within the larger Geotechnical group for all their constructive feedback during various presentations and discussions and always being there as a welcome distraction. I would also like to thank Vivian Giang, Annette Busenius, and Sally Petaske; without whom numerous details and deadlines over the past four years would have fallen through the cracks.

I would also like to express my sincere and unending gratitude to my family. While you may not always understand what I am doing, the support you provide is fundamental to me seeing it through. Finally, to Anja; thank you for always being there, willing to listen to a presentation, act as a sounding board, or read a manuscript. I could not have done this without you.

To Nancy, Kevin, Jean, Bernard, Margaret, and Peter

Table of Contents

Abstract ii
Preface iv
Acknowledgement v
List of Figures xi
List of Tables xxi
Chapter 1: Introduction 1
1.1. Problem Description 2
1.2. Research Objectives 4
1.3. Description of the Study Site 5
1.4. Scope and Methodology 6
1.4.1. Review and Synthesis of the Relevant Literature regarding GPR as Applied to Ballast Degradation Studies 7
1.4.2. Investigating Ballast Degradation as a Dominant Factor Affecting Trends in Track Geometry 8
1.4.3. The Sensitivity of Ballast Degradation Estimates in the Presence of Variable Track Foundations 9
1.4.4. The Spatial Association between Rough Track and GPR-Inferred Degraded Ballast 10
1.5. Thesis Outline 11
1.6. References 12
Chapter 2: Literature Review 14
2.1. Track Geometry 14
2.1.1. Basic Measurements 14
2.1.2. Methods to Interpret Track Roughness 16
2.2. Ballasted Track Foundations 19
2.2.1. The Ballast Layer 20
2.2.2. Fundamentals of Ballast Degradation 23
2.2.3. Quantification of Ballast Degradation 26
2.3. Field Methods to Assess Ballast Degradation 28
2.3.1. Destructive Methods 28
2.3.2. Non-Destructive Methods 29
2.4. References 31
Chapter 3: A Review of Methods for Estimating Ballast Degradation using Ground-Penetrating Radar 35
3.1. Contribution of the Ph.D. Candidate 35

3.2. Abstract 35
3.3. Introduction 36
3.4. Fundamentals of Ground-Penetrating Radar 39
3.4.1. Electromagnetic Material Properties 39
3.4.2. GPR Signal Attenuation, Velocity, and Reflection 42
3.5. Effect of Ballast Degradation on GPR Signals 45
3.5.1. Low-Frequency GPR 45
3.5.2. High-Frequency GPR 47
3.6. GPR Interpretation Methods 49
3.6.1. Low-Frequency (<1 GHz) Methods 52
3.6.2. High-Frequency (>1 GHz) Methods 58
3.6.3. Comparison of Low- and High-Frequency Methods 62
3.7. Conclusions 63
3.8. Acknowledgments 65
3.9. References 65
Chapter 4: Evaluating the Impact of Ballast Undercutting on the Roughness of Track Geometry over Different Subgrade Conditions 71
4.1. Contribution of the Ph.D. Candidate 71
4.2. Abstract 71
4.3. Introduction 72
4.4. Datasets 74
4.5. Quantification of Track Roughness 78
4.6. Trends in Track Roughness 82
4.6.1. Expected Trends 82
4.6.2. Classification of Observed Trends 84
4.7. Classification Results and Discussion 87
4.7.1. Spatial Distribution of Roughness Classifications 87
4.7.2. Effect of Subgrade on Track Roughness 92
4.8. Conclusions 94
4.9. Acknowledgements 95
4.10. References 95
Chapter 5: Evaluating the sensitivity of low-frequency ground-penetrating radar attributes to estimate ballast fines in the presence of variable track foundations through simulation 99
5.1. Contribution of the Ph.D. Candidate 99

5.2. Abstract 99
5.3. Introduction 100
5.4. Effect of Ballast Degradation on Electromagnetic Material Properties 103
5.5. Estimating Ballast Degradation Levels from GPR Data 105
5.5.1. Propagation Velocity 105
5.5.2. Windowed Fourier Amplitude Spectrum Integral 106
5.5.3. Normalized Reflectivity 108
5.6. The Synthetic Track Foundation Model 109
5.7. EM Properties Assigned to the Synthetic Model 112
5.8. Preliminary Data Processing 116
5.9. Modeling Results and Discussion 119
5.9.1. Model Sensitivity 119
5.9.2. Propagation Velocity 121
5.9.3. Windowed Fourier Amplitude Spectrum Integral 123
5.9.4. Normalized Reflectivity 126
5.9.5. Similarity between the WFASI and Normalized Reflectivity GPR Attributes 128
5.10. Conclusions 132
5.11. Acknowledgements 134
5.12. References 134
Chapter 6: The Spatial Correlation between Track Roughness and Ground-Penetrating Radar Inferred Ballast Degradation 139
6.1. Contribution of the Ph.D. Candidate 139
6.2. Abstract 139
6.3. Introduction 140
6.4. Datasets 142
6.4.1. Track Geometry 143
6.4.2. Quantification of Track Roughness 145
6.4.3. GPR 147
6.4.4. Estimation of Ballast Degradation from the GPR Measurements 152
6.5. Combining the Track Geometry and GPR Datasets and Infrastructure Removal 155
6.6. Full Subdivision Comparison of Track Roughness and Ballast Degradation Estimate 157
6.7. Identifying Local Sections for Cross Correlation 162
6.8. Local Comparison of Running Roughness and WFASI 163

6.9. Conclusions 171
6.10. Acknowledgments 173
6.11. References 173
Chapter 7: Conclusions & Recommendations 179
7.1. Review and Synthesis of the Relevant Literature regarding GPR as Applied to Ballast Degradation Studies 179
7.2. Validating Ballast Degradation as a Dominant Factor Affecting Trends in Track Geometry 180
7.3. The Sensitivity of Ballast Degradation Estimates in the Presence of Variable Track Foundations 182
7.4. The Spatial Association between Rough Track and GPR-Inferred Ballast Degradation 183
7.5. Implications of this Study 184
7.6. Recommendations 185
References 188
Appendix A: Evaluating the Equivalency between Track Quality Indices and Minimum Track Geometry Threshold Exceedances along a Canadian Freight Railway 200
A.1. Contribution of the Ph.D. Candidate 200
A.2. Abstract 200
A.3. Introduction 201
A.4. Track Quality Indices 204
A.5. Analysis of the Track Geometry Data 207
A.6. Comparing Threshold Exceedances and TQI 210
A.7. Results and Discussion 212
A.8. Conclusion 216
A.9. Acknowledgements 217
A.10. References 217

List of Figures

Figure 1-1. Section of CN's Edson subdivision investigated as part of this research. The section is 335 km long and extends in a dominantly east-west direction between Stony Plain and Jasper..... 5

Figure 2-1. Principles of performing a MCO measurement. 16

Figure 2-2. Cross-section of a typical ballasted track foundation. 20

Figure 2-3. Particle size distributions for AREMA #4 and #24 ballast gradations after Li et al. (2016). 21

Figure 2-4. Illustrative results from a cyclic triaxial test of railway ballast demonstrating the accumulation of unrecoverable (plastic) axial strain until resilient (elastic) behaviour is observed after Li et al. (2016). Deformation in the elastic regime is characterized by the resilient modulus (M_r – Equation 2-3). 23

Figure 2-5. Experimental isotropic drained triaxial test results for various clay-degraded ballast samples with a 10 kPa confining stress after Indraratna et al. (2013). There is a clear reduction in ballast shear strength as clay particles accumulate (represented by a VCI increase) within the ballast..... 26

Figure 3-1. Basic GPR operating principles in a ballasted railway track foundation. 37

Figure 3-2. A propagating EM plane wave separated into its a) TE mode and b) TM mode components. 44

Figure 3-3. Variation in the normalized dimension (D_N) as a function of signal frequency and the relative dielectric permittivity of the ballast. Mie scattering dominates when D_N is approximately one. 48

Figure 3-4. Artificial normalized reflectivity profiles illustrating how the normalized reflectivity metric can be used to infer relative increased moisture retention in the ballast. The greater seasonal difference in the ballast beyond 0.4 km would be indicative of increased moisture retention relative to the ballast prior to 0.4 km. 53

Figure 3-5. Fundamental aspects of the attenuation interpretation for low-frequency GPR data; a) a reduced Fourier amplitude spectra integral in the presence of degraded ballast due to the increased signal attenuation and b) a quantitative calibration of the GPR attenuation metric with a ballast fines index after Silvast et al. (2010). 54

Figure 3-6. Labeled interpretation of example GPR data collected over a layered track foundation with a radar-detectable geosynthetic installed at the base of the ballast at 3.5 m. $\varepsilon_{r,ballast}$ can be estimated from the shape of the diffraction hyperbola. 56

Figure 3-7. Example wide-angle reflection and refraction (WARR) GPR survey; a) survey design and b) annotated results highlighting the reflected wave from which $\varepsilon_{r,ballast}$ can be estimated through curve fitting. 57

Figure 3-8. Procedure followed by Shao et al. (2011a) (solid line) and Shao et al. (2011b) (dashed line) to qualitatively differentiate between degraded and non-degraded ballast without strict reliance on estimating $\varepsilon_{r,ballast}$. 58

Figure 3-9. 2 GHz GPR profiles collected over a) clean ballast and b) degraded ballast after Al-Qadi et al. (2008b). GPR profiles collected over clean ballast exhibit stronger reflections and a more cluttered appearance due to Mie scattering. 59

Figure 3-10. Quantitative calibration of the descriptive statistics calculated from decomposed high-frequency GPR traces with the ballast fouling index after Shangguan et al. (2012). Larger statistic amplitudes are indicative of a more cluttered GPR signal and less degraded ballast. 60

Figure 3-11. Comparison of short time Fourier transform results for GPR traces acquired in a) clean ballast and b) layered clean and degraded ballast after Al-Qadi et al. (2010b). Increased signal attenuation in the degraded ballast leads to an absence of warm colours in the bottom half of the plot..... 62

Figure 4-1. AREMA #4 recommended particle grain size distribution for new ballast and example grain size distributions for ballast pre-renewal and post-renewal after Li et al. (2016). 73

Figure 4-2. Example repeated crosslevel [a) and d)], alignment [b) and e)], and surface [c) and f)] datasets collected over mineral [a)-c)] and organic [d)-f)] subgrades. Solid and dashed lines in b), c), e), and f) represent measurements for the left and right rail, respectively. 77

Figure 4-3. Variation in a) crosslevel, b) alignment, and c) surface standard deviation (σ) as a function of segment length..... 80

Figure 4-4. Trends in standard deviation (σ) calculated from the example track geometry data presented in Figure 2. Circles represent σ calculated for the segment between 0 and 60 m; squares for the segment between 60 and 120 m and triangles for the segment between 120 and 180 m. 82

Figure 4-5. The idealized standard deviation (σ) behavior derived from measured track geometry showing the effect of repeated tamping after Audley and Andrews (2013). 83

Figure 4-6. Trends in standard deviation (σ) showing a) a long-term reduction after ballast undercutting (Type I trends) and b) a temporary reduction after ballast undercutting but no long-term change (Type II trends). Stars indicate the interval between geometry surveys where the ballast renewal occurred. 85

Figure 4-7. Trends in standard deviation (σ) showing a) no notable reductions after ballast undercutting and no long-term change (Type III trends) and b) a long-term increase after ballast undercutting (Type IV trends). Stars indicate the interval between geometry surveys where the ballast renewal occurred. 86

Figure 4-8. Along track variation in the classification results for a) track crosslevel, b) track alignment, and c) track surface in undercut section one illustrated in d). 88

Figure 4-9. Along track variation in the classification results for a) track crosslevel, b) track alignment, and c) track surface in undercut section two illustrated in d). 89

Figure 4-10. Along track variation in the classification results for track crosslevel [a), e)], track alignment [b), f)], and track surface [c), g)] for undercut section three illustrated in d) and four illustrated in h). 90

Figure 4-11. Percentage of undercut segments belonging to each classification type for track constructed on subgrades where the dominant materials were a) mineral (till, sand, silt, and clay) and b) organic (peat). The total number of undercut segments represented in a) and b) are 87 and 25, respectively. 93

Figure 5-1. Typical ballasted track foundation structure and important ground-penetrating radar reflections (top-of-ballast, base-of-ballast, base of subballast and subgrade reflections). 101

Figure 5-2. Normalized Fourier amplitude spectra of two ground-penetrating radar traces, one recorded over clean ballast (solid line) and one over degraded ballast (dashed line), based on Silvast et al. (2010). Note the reduced integral area under the degraded ballast spectrum compared to the clean ballast spectrum. 108

Figure 5-3. Example gprMax model highlighting a 0.40 m thick ballast overlying a 0.30 m thick subballast with the transmitting and receiving antennas suspended 0.25 m above the ballast surface. 111

Figure 5-4. Variation in bulk ballast relative dielectric permittivity as a function of the void volume fraction filled with fines and saturation. Values determined using the Bruggeman-Hanai-Sen (BHS) mixing model. 114

Figure 5-5. Example raw synthetic GPR data dominated by the direct wave. 117

Figure 5-6. a) Direct wave simulated for a transmitting and receiving antenna pair suspended in free space and b) synthetic GPR data after subtraction of the direct wave..... 118

Figure 5-7. Track foundation model sensitivity analysis showing the effect of a) the horizontal dimensions of the model, b) the subballast thickness, and, c) the bulk ballast conductivity. Interpreted GPR data are not sensitive to variations in horizontal model dimensions and subballast thickness; variations in ballast conductivity do exert a systematic influence.120

Figure 5-8. Calculated ballast relative dielectric permittivity ($\varepsilon_{r,ballast}$) as a function of the volume fraction of voids containing fines and model input $\varepsilon_{r,ballast}$ showing no systematic effects of changes in ballast thickness [a), and b)] or subballast composition [c), and d)]. 122

Figure 5-9. Windowed Fourier amplitude spectrum integral (WFASI) attribute results derived from simulated GPR data as a) the ballast thickness, b) the ballast saturation, and c) the subballast material are varied. All variations lead to ambiguities in the WFASI amplitudes with respect to the volume fraction of voids filled by fines. 124

Figure 5-10. Normalized reflectivity attribute results derived from simulated GPR data as a) the ballast thickness, b) the ballast saturation, and c) the subballast material are varied. All variations lead to ambiguities in the normalized reflectivity amplitudes with respect to the volume fraction of voids filled by fines. 127

Figure 5-11. Windowed Fourier amplitude spectral integral (WFASI) [a)] and normalized reflectivity [b)] attribute results for different ballast saturations as a function of the input

bulk ballast relative permittivity. Different saturation curves are part of the same larger U-shaped behaviour. 130

Figure 5-12. Variation in windowed Fourier amplitude spectral integral (WFASI) results as the base-of-ballast is defined at different positions relative to the ballast-subballast reflection. 132

Figure 6-1. Example left and right rail a) 62-foot MCO surface track geometry deviations and b) running roughness profiles based on the deviation measurements. A 20 m filter length is used during running roughness calculation..... 145

Figure 6-2. Example of an a) unedited and b) processed centreline GPR profile acquired using the 400 MHz GSSI antenna. The user-defined base-of-ballast reflection is overlaid on the processed GPR image [b)]. For each GPR dataset (two ballast shoulders and the track centreline), the WFASI attribute [c)] is calculated based on the user-defined base-of-ballast and subsequently smoothed with a 20 m running average filter. 149

Figure 6-3. Preliminary GPR data processing algorithm applied prior to WFASI attribute calculation. 149

Figure 6-4. Comparison of the three WFASI profiles in the region of two recent ballast renewals (undercutting) performed in September 2010 and May 2011. The centreline WFASI profile demonstrates the expected increase in WFASI amplitudes in the region of relatively less degraded ballast corresponding to the 2011 renewal but no associated increase is observed for the 2010 ballast renewal. The darker shoulder WFASI profile exhibits a slight increase in WFASI amplitude for the 2010 ballast renewal but not for the

2011 renewal, while the remaining shoulder profile exhibits no significant effects related to ballast renewal. 155

Figure 6-5. Processed centreline GPR [a)] and surface running roughness [b)] data demonstrating the impact of track infrastructure; specifically, i) a crossing, ii) a culvert, and iii) a turnout. Locations of track infrastructure are removed prior to contrasting the WFASI and running roughness datasets. 157

Figure 6-6. Full-subdivision comparison of the centreline WFASI and the left rail surface running roughness. No universal association is observed between the estimates of ballast degradation and track roughness. A similar result is observed for all possible combinations of a WFASI dataset (ballast shoulder or track centreline) and a running roughness dataset (left and right rail alignment and surface). 158

Figure 6-7. Distribution of left rail surface running roughness and centreline WFASI amplitudes across the full subdivision [a) and d)], when restricted to locations where the WFASI and running roughness amplitudes are less than or equal to b) 5 or e) 30 mm^2 respectively, and when restricted to locations where the WFASI and running roughness amplitudes exceed c) 5 or f) 30 mm^2. There is no significant change in either the running roughness or WFASI distribution when the other variable is considered to be indicative of solely degraded ballast [b) - WFASI <= 5] or rough track [f) - running roughness > 30 mm^2]. 160

Figure 6-8. Repeated track geometry survey results demonstrating increasing running roughness [a)] and b) the local section of interest identified for further analysis. 163

Figure 6-9. A local comparison of the two surface running roughness (solid) profiles and the three WFASI (dashed) profiles. The thicker solid lines highlight the most recent running roughness profiles (August 2012) that are cross-correlated with the WFASI profiles. Significant R values of -0.72 and -0.60 are derived for the left rail surface running roughness and the two shoulder WFASI datasets. A significant R value (-0.69) is also derived from the cross-correlation of the most recent right rail surface running roughness profile and the darker shoulder WFASI dataset. In this local section, no significant R values are calculated when considering the centreline WFASI data. 166

Figure 6-10. A second local comparison of the two surface running roughness (solid) profiles and the three WFASI (dashed) profiles. Significant R values (-0.75 and -0.72) are derived from the cross-correlation of the most recent left and right rail running roughness profiles with the centreline WFASI dataset. In this local section, no significant R values are calculated when considering either shoulder WFASI dataset..... 167

Figure 6-11. A third local comparison of the two surface running roughness (solid) profiles and the three WFASI (dashed) profiles. In this local section, no significant correlation coefficients are observed for any combination of running roughness and WFASI datasets. 168

Figure A-1. Example TQI results for a 40 km section of the rail line under analysis; OTGI (a), Polish J Index (b) and Swedish Q Index (c). The darker shaded portions of each profile represent TQI amplitudes indicative of irregular track geometry..... 209

Figure A-2. Normalized percentages of OTGI bins belonging to each classification as a function of bin size. 213

Figure A-3. Normalized percentage of Polish J Index bins belonging to each classification as a function of bin size. 214

Figure A-4. Normalized percentages of Swedish Q Index bins belonging to each classification as a function of bin size. 215

List of Tables

Table 2-1. Description of main track geometry measurements based on Hyslip (2002)..... 15

Table 2-2. Summary of the three main track geometry interpretation types 17

Table 2-3. State of ballast degradation based on F_I (Selig and Waters 1994) 28

Table 2-4. Expected ballast behaviour with respect to *VCI* (Tennakoon and Indraratna 2014) ... 28

Table 3-1. Typical relative dielectric permittivity (ε_r) and DC electrical conductivity (σ_{DC}) values for select earth materials after Jol (2009) 42

Table 3-2. Summary of low- and high-frequency methods to estimate ballast degradation from GPR measurements 51

Table 4-1. Description of the four track geometry trend classification types..... 85

Table 5-1. Relative dielectric permittivities (ε_r) of the various components of a degraded ballast as calculated from Kashani et al. (2016) or as presented by Jol (2009) 114

Table 5-2. Relative dielectric permittivity (ε_r) and electrical conductivity (σ) for the different subballast materials considered (Jol 2009) 116

Table 6-1. The number of local track alignment sections of interest detected within the subdivision and amount of those that demonstrate significant R values when cross-correlated with a specific WFASI profile 164

Table 6-2. The number of local track surface sections of interest detected within the subdivision and amount of those that demonstrate significant R values when cross-correlated with a specific WFASI profile 165

Table A-1. Maximum allowable Polish J Indices before maintenance is required as a function of train speed 206

Table A-2. Allowable standard deviations as a function of train speed for use in Swedish Q Index calculations 207

Chapter 1: Introduction

Canada's railway network is one of the longest and most dispersed networks in the world. The network is spread through nine provinces, one territory and consists of 62,000 km of track. Traffic along the network is dominated by freight operations, which have contributed more than 90% of annual operating revenues since 2012. As such, Canada's railway network is critical to the health of the Canadian economy on a national, continental, and global scale.

The dispersed nature of Canadian railways results in a limited number of ways in which goods and people can be moved through the network. Therefore, economic rail operations are highly sensitive and susceptible to the delays caused by train derailments. Being able to minimize the risk of train derailments then has a direct correlation to economic railway operations. Moreover, in light of the resistance faced when proposing and constructing new oil-and-gas pipelines, the long-distance transportation of hydrocarbon products by rail has become increasingly prominent. As such, in addition to a significant economic benefit, there are also environmental benefits (preventing contaminant release) and societal benefits (maintaining public confidence) to be gained by railway operators and researchers by attempting to reduce the risk of train derailments.

In both Canada and the United States, the variation in track geometry is the second-leading cause of train derailments along main-line railways after broken rails (Liu et al. 2012, TSB. 2016). Maintaining proper track geometry is considered to be a primary function of railway ballast, which is the layer of crushed rock aggregate placed below and surrounding the ties in a typical ballasted track foundation (Selig and Waters 1994, Sussmann et al. 2012). Large-scale laboratory experiments have suggested that the ability of the ballast to hold the correct track geometry is inversely related to the accumulation of fine-grained particles (fines) within the void space

between the ballast aggregates (Indraratna et al. 2013, Mishra et al. 2013). As fines collect within the ballast, a process referred to as ballast degradation, increased plastic deformation of the ballast layer is expected to lead to progressive differential tie settlement and the long-term development of variable track geometry. The expected spatial association between degraded ballast and variable track geometry is so prevalent within railway engineering that regulators in both Canada (Transport Canada) and the United States (the Federal Railroad Administration) have included references to it in their respective track safety rules (Transport Canada 2012, Federal Railroad Administration 2014). The major challenges faced by railway operators are establishing the spatial association between degraded ballast and long-term trends in track geometry for an operational railway while also developing the tools necessary to identify locations of degraded ballast in a time- and cost-efficient manner.

The overall goals of this research program are threefold; first, to demonstrate that the presence of degraded ballast is spatially associated with long-term increases in track geometry variability along an in-service railway; second, to evaluate the suitability of ground-penetrating radar (GPR) as a degraded ballast detection tool for long (subdivision-scale, 100's of kilometers) sections of track; and finally, to evaluate the spatial association between locations of increasing track geometry variability and the presence of degraded ballast as estimated from field GPR measurements.

1.1. Problem Description

The majority of the Canadian rail network is constructed on ballasted track foundations. As a result, railway operators allocate significant capital resources to maintaining the ballast in order to control the development of track geometry. The challenge is that the management of degraded ballast being equivalent to the management of long-term increasing trends in track geometry

variability is based on laboratory observations and anecdotal evidence; it has yet to be rigorously demonstrated in the field. Furthermore, with finite resources to address ballast degradation across the network, railway operators must be very selective in where they perform ballast maintenance. These decisions are often made in regards to observed trends in track geometry; with little insight into if these trends are in fact related to the presence of degraded ballast.

The influence of ballast degradation on the long-term trends in track geometry variability (roughness) can be assessed through an analysis of historical undercutting (ballast renewal) records. Undercutting involves the complete removal of fines from the ballast without alteration of the other track components, such as the rail, ties, or subgrade. Any resulting change in the long-term trends in track roughness, as evaluated from repeated track geometry surveys, post-undercutting is then related to the effects of ballast degradation.

The spatial association between degraded ballast and the long-term development of track roughness has yet to be thoroughly investigated along operational railways due to the lack of an efficient method (time and cost) to infer ballast degradation. The past two decades have seen significant development of ground-penetrating radar (GPR) as an efficient ballast degradation detection tool (Jack and Jackson 1999, Clark et al. 2001, Silvast et al. 2010). GPR technology is currently in wide-scale use by the Burlington Northern Santa Fe (BSNF) Railway Company in the United States and has been applied in small-scale studies by Canadian National (CN). Much of the available literature on development of GPR is based on laboratory or limited scale-field studies performed by the service providers. There has been limited independent analysis of the fundamental geophysical principles governing the use of GPR for degraded ballast detection as well as how reliable GPR-based estimates of degraded ballast will be for large-scale field applications and how these compare with observed track behaviour.

1.2. Research Objectives

The overarching objective of this research is to provide greater quantitative insight into the effects of ballast degradation on long-term trends in track roughness in order to minimize the risk of track geometry-related train derailments and increase rail transport reliability and safety.

The four specific research objectives that form the basis of this PhD work are as follows;

I. To review and synthesize the available literature regarding the use of GPR as a ballast degradation detection tool from a fundamental geophysical perspective. This work will identify current limitations in the technology that will have to be addressed prior to attempting to associate GPR-based estimates of ballast degradation with observed trends in track roughness.

II. To use historical undercutting records to investigate whether a change in ballast degradation conditions is the dominant factor influencing long-term trends in track geometry along an operational railway, while elaborating on additional mechanisms that may also be affecting track roughness if it is not.

III. To conduct a thorough simulation-based sensitivity analysis on how ballast degradation is inferred from 400 MHz GPR data in the presence of variable track foundation conditions. From a geophysical perspective, variations in ballast thickness, saturation, and electrical conductivity as well as subballast material affect GPR measurements in a similar fashion to degraded ballast and the consequence of this must be thoroughly investigated.

IV. To quantify the spatial association between track locations exhibiting either sustained or increasing trends in track roughness and degraded ballast, as inferred from field GPR measurements. This analysis will evaluate the ability for industry to use GPR

measurements and current data interpretation methodologies to fulfill the need for a non-destructive and efficient ballast degradation tool along Canadian railways.

1.3. Description of the Study Site

All field data included in this research (for Objectives II and IV) come from a portion of CN's Edson subdivision in Alberta, Canada. The specific portion of the Edson Subdivision analyzed is the 335 km section between Stony Plain and Jasper; the trace of which is highlighted in Figure 1-1.

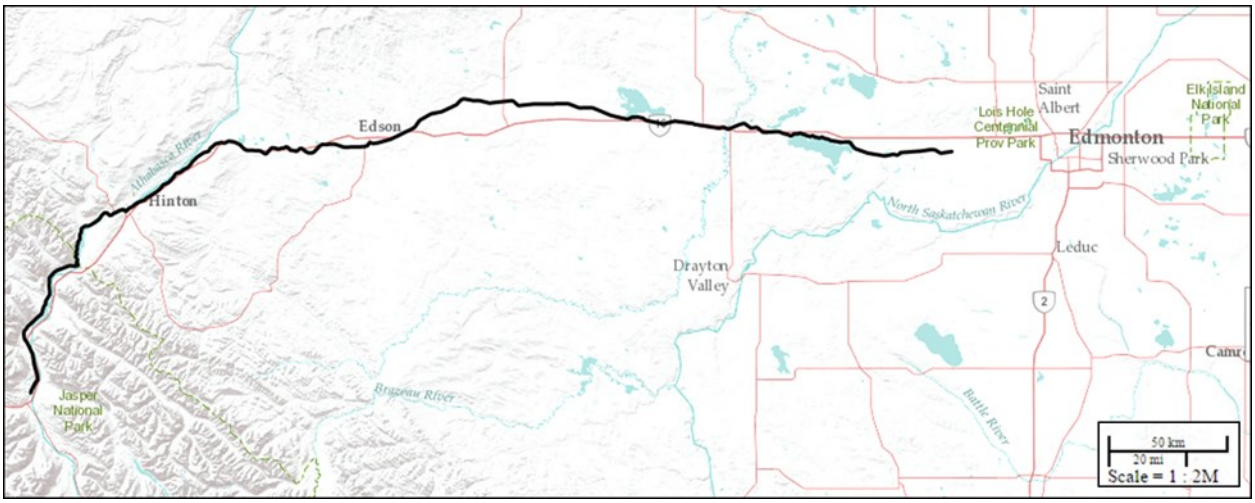

Figure 1-1. Section of CN's Edson subdivision investigated as part of this research. The section is 335 km long and extends in a dominantly east-west direction between Stony Plain and Jasper.

The Edson subdivision consists of various sections of Class II, III, and IV main-line track and is a vital component of CN's national network. It is the sole CN route connecting the interior of Canada to ports on the Pacific coast (Prince Rupert and Vancouver). Annual freight loads along the subdivision are typically 50 million gross tonnes (MGT) and concrete and continuously-welded rail are the dominant tie and rail types.

The 335 km-long portion on the Edson subdivision investigated in this research crosses a variety of different surficial geologies. Surficial geology east of Edson is defined at 1:100,000 scale by the Alberta Agriculture and Forestry as the Agricultural Region of Alberta Soil Inventory Database (AGRASID) and accessible through the on-line Alberta Soil Information Viewer (Alberta Agriculture and Forestry 2012). Surficial soil conditions underlying the railway east of Edson include organic (peat) dominated soils as well as mineral-based (sand, silt, clay, and till) soils. Both soil types (organic and mineral) can be interspersed with one another at a resolution beyond that of the AGRASID database. Surficial soils west of Edson are not included in AGRASID due to the lack of agricultural development. Larger regional trends in surficial geology west of Edson can be inferred from the Alberta surficial geology map produced by the Alberta Geological Survey (Fenton et al. 2013) as well as air photos.

1.4. Scope and Methodology

This research synthesizes and discusses the available literature related to the use of GPR as a degraded ballast detection tool from a fundamental geophysical perspective, investigates the long-standing belief that improvements in ballast degradation conditions through undercutting will result in a noticeable improvement on trends in track geometry, illustrates the sensitivity of GPR-based ballast degradation estimates to other structural and compositional changes in a ballasted track foundation, and investigates the spatial correlation between locations of sustained or increasingly rough track geometry and the presence of degraded ballast as estimated from GPR measurements. Three main types of data are considered during this research; track geometry data collected during routine CN track geometry surveys as well as synthetically generated and field-collected 400 MHz GPR data from which ballast degradation is estimated. Of note is that the field GPR measurements were performed prior to the start of this specific

research project. Furthermore, the GPR measurements were performed with the intention of providing an overall view of the track foundation, while this research focuses specifically on the portions of these measurements within the ballast. In addition to the track geometry and GPR datasets, CN ballast maintenance records are used to identify the timing and location of track undercuttings and the AGRASID database is used to differentiate between surficial soil types on which the undercut portions of track have been constructed. The following sections outline the steps followed to achieve the four research objectives

1.4.1. Review and Synthesis of the Relevant Literature regarding GPR as Applied to Ballast Degradation Studies

This section outlines the methodology followed during the completion of Objective I; a review and synthesis of the available literature related to the use of GPR as a degraded ballast evaluation tool. GPR is already in commercial use as a degraded ballast detection tool as it is intended to provide distinct time and cost saving advantages compared to conventional ballast sampling and testing. A variety of approaches for inferring the amount of fines present within the ballast void space have been presented in the literature. However, there has yet to be a thorough review, synthesis, and comparison of these GPR measurement interpretation strategies based on the underlying physical phenomena.

Any discussion of GPR as a change detection tool (degraded versus non-degraded ballast) must be rooted in the fundamental geophysical phenomena that govern electromagnetic (EM) wave propagation and reflection. As such, the bulk effects the accumulation of fines exerts on GPR measurements are introduced only after a discussion of both the fundamental physical principles and material properties relevant to GPR studies. With a theoretical background established, the resulting changes in GPR measurements due to degraded ballast can be predicted and data

interpretation techniques developed in the literature can be thoroughly assessed. Qualitative as well as quantitative strategies to infer the amount of fines present within a column of ballast are introduced and discussed for both low-frequency (<1 GHz) and high-frequency (>1 GHz) GPR signals with relevant examples extracted from existing literature. Finally, low- and high-frequency methods are contrasted in order to illustrate their respective benefits and limitations.

1.4.2. Investigating Ballast Degradation as a Dominant Factor Affecting Trends in Track Geometry

This section outlines the methodology followed during the completion of Objective II; investigating of contribution from improved ballast degradation conditions on long-term trends in track geometry using historical undercuttings. Track geometry is the primary indicator used by operators to gauge the performance of their railways and allocate maintenance resources. As track geometry is measured repeatedly throughout the year, it is also the most appropriate metric with which to follow the trends in track performance through time. Ballast renewal maintenance programs represent fixed points in space and time where degradation conditions in the ballast have been improved without alterations to the remaining track components (rails, ties, subgrade, etc.). Therefore, they are uniquely suited to investigating the change in long-term track geometry trends resulting from the removal of fines from the ballast.

The scope of work involved isolating sections of track which had been subject to ballast renewal operations and then investigating the long-term changes in track geometry from what was observed before ballast renewal to several years following ballast renewal. Two years of ballast renewal operations along the Edson subdivision were analyzed as part of this research. The individual steps followed in the study include; 1) cleaning the ballast maintenance records to isolate the continuous track sections where ballast undercutting is known to have occurred, 2)

segmentation of these extended sections to a consistent length, 3) quantification of track geometry variability (roughness) in each segment for three track geometry variables over a five year analysis window extending both before and after the ballast renewal took place, and 4) classification and comparison of the temporal patterns in track roughness after ballast renewal across multiple segments and between subgrade conditions (derived from AGRASID). The classification of the individual segments along the railway also allows for the relationship between degraded ballast and the long-term trends in track roughness to be mapped for each track geometry variable.

1.4.3. The Sensitivity of Ballast Degradation Estimates in the Presence of Variable Track Foundations

This section outlines the methodology followed during the completion of Objective III; a simulation-based sensitivity analysis of ballast degradation estimates from 400 MHz GPR data in the presence of variable track foundations. The purpose of this section is to investigate what effect a variable ballast thickness, ballast saturation, or subballast material will have on ballast degradation estimates derived from 400 MHz GPR data. In order to properly interpret the subdivision-scale field 400 MHz GPR measurements, it is critical to first assess what impacts a structurally and compositionally variable track foundation will have. The simulation-based approach employed here is the only approach capable of generating reliable and repeatable GPR measurements in a controlled manner.

The scope of work involved numerically simulating the expected GPR response from a ballasted track foundation as the conditions in the track foundation were progressively varied. This was then followed by the application of tested and literature-established GPR data interpretation techniques to infer the volumetric concentration of fines within the ballast and comparison with

the known amounts assigned to the model. The individual steps followed in the study include; 1) construction of multiple ballasted track foundation within the simulation software, 2) deriving and assigning representative material properties to each layer to reflect their respective composition, 3) generation of the synthetic GPR measurements, and 4) ballast degradation interpretation of the GPR measurements using three established techniques and comparison between the results as ballast thickness, saturation, conductivity, and subballast material type are progressively altered.

1.4.4. The Spatial Association between Rough Track and GPR-Inferred Degraded Ballast

This section outlines the methodology followed during the completion of Objective IV; quantifying the spatial correlation between trends in track roughness and GPR-inferred degraded ballast. As with Objective II, track geometry data and the trends generated from them are the major performance metrics used by operators while monitoring their railways. GPR measurements are non-destructive and can yield insight into track foundation conditions (including ballast degradation) across a spatially extensive area in both a time- and cost-effective manner. However, as of yet, no large-scale comprehensive investigation between the spatial correlation of track roughness and GPR-based inferences of ballast quality has been presented in the literature.

The scope of work involved spatially correlating track roughness and GPR-based ballast degradation profiles in sections of track where either sustained or increasing trends in track roughness were detected. The individual steps followed in the study include; 1) isolation of track sections exhibiting sustained or increasing trends in track roughness, 2) interpretation of the GPR measurements using established methods to infer the presence of ballast degradation, 3) combination of the track roughness and GPR-based ballast degradation profiles onto a single

spatial axis and 4) cross-correlation of the roughness and ballast degradation profiles to quantify the spatial correlation between the two datasets.

1.5. Thesis Outline

This thesis consists of seven chapters, including this introductory chapter, one appendix, and has been prepared in the manuscript-based format.

Chapter Two contains the literature review necessary for this study for all topics discussed except the development of GPR as a degraded ballast detection tool.

Chapter Three (manuscript #1) provides a thorough and in-depth review of GPR as a ballast degradation detection tool.

In *Chapter Four* (manuscript #2), the impact of undercutting on the long-term (3-to-4 year) trends in track roughness is quantified using observations from the Edson subdivision (Figure 1-1).

Chapter Five (manuscript #3) uses simulated 400 MHz GPR measurements to perform a sensitivity analysis on the effect a variable ballast thickness, ballast saturations, and subballast material type have on the attributes used to infer ballast degradation from GPR measurements.

Chapter Six (manuscript #4) presents a spatial comparison of track roughness and ballast degradation, as inferred from field GPR measurements, for the entire studied length of the Edson subdivision (Figure 1-1).

Chapter Seven contains the conclusions and recommendations stemming from this study.

Finally, *Appendix A* presents a comparison of different track geometry interpretation methodologies; specifically, the equivalence of rough track as determined from minimum safety threshold exceedances and three track quality indices.

1.6. References

Alberta Agriculture and Forestry. 2012. Alberta soil information viewer [online]. Available from http://www4.agric.gov.ab.ca/agrasidviewer/ [cited 03/16 2016].

Clark, M.R., Gordon, R., Kemp, T., and Forde, M.C. 2001. Electromagnetic properties of railway ballast, NDT&E International, **34**(5): 305-311.

Federal Railroad Administration. 2014. Track and rail and infrastructure integrity compliance manual. Federal Railroad Administration, Washington DC, USA.

Fenton, M.M., Waters, E.J., Pawley, S.M., Atkinson, N., Utting, D.J., and Mckay, K. 2013. Surficial geology of alberta. Alberta Energy Regulator, Edmonton, AB, Canada.

Indraratna, B., Tennakoon, N., Nimbalkar, S., and Rujikiatkamjorn, C. 2013. Behaviour of clay-fouled ballast under drained triaxial testing, Géotechnique, **63**(5): 410-419.

Jack, R. and Jackson, P. 1999. Imaging attributes of railway track formation and ballast using ground probing radar, NDT&E International, **32**(8): 457-462.

Liu, X., Saat, M.R., and Barkan, C.P.L. 2012. Analysis of causes of major train derailment and their effect on accident rates, Transportation Research Record, **2289**: 154-163.

Mishra, D., Kazmee, H., Tutumluer, E., Pforr, J., Read, D., and Gehringer, E.:. 2013. Characterization of railroad ballast behavior under repeated loading: Results from new large triaxial setup, Transportation Research Record, **2374**: 169-179.

Selig, E.T. and Waters, J.M. 1994. Track geotechnology and substructure management. Thomas Telford Ltd., London.

Silvast, M., Nurmikolu, A., Wiljanen, B., and Levomaki, M. 2010. An inspection of railway ballast quality using ground penetrating radar in finland, Proceedings of the Institution of Mechanical Engineers, Part F: Journal of Rail and Rapid Transit, **224**: 345-351.

Sussmann, T.R., Ruel, M., and Chrismer, S.M. 2012. Source of ballast fouling and influence considerations for condition assessment criteria, Transportation Research Record, **2289**: 87-94.

Transport Canada. 2012. Rules respecting track safety. Canada, Ottawa.

Transportation Safety Board of Canada. 2016. Statistical summary - railway occurrences 2015 - data tables [online]. Available from http://www.bst-tsb.gc.ca/eng/stats/rail/2015/sser-ssro-2015-tbls.asp [cited 05/12 2017].

Chapter 2: Literature Review

2.1. Track Geometry

2.1.1. Basic Measurements

The three-dimensional spatial orientation of railway tracks, henceforth referred to as 'track geometry', provides a primary measure of both track performance and ride quality (Selig and Waters 1994, Hyslip 2002, Li et al. 2016). Through the analysis of track geometry measurements, sections of track that exhibit performances outside of the safety or comfort standards set by either the railway operators or the regulators, Transport Canada (2012) or the Federal Railroad Administration (2014) in the United States, can be identified and subsequently rectified by maintenance (tamping, undercutting, stone blowing etc.). Repeated track geometry surveys performed throughout the year allows for the detection and amelioration of track geometry issues before they begin to pose a potential risk for vehicle derailments.

Major Canadian railway operators, such as Canadian National (CN) and Canadian Pacific (CP), monitor track geometry with specially designed rail vehicles that continually traverse their respective networks. Track geometry measurements are commonly made at 0.30 m (one foot) increments along the railway. There are a wide variety of variables used to quantify track geometry during a single survey. These variables can be classified into one of two main categories based on whether the orientation of one or both of the rails is considered during calculation. Track geometry variables such as track gauge, crosslevel and twist are *relative* measurements of the offsets between the two rails and yield a single value at each track geometry measurement position. In contrast, track geometry variables such as alignment and surface quantify the *absolute* orientation of each rail relative to some separate datum and are defined for

each rail individually at each measurement position. Table 2-1 presents a description for each of these common track geometry measures based on Hyslip (2002).

Table 2-1. Description of main track geometry measurements based on Hyslip (2002).

Track Geometry Measure	Description
Gauge	The horizontal distance between the two rails measured from the rail heads
Crosslevel	The difference in elevation between the two rails measured along a horizontal line
Twist	The difference in crosslevel measured between any two points either less than or equal to a certain distance apart.
Alignment	The horizontal deviation of the rail relative to a straight-line reference chord after projecting both the rail and the chord onto the horizontal plane
Surface	The vertical deviation of the rail relative to a straight-line reference chord after projecting both the rail and the chord onto the vertical plane

In North America, the alignment and surface track geometry variables are quantified as mid-chord offsets (MCO) (Hyslip 2002, Li et al. 2016). The chord can be considered as an imaginary straight-line beam with a fixed length (the chord length) connecting two points on the rail. When used to define the alignment or surface mid-chord offset, the reference datum is then either the horizontal or vertical projection of that three-dimensional beam. The alignment and surface measurements are the horizontal or vertical deviations between these chord projections and the similar projection of the track at the mid-chord position (Figure 2-1). Common chord lengths include 24.1 m (79 feet), 18.9 m (62 feet), and 9.5 m (31 feet).

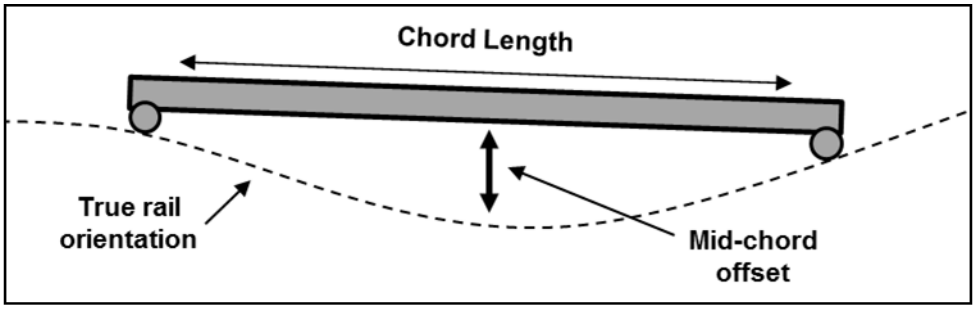

Figure 2-1. Principles of performing a MCO measurement.

Track alignment and surface deviations quantified at the same track positions but with different chord lengths are rarely equal. The different fixed chord lengths result in different reference datums used in the MCO measurements. Similar MCO deviations will only be measured if the reference chords intersect at their mid-point. Furthermore, MCO measurements are not necessarily the same as those that would be measured geodetically (i.e. using a theodolite stationed off of the track), as the reference chord changes its orientation at each measurement position along the railway depending on the geometry of the rails. Overall, the effect of quantifying track alignment and surface as a MCO measurement is that each variable is subject to mechanical filtering that removes long wavelength features in track geometry (Hyslip 2002, Li et al. 2016).

2.1.2. Methods to Interpret Track Roughness

Once track geometry data have been collected, there are multiple ways in which it can be interpreted to distinguish between sections of well-performing track and those where intervention and track re-alignment are necessary. The three main types of track geometry interpretations include; threshold exceedance analysis, running roughness analysis, and track quality index (TQI) analysis (Table 2-2). Multiple individual analyses exist within each approach

depending on different specifics such as which track geometry variables are considered, the regulatory environment, and the nature of the railway traffic (passenger versus freight).

Table 2-2. Summary of the three main track geometry interpretation types.

Interpretation Type	Definition
Threshold Exceedance	Track geometry measurements exceeding a pre-defined threshold for a specific geometry variable. Individual railway regulators and railway operators often have different pre-defined thresholds for different geometry variables.
Running Roughness	Smoothed squares of individual track geometry variables.
Track Quality Indices (TQIs)	Individual or statistical combinations of threshold exceedances or standard deviations derived from multiple track geometry variables within the same section of track. May also be derived from the actual three-dimensional space curve of the rails.

Interpretations of track geometry data based on threshold exceedances are straightforward. A set of maximum thresholds are defined that once exceeded, imply the need for corrective maintenance (Rail Safety and Standard Board Limited 2011, Transport Canada 2012, Federal Railroad Administration 2014). These thresholds can be defined from either a safety or a ride-quality perspective. Minimum thresholds are commonly set by regulators and vary depending on the class of track (indicative of the maximum speed at which trains are allowed to proceed). As can be expected, sections of track with higher operating speeds commonly have more restrictive thresholds. In Canada, major railway operators (CN and CP) maintain their track to tighter track geometry thresholds than those mandated by Transport Canada. This is to avoid the mandatory track closure until the exceedance can be corrected, should the Transport Canada minimum thresholds ever be exceeded.

The running roughness approach to track geometry was first proposed by Ebersöhn and Selig (1994). Running roughness (*RR*) represents the smoothed square of individual track geometry datasets, calculated as

$$RR = \frac{1}{n}\sum_{i=1}^{n} d_i^2 \ . \qquad \text{[Equation 2-1]}$$

d_i in Equation 2-1 represents the individual measurements for a particular track geometry variable, while n represents the number of consecutive measurements considered during smoothing (the smoothing length). Ebersöhn and Selig (1994) did not specify a particular smoothing length in the original definition of the running roughness; however, Li et al. (2016) suggest a smoothing length equal to the truck spacing of typical rail vehicles traversing the section of railway under analysis. Running roughness is not a regulated approach to the interpretation of track geometry data in Canada; however attempts have been made to categorize track performance based on the calculated running roughness amplitudes in the United States (Sadeghi 2010).

Finally, track quality indices (TQIs) commonly infer track performance based on the standard deviation of the track geometry measurements. The standard deviation (*SD*) of n individual track geometry measurements (d_i) with a mean value of $\bar{\mu}$ is defined by;

$$SD = \sqrt{\frac{1}{n}\sum_{i=1}^{n}(d_i - \bar{\mu})^2} \ . \qquad \text{[Equation 2-2]}$$

A wide assortment of standard deviation-based TQIs have been proposed in the literature or are in current regulated use on railways around the world (Sadeghi and Askarinejad 2009, Sadeghi and Askarinejad 2010, Sadeghi 2010, Rail Safety and Standard Board, Limited 2011, Audley and Andrews 2013). TQIs include both individual standard deviations calculated for specific track geometry variables (Sadeghi and Askarinejad 2009, Rail Safety and Standard Board Limited 2011, Audley and Andrews 2013) and arithmetic combinations of multiple standard deviations

weighted individually to reflect their relative importance (Sadeghi and Askarinejad 2010, Sadeghi 2010). Arithmetic combinations of individual standard deviations are widely used to infer overall track performance but are limited in their ability to identify factors in the track foundation that may be contributing to the variable track geometry (Sadeghi and Askarinejad 2009). In addition to standard deviation-based TQIs, TQIs have also been developed based on the three-dimensional space curve of the rails (El-Sibaie and Zhang 2004) as well as the number of threshold exceedances (Sadeghi 2010). Each individual TQI can then be used to assess track performance based on the resulting TQI amplitudes.

Appendix A presents a detailed investigation into the equivalency between the existence of minimum safety threshold exceedances and rough track as determined from the amplitudes of three TQIs. The results demonstrate that certain TQI are more successful than others at indicating the presence of rough track at the same track positions where threshold exceedances are detected (the details of the particular TQI analyzed are presented in Appendix A). Furthermore, for an individual TQI, the TQI-threshold exceedance equivalency is also affected by the number of track geometry measurements considered when defining the standard deviation of an individual track geometry variable (n in Equation 2-2). The advantage of a TQI-based approach to analyzing track geometry datasets, compared to threshold exceedances, is that TQIs are continuous. When a suitable agreement between TQI-implied rough track and the existence of threshold exceedances is observed, TQI amplitudes may also be indicative of variable track geometry in sections of track where no threshold exceedances are present.

2.2. Ballasted Track Foundations

The cross-section of a typical ballasted railway track foundation is presented in Figure 2-2. The foundation can be subdivided into two sub-systems; the superstructure and the substructure

(Selig and Waters 1994). The track superstructure encompasses the rails, ties and fasteners (which hold on the rail in place on the ties), while the substructure consists of the ballast, subballast, and subgrade.

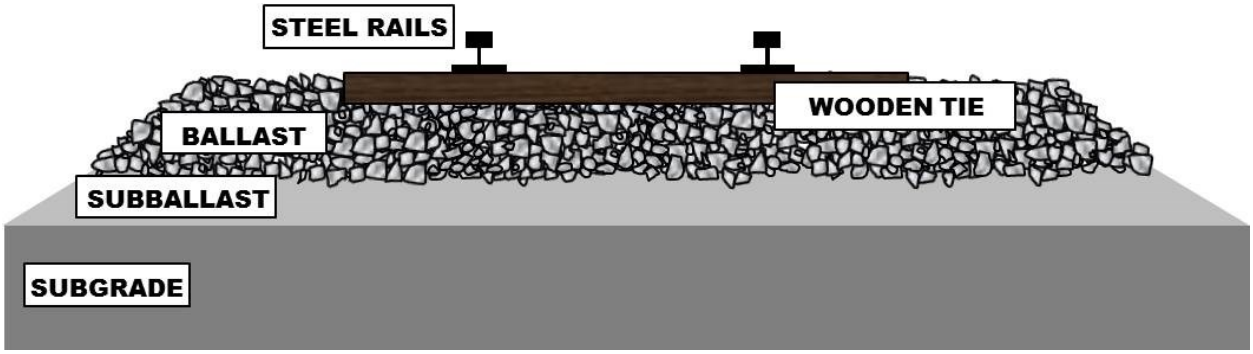

Figure 2-2. Cross-section of a typical ballasted track foundation.

The following sections elaborate further on the functionality and specifics of the ballast layer as well as how ballast degradation affects the ability of the ballast layer to perform its intended functions and may lead to the development of track geometry issues.

2.2.1. The Ballast Layer

In its ideal state, the ballast layer is comprised of angular crushed rock aggregate (limestone, granite, or basalt) between 10 and 75 mm in diameter. (Li et al. 2016). Figure 2-3 presents the particle size distributions for two common gradations of mainline ballast (AREMA #4 and #24).

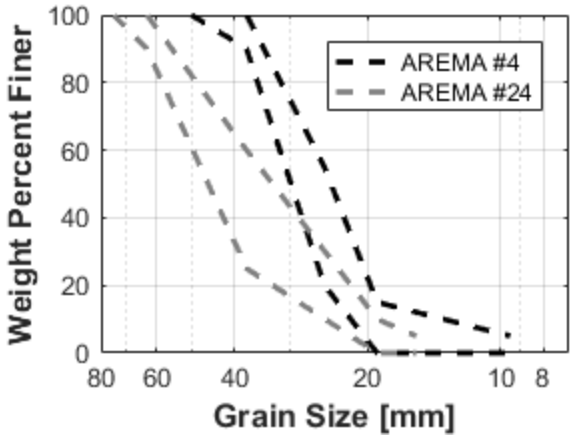

Figure 2-3. Particle size distributions for AREMA #4 and #24 ballast gradations after Li et al. (2016).

A wide variety of tests exist in order to evaluate the suitability of a particular aggregate to construct a ballast layer with, beyond it satisfying an appropriate particle size distribution (Selig and Waters 1994, Li et al. 2016). These tests include durability tests (Los Angeles abrasion, Deval attrition), aggregate shape tests (elongation, angularity), unit weight determination tests, environmental tests, and petrographic analyses. Durability tests yield a measure of aggregate toughness or resistance to abrasion, which is critical because the ballast is subjected to high loads during trafficking. The shape of the aggregate particles is also an important factor to consider as the interlocking of angular asperities is what provides the strength and resiliency of the ballast. Unit weight and environmental tests are used to evaluate the porosity of the aggregate as well as the tendency of the aggregate to fracture or breakdown due to freeze-thaw cycles or chemical weathering. Finally, petrographic analyses are used to determine the mineral composition of the aggregate in order to predict/assess its behaviour.

Once a suitable aggregate is selected, the functions that the ballast layer must perform in order for the track foundation to operate as intended include (but are not limited to);

- provide water-shedding pathways and sufficient storage space for fine-grained material so they do not impede drainage,
- provide resistance against the forces applied to the ties (vertical, longitudinal and lateral) during the passing of trains,
- provide resiliency against the accumulation of deformation, and
- reduce the applied loads on the subballast and subgrade to manageable levels by distributing the train loads over a wider area.

Large ballast void spaces required to conduct infiltrating water and store fine-grained materials are a consequence of more uniformly graded ballast (such as the AREMA #4 gradation in Figure 2-3). More broadly graded ballast (such as the AREMA #24 gradation in Figure 2-3) are expected to be relatively stronger compared a uniformly graded ballast due to the smaller void ratio (Indraratna et al. 2011a).

Regardless of the actual ballast gradation, the shear strength and resilience of the ballast layer is provided by the interlocking of the angular aggregates, aggregate durability, and ballast layer compaction. The resiliency of ballast against the accumulation of deformation is encapsulated in the resilient modulus (M_r),

$$M_r = \frac{\Delta q}{\varepsilon_{ra}}, \qquad \text{[Equation 2-3]}$$

which can be measured during cyclic triaxial tests once plastic deformation has ceased (Figure 2-4). In Equation 2-3, Δq represents the deviator stress applied during each repeated load increment and ε_{ra} represents the recoverable axial strain. Ballast with a higher resilient modulus accumulates plastic (unrecoverable) axial strains at a slower rate compared to ballast exhibiting a lower resilient modulus and are therefore more resistant to deformation.

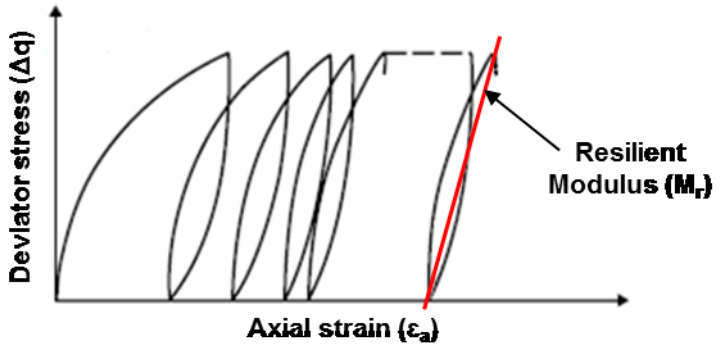

Figure 2-4. Illustrative results from a cyclic triaxial test of railway ballast demonstrating the accumulation of unrecoverable (plastic) axial strain until resilient (elastic) behaviour is observed after Li et al. (2016). Deformation in the elastic regime is characterized by the resilient modulus (M_r – Equation 2-3).

The amount of load dissipation within the ballast is related to the thickness of the ballast layer. The American Railway Engineering and Maintenance-of-way Association (AREMA) guidelines (AREMA 2012) provide the empirical Talbot equation as a simple relationship to determine an appropriate ballast thickness (H) in meters,

$$H = 0.24 * \left(\frac{P_m}{P_c}\right)^{0.8}. \quad \text{[Equation 2-4]}$$

P_c in Equation 2-4 represents the allowable vertical compressive stress at the top of the subgrade (AREMA recommends 138 kPa) and P_m represents the vertical stress applied at the ballast surface. Other methods to determine an appropriate ballast thickness include the Raymond method, the British Rail method, and the Li-Selig method (Li et al. 2016).

2.2.2. Fundamentals of Ballast Degradation

The ability of a ballast layer to perform its intended functions is dependent on the ballast being free of fine-grained particles (fines). The process of fines accumulating within the ballast void

space is referred to as ballast degradation (sometimes also referred to as ballast fouling). Significant laboratory testing has been dedicated to characterizing the effects of degradation on the shear strength and resilient modulus of the ballast (Selig and Waters 1994, Huang et al. 2009, Sussmann et al. 2012, Indraratna et al. 2013, Mishra et al. 2013). Many of these studies extrapolate the results of laboratory tests to in-service ballast along operational railways and predict a spatial association between degraded ballast and increased track geometry variability. Progressive ballast degradation is also a critical cause of increasing track roughness through time in many predictive track geometry modelling algorithms (Sadeghi and Askarinejad 2010, Andrews 2012, Prescott and Andrews 2013, Andrews et al. 2014, Prescott and Andrews 2015).

Selig and Waters (1994) identified five primary sources of ballast fines; ballast breakdown, infiltration from the ballast surface, erosion of the sleepers, infiltration from underlying placed layers (subballast and fill) and infiltration from the natural subgrade. The relative contribution of each of these five sources to the total amount of fines within the ballast layer is dependent on the geographic location and the type of rail traffic. From observations on North American railways, Selig and Waters (1994) determined that 76% of fines are generated from the internal breakdown of the ballast due to train loading and weathering. The contributions from the remaining sources (infiltration from the surface, sleeper erosion, infiltration from underlying placed layers and infiltration from the natural subgrade) were 7, 1, 13, and 3%, respectively. In contrast, Indraratna et al. (2013) observed that for typical Australian railways, the majority of fines are derived from the soils (either placed or natural) below the ballast. Finally, in regions of significant coal transport by rail, Feldman and Nissen (2002) observed that upwards of 95% of fines within the ballast were coal dust that had infiltrated into the ballast from the surface.

The source of the ballast fines is important as different types of fines have different effects on the ballast shear strength and resilient modulus. A convention within the literature is to differentiate the observed behaviour according to three main types of fines; mineral degradation from broken aggregate, clay degradation from infiltrating soils, and coal degradation from settling coal dust (Huang et al. 2009, Indraratna et al. 2009, Nimbalkar et al. 2012, Tennakoon and Indraratna 2014)

Huang et al. (2009), Nimbalkar et al. (2012) and Indraratna et al. (2013) each performed a series of laboratory shear tests (either direct shear or triaxial compression) to investigate the effect of both fines type and moisture content on the shear strength of ballast (Figure 2-5). Under dry conditions, ballast degraded with coal dust exhibited the lowest shear strength followed by clay and then mineral fines. All degraded ballast shear strengths were lower than what was observed for non-degraded (clean) ballast. As moisture contents were varied, both the coal and clay degraded ballast exhibited decreases in ballast shear strength with increasing moisture content, with the coal degraded ballast being more strongly affected. Mineral degraded ballast exhibited little sensitivity to changes in moisture content. These experimental results are the same as those suggested by Sussmann et al. (2012).

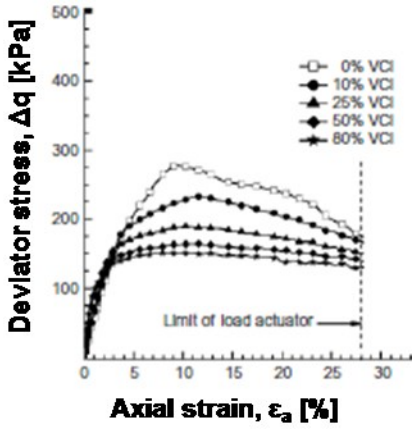

Figure 2-5. Experimental isotropic drained triaxial test results for various clay-degraded ballast samples with a 10 kPa confining stress after Indraratna et al. (2013). There is a clear reduction in ballast shear strength as clay particles accumulate (represented by a VCI increase) within the ballast.

In contrast to shear strength, laboratory tests revealed that the overall change in resilient modulus relative to clean ballast was dependent on the type of fines. Indraratna et al. (2009) observed that the addition of mineral fines increases the resilient modulus of ballast; while Tennakoon and Indraratna (2014) observed that clay fines decrease the resilient modulus. The author's concluded that mineral-based fines exerted a stabilizing effect on the ballast due to an increase in the interparticle contact area. For ballast containing significant clay particles, the clay particles coat the ballast aggregates and reduce interparticle friction allowing for more deformation during cyclic loading and a lower resilient modulus.

2.2.3. Quantification of Ballast Degradation

There are a number of different approaches to quantify the amount of fines within a ballast sample. These approaches can be categorized into two main types; mass-based methods and

volume-based methods. Mass-based approaches include the fouling index (F_I), the percent fouling and the D-Bar methods (Selig and Waters 1994, Anbazhagan et al. 2011), while the volume-based systems include the percent void contamination (PVC), relative ballast fouling ratio ($R_{b\text{-}f}$) and void contamination index (VCI) methods (Feldman and Nissen 2002, Indraratna et al. 2011b, Nimbalkar et al. 2012, Indraratna et al. 2013, Tennakoon and Indraratna 2014). The differentiation between mass-based and volume-based approaches is required in order to account for the different specific gravities of mineral, clay, and coal fines.

The most common mass-based approach is the fouling index (Selig and Waters 1994), while the most common volume-based system is the void contamination index (Indraratna et al. 2013). The fouling index is defined as

$$F_I = P_4 + P_{200} \ , \qquad \text{[Equation 2-5]}$$

where P_4 is the weight percentage of the ballast sample passing the number four sieve (4.75 millimeter) and P_{200} is the weight percentage passing the number 200 sieve (0.075 millimeter). The void contamination index (VCI) is defined as the ratio between the volume of degradation material (V_f) and the volume of the ballast voids (V_{vb}),

$$VCI = \frac{V_f}{V_{vb}} = \frac{(1+e_f)}{e_b} * \frac{G_{sb}}{G_{sf}} * \frac{M_f}{M_b} * 100\% \ . \qquad \text{[Equation 2-6]}$$

VCI can also be defined in terms of common soil parameters for a sample of degraded ballast where e_f is the void ratio of the degradation material, e_b is the void ratio of a clean ballast, G_{sb} is the specific gravity of a clean ballast, G_{sf} is the specific gravity of the degradation material, M_f is the mass of the degradation material, and, finally, M_b is the mass of the clean ballast.

Selig and Waters (1994) and Tennakoon and Indraratna (2014) developed individual ballast classification systems based on F_I and VCI respectively. Table 2-3 presents the F_I classification system that relates a calculated F_I to a state of ballast degradation, while Table 2-4 presents the

VCI classification system which relates *VCI* to an expected ballast performance. While not explicitly stated in the F_I classification system (Table 2-3), similar to the *VCI* system (Table 2-4), Selig and Waters (1994) anticipate increasing ballast deformation (axial strain) as fines accumulate within the ballast void space (as the ballast transitions from clean to highly fouled).

Table 2-3. State of ballast degradation based on F_I (Selig and Waters 1994).

Ballast Degradation State	Range of Calculated Fouling Indices
Clean	$F_I < 1$
Moderately Clean	$1 \leq F_I < 10$
Moderately Fouled	$10 \leq F_I < 20$
Fouled	$20 \leq F_I < 40$
Highly Fouled	$F_I \geq 40$

Table 2-4. Expected ballast behaviour with respect to *VCI* (Tennakoon and Indraratna 2014).

Zone	VCI Range	Expected Ballast Performance
1	$VCI \leq 25\%$	Lubrication of ballast - increased axial strain with increasing *VCI*
2	$25\% \leq VCI \leq 50$	Stabilisation of ballast - little increase in axial strain with increasing *VCI*
3	$VCI > 50\%$	Impeded drainage - increased axial strain with increasing *VCI* and generation of pore water pressures

2.3. Field Methods to Assess Ballast Degradation

2.3.1. Destructive Methods

The most direct way to assess ballast degradation along a railway is through destructive ballast sampling (Brough et al. 2003, Federal Railroad Administration 2011). In destructive sampling, the ballast is excavated from the track foundation (by either automatic ballast samplers, test-pits,

or trenching) and transported for laboratory analysis. From these laboratory analyses (particle size analysis, standard Proctor tests, etc.), the degradation state of the ballast can then be reliably quantified using one of the methods discussed previously (F_I or VCI for example). Issues with destructive ballast sampling are that the process of excavating the ballast, transporting the sample, and performing the laboratory testing is slow and time consuming as well as costly if the ultimate goal is to characterize ballast degradation over a large spatial area. In addition, the fibre-optic cables that control train signalling are often buried in the ballast shoulders and can be damaged if the ballast excavation is not performed with care.

2.3.2. Non-Destructive Methods

Non-destructive methods to assess ballast degradation have been developed as an alternative to destructive methods in order to be deployable over a large spatial area in a cost and time efficient manner. Three main non-destructive ballast evaluation methodologies have been proposed; visual inspections, vertical track deflections, and ground-penetrating radar (GPR). The remainder of this chapter is dedicated to the introduction and discussion of the visual inspection and vertical track deflection non-destructive techniques. The theoretical basis as well as the implementation of GPR as a ballast degradation detection tool is discussed in depth in Chapter Three.

Sadeghi and Askarinejad (2009, 2011) develop and implement a methodology to assess ballast degradation through visual inspection as part of a broader track condition investigation. Through consultation with industry experts, the authors develop a three-tier (low, moderate, and high) severity ranking criteria for ballast degradation. As the amount and composition of ballast fines are difficult to quantify visually, the severity ranking criteria relies strongly on the presence of vegetation growth within the ballast. At the lowest severity level, vegetation growth is present within the ballast but does not interfere with the visual ballast inspection, while at the highest

severity level, the vegetation is deemed dense enough to interfere with train movements. This visual ballast assessment methodology, while straightforward to implement, cannot detect the accumulation of fines within the ballast without any surface expression and, in absence of any vegetation growth, the severity of the ballast degradation cannot be easily differentiated.

Sussmann et al. (2012) suggest that measurements of vertical track deflection can be used to assess ballast degradation. The basis for this approach is that areas of degraded ballast, where the accumulation of fines has reduced the resilient modulus of the ballast layer as well as the overall stiffness of the track foundation (track modulus), would correlate with larger observed track deflections under the same applied load. However, Selig and Li (1994) demonstrate that subgrade stiffness most strongly influences observed track modulus, with the contribution of resilient ballast modulus is expected to be small.

Two methods that have been used to study vertical track deflections along Canadian railways are the falling weight deflectometer (Haji Adbulrazagh and Hendry 2016) and the MRail system (Roghani and Hendry 2016). Falling weight deflectometer measurements involve dropping a weight on the track foundation while measuring surface deflections radially outward from the weight using geophones. The MRail system is a mobile unit mounted on a rail car which measures relative deflections in the rail as it traverses the railway under investigation. Both sets of vertical track deflection measurements exhibit stronger correlations with the presence of soft subgrades than with ballast degradation (Haji Adbulrazagh and Hendry 2016, Roghani and Hendry 2016).

With visual ballast inspection methods unable to differentiate between degradation conditions in absence of any noticeable surface expression (either considerable vegetation growth or visible changes in fines concentrations) and vertical track deflections dominated by subgrade stiffness,

GPR is the only remaining non-destructive method that may be capable of producing efficient inferences of ballast degradation levels.

2.4. References

Anbazhagan, P., Su, L., Buddhima, I., and Cholachat, R. 2011. Model track studies on fouled ballast using ground penetrating radar and multichannel analysis of surface wave, Journal of Applied Geophysics, **74**: 175-184.

Andrews, J. 2012. A modelling approach to railway track asset management, Proceedings of the Institution of Mechanical Engineers, Part F: Journal of Rail and Rapid Transit, **227**(1): 56-73.

Andrews, J., Prescott, D., and De Rozières, F. 2014. A stochastic model for railway track asset management, Reliability Engineering and System Safety, **130**: 76-84.

AREMA. 2012. Manual for railway engineering. American Railway Engineering and Maintenance of Way Association, Lanham, MD, USA.

Audley, M. and Andrews, J.D. 2013. The effects of tamping on railway track geometry degradation, Proceedings of the Institution of Mechanical Engineers, Part F: Journal of Rail and Rapid Transit, **227**(4): 376-391.

Brough, M., Stirling, A., Ghataora, G., and Madelin, K. 2003. Evaluation of railway trackbed and formation: A case study, NDT&E International, **36**: 145-156.

Ebersöhn, W. and Selig, E.T. 1994. Use of track geometry measurements for maintenance planning, Transportation Research Record, **1470**.

El-Sibaie, M. and Zhang, Y. 2004. Objective track quality indices, Transportation Research Record, **1863**: 81-87.

Federal Railroad Administration. 2014. Track and rail and infrastructure integrity compliance manual. Federal Railroad Administration, Washington DC, USA.

Federal Railroad Administration. 2011. Heavy axle load revenue service mud-fouled ballast investigation. RR11-10, Federal Railroad Administration, Washington DC, USA.

Feldman, F. and Nissen, D. 2002. Alternative testing method for the measurement of ballast fouling: Percentage void contamination. In Proceedings of the Conference on Railway Engineering, Wollongong, Australia, pp. 101-109.

Haji Adbulrazagh, P. and Hendry, M.T. 2016. Case study of use of falling weight deflectometer to investigate railway infrastructure constructed upon soft subgrades, Canadian Geotechnical Journal, **53**(12): 1991-2000.

Huang, H., Tutumluer, E., and Dombrow, W. 2009. Laboratory characterization of fouled railroad ballast behavior, Transportation Research Record, **2117**: 93-101.

Hyslip, J.P. 2002. Fractal analysis of geometry data for railway track condition assessment. PhD, University of Massachusetts Amherst, ProQuest Dissertations and Theses.

Indraratna, B., Salim, W., and Rujikiatkamjorn, C. 2011a. Advanced rail geotechnology - ballasted track. Taylor and Francis Group LLC, London UK.

Indraratna, B., Su, L., and Rujikiatkamjorn, C. 2011b. A new parameter for classification and evaluation of railway ballast fouling, Canadian Geotechnical Journal, **48**: 322-326.

Indraratna, B., Vinod, J.S., and Lackenby, J. 2009. Influence of particle breakage on the resilient modulus of railway ballast, Géotechnique, **59**(7): 643-646.

Indraratna, B., Tennakoon, N., Nimbalkar, S., and Rujikiatkamjorn, C. 2013. Behaviour of clay-fouled ballast under drained triaxial testing, Géotechnique, **63**(5): 410-419.

Li, D., Hyslip, J.P., Sussmann, T.R., and Chrismer, S.M. 2016. Railway geotechnics. Taylor & Francis Group LLC, Boca Raton, FL, USA.

Mishra, D., Kazmee, H., Tutumluer, E., Pforr, J., Read, D., and Gehringer, E.:. 2013. Characterization of railroad ballast behavior under repeated loading: Results from new large triaxial setup, Transportation Research Record, **2374**: 169-179.

Nimbalkar, S., Indraratna, B., Rujikiatkamjorn, C., and Martin, M. 2012. Effect of coal fines on the shear strength and deformation characteristics of ballast. In 11th Australia - New Zealand Conference on Geomechanics: Ground Engeineering in a Changing World, Australia, pp. 451-456.

Prescott, D. and Andrews, J. 2015. Investigating railway track asset management using a markov analysis, Proceedings of the Institution of Mechanical Engineers, Part F: Journal of Rail and Rapid Transit, **229**(4): 402-416.

Prescott, D. and Andrews, J. 2013. A track ballast maintenance and inspection model for a rail network, Proceedings of the Institution of Mechanical Engineers, Part O: Journal of Risk and Reliability, **227**(3): 251-266.

Rail Safety and Standard Board Limited. 2011. Track system requirements. United Kingdom, London.

Roghani, A. and Hendry, M.T. 2016. Continuous vertical track deflection measurements to map subgrade condition along a railway line: Methodology and case studies, Journal of Transportation Engineering, **142**(12): 04016059-1-04016059-8.

Sadeghi, J. 2010. Development of railway track geometry indexes based on statistical distribution of geometry data, Journal of Transportation Engineering, **136**(8): 693-700.

Sadeghi, J. and Askarinejad, H. 2011. Development of track condition assessment model based on visual inspection, Structure and Infrastructure Engineering: Maintenance, Management, Life-Cycle Design and Performance, **7**: 895-905.

Sadeghi, J. and Askarinejad, H. 2010. Development of improved railway track degradation models, Structure and Infrastructure Engineering: Maintenance, Management, Life-Cycle Design and Performance, **6**: 675-688.

Sadeghi, J. and Askarinejad, H. 2009. An investigation into the effects of track structural conditions on railway track geometry deviations, Proceedings of the Institution of Mechanical Engineers, Part F: Journal of Rail and Rapid Transit, **233**: 415-425.

Selig, E.T. and Waters, J.M. 1994. Track geotechnology and substructure management. Thomas Telford Ltd., London.

Selig, E.T. and Li, D. 1994. Track modulus: Its meaning and factors influencing it, Transportation Research Record, **1470**: 47-54.

Sussmann, T.R., Ruel, M., and Chrismer, S.M. 2012. Source of ballast fouling and influence considerations for condition assessment criteria, Transportation Research Record, **2289**: 87-94.

Tennakoon, N. and Indraratna, B. 2014. Behaviour of clay-fouled ballast under cyclic loading, Géotechnique, **64**(6): 502-506.

Transport Canada. 2012. Rules respecting track safety. Canada, Ottawa.

Chapter 3: A Review of Methods for Estimating Ballast Degradation using Ground-Penetrating Radar

3.1. Contribution of the Ph.D. Candidate

The detailed literature review and manuscript preparation for this chapter was performed by the Ph.D. candidate. This chapter details the theoretical physical phenomena underlying ground-penetrating radar as well as the expected effects ballast degradation will have on the associated electromagnetic material properties and resulting measurements. This is followed by a discussion of the various approaches presented in the scientific literature to estimate ballast degradation from ground-penetrating radar measurements. As supervisors, Dr. M.T. Hendry, Dr. C.D. Martin, and Dr. D.R. Schmitt reviewed all parts of the work. This chapter has been accepted for publication with the following citation;

Scanlan, K.M., Hendry, M.T., Martin, C.D., and Schmitt, D.R. 2018 (accepted May 22 2017). A Review of Methods for Estimating Ballast Degradation using Ground-Penetrating Radar. ASTM International's Selected Technical Papers 1605: Symposium on Railroad Ballast Testing and Properties.

3.2. Abstract

Significant research has been conducted over the last two decades applying non-destructive ground-penetrating radar (GPR) measurements to evaluate the amounts of both fine-grained particles (fines) and moisture present in railway ballast. This has led to the development of a variety of quantitative as well as qualitative GPR signal interpretation techniques as variations in the amount of ballast fines and moisture result in detectable changes in recorded GPR signals.

The accumulation of fines within the void space between the ballast particles decreases the size of the air voids, while also altering the bulk dielectric permittivity and electrical conductivity of the ballast layer. Changes to the bulk ballast electromagnetic properties in turn affect GPR wave traveltimes, reflection strengths, and signal attenuation, while changes in air void size can directly impact the scattering behaviour of GPR waves as they propagate through the ballast. Measurements from low-frequency (<1 GHz) GPR systems are predominately affected by the changes in bulk electromagnetic properties, whereas, high-frequency (>1 GHz) GPR measurements, while affected by changes in signal attenuation, also respond directly to changes in air void size. The majority of GPR-based detection methods infer ballast degradation based on the resulting effects on the bulk electromagnetic properties; however, direct approaches, which do not rely on these intermediary properites, also exist.

This paper presents a review of how ballast degradation, characterized by the accumulation of fines and increased moisture retention, affects the electromagnetic properties critical for GPR, and contrasts the current methods used to estimate ballast conditions from GPR measurements.

3.3. Introduction

Ground-penetrating radar (GPR) is a geophysical tool applied in a variety of civil and geotechnical engineering disciplines; including bridge and pavement inspections (Hubbard et al. 2003, Benedetto and Pensa 2007), buried utility detection (Lester and Bernold 2007), retaining wall assessments (Hugenschmidt and Kalogeropoulos 2009), and railway foundation studies (Hugenschmidt 2000, Sussmann et al. 2003). GPR owes its wide applicability to its ability to produce high-resolution images of the near subsurface in a non-destructive and time efficient manner (Benedetto and Pajewski 2015). These images are generated through the transmission and reflection of electromagnetic (EM) waves in the subsurface, which oscillate in the radar

frequency range (megahertz: 10^6 s^{-1} to gigahertz: 10^9 s^{-1}). Figure 3-1 presents the basic principles of GPR in a conventional ballasted railway foundation setting. Incident waves are generated by a transmitting antenna (represented as raypaths in Figure 3-1) and radiate through the track foundation. At contrasts in EM material properties, which may correspond to material boundaries, portions of the incident EM wave are reflected. The amplitude and timing of these back-scattered waves are recorded by the receiver antenna; thereby creating a GPR trace. Aligning traces from adjacent GPR measurements performed along the railway (i.e. either into or out of the page in Figure 3-1) produces a two-dimensional cross-section image (GPR profile) of the track foundation.

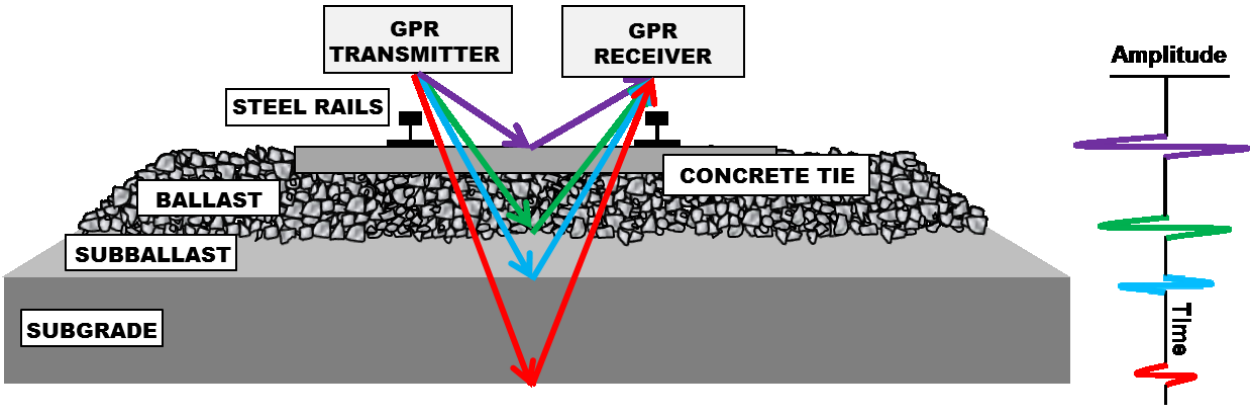

Figure 3-1. Basic GPR operating principles in a ballasted railway track foundation.

Gallagher et al. (1999) and Jack and Jackson (1999) investigated the use of GPR on railways and, specifically, the ability to detect degraded ballast. In both investigations, the authors observe distinct differences between GPR profiles collected in areas where the ballast contains a significant amount of fines within the void space (degraded ballast) and where fines are not present (clean ballast). Subsequent laboratory testing was performed to investigate how increasing amounts of both fines and moisture alter the ballast EM material properties critical for GPR (Clark et al. 2001, Su et al. 2010, De Chiara et al. 2014, Parsons et al. 2014). An increase in

moisture retention is considered to be a side-effect of degradation reducing the water-shedding capability of ballast (Selig and Waters 1994, Sussmann et al. 2012). The results of these laboratory tests stimulated the development of a suite of methods for interpreting and estimating the amount of ballast degradation present from field GPR datasets (Carpenter et al. 2004, Al-Qadi et al. 2008a, Silvast et al. 2010, Al-Qadi et al. 2010b, Shangguan et al. 2012, Khakiev et al. 2014b). These interpretation methods vary with GPR signal frequency and yield either qualitative or quantitative estimates for the amount of fines or moisture within the ballast void space.

In less than two decades, the application of GPR to the issue of ballast degradation has undergone rapid and substantial development into widely available commercial services. With such rapid development, the literature base has become widely disseminated and highly specialized. Therefore, at this point it is useful to review the fundamental aspects of rail-borne GPR applied to the evaluation of degraded ballast and summarize the different data interpretation methods that have been proposed.

This manuscript begins with a general description of the EM material properties critical for GPR as well as the fundamental aspects of EM wave behavior. The discussion then focuses on how the accumulation of fines and moisture alters the EM material properties of the ballast. Then, based on the altered EM material properties, the anticipated changes in both low- and high-frequency GPR measurements are outlined. Finally, the methods developed to interpret the GPR data and estimate the amount of fines or moisture within the ballast void space are presented.

3.4. Fundamentals of Ground-Penetrating Radar

This section presents an overview of the theoretical fundamentals of ground-penetrating radar. A basic understanding of these fundamental aspects is necessary in order to anticipate how localized ballast degradation manifests in GPR data.

3.4.1. Electromagnetic Material Properties

The fundamental aspects of EM wave behavior are described by Maxwell's equations and solutions to the resulting vector wave equation (Equation 3-1). The vector wave equation presented in Equation 3-1 considers only the electric field ($\bar{E}$) but an equivalent equation can be derived for the magnetic field ($\bar{H}$):

$$\bar{\nabla} \times \bar{\nabla} \times \bar{E} = \mu\varepsilon \frac{\partial^2 \bar{E}}{\partial t^2} - \mu\sigma \frac{\partial \bar{E}}{\partial t}. \qquad \text{[Equation 3-1]}$$

All EM waves contain inter-dependent electric and magnetic field components. The left-hand side of Equation 3-1 describes the spatial variability in the electric field component, while the right-hand side describes the spatial and temporal variability in the magnetic field component. The equivalent vector wave equation defined in terms of $\bar{H}$ describes the same scenario for the opposite EM field components. The second-order time derivative portion of the vector wave equation (when defined in terms of either $\bar{E}$ or $\bar{H}$) describes EM energy storage, while the first-order derivative describes EM energy loss. GPR is most effective when more EM energy is stored through polarization than is lost as heat. The EM material properties appearing in Equation 3-1 are the dielectric permittivity (ε: Farads per meter), the electric conductivity (σ: millisiemens per meter), and the magnetic permeability (μ: Henries per meter).

Dielectric permittivity (ε) quantifies the ability of a material to store and release electric charges (the ability to be polarized) and is related to the materials capacitance. In its most basic form, dielectric permittivity is both frequency-dependent ($\omega = 2\pi f$) and complex-valued ($j = \sqrt{-1}$):

$$\varepsilon(\omega) = \varepsilon'(\omega) - j\varepsilon''(\omega) \; . \qquad \text{[Equation 3-2]}$$

The real component of dielectric permittivity, $\varepsilon'(\omega)$ in Equation 3-2, describes the EM energy stored and released through polarization, while the imaginary component, $\varepsilon''(\omega)$, describes the EM energy lost to heat as collisions occur between particles during polarization. Earth materials can be polarized in a variety of fashions as they are exposed to EM fields of different frequencies (hence the frequency-dependence) but an in-depth discussion of these polarization mechanisms and their associated mathematical models is beyond the scope of this paper. A thorough description of the various polarization phenomena can be found in Jol (2009).

Electric conductivity (σ) quantifies the ability of a material to carry an electric current and is the reciprocal of electric resistivity (ρ: Ohm-meters). It describes the EM energy lost during GPR wave propagation as moving charges collide and produce heat. Similar to dielectric permittivity, the electric conductivity is both frequency-dependent and complex valued:

$$\sigma(\omega) = \sigma'(\omega) + j\sigma''(\omega) \; . \qquad \text{[Equation 3-3]}$$

However, at GPR signal frequencies (MHz to GHz), the imaginary component of electric conductivity and the frequency dependence of the real component are often ignored (Turner and Siggins 1994, Irving and Knight 2003). The result is a constant and real valued electric conductivity, referred to as the direct current (DC) conductivity (σ_{DC}).

The final EM material property in Equation 3-1 is the magnetic permeability (μ). Magnetic permeability quantifies the magnetization of a material when exposed to an external magnetic field. Magnetization effects often have little impact on propagating GPR waves unless significant

quantities of ferromagnetic minerals are present (iron and nickel sulphides/oxides) (Annan 2008, Jol 2009). In the absence of ferromagnetic minerals, the magnetic permeability of earth materials is assumed to be the same as that of free space (μ_o: 4π x 10^{-7} H/m).

The preceding paragraphs have established that the most critical EM material properties to consider during GPR applications are the dielectric permittivity and the electric conductivity. At this point it is convenient to define two effective material properties related to the energy storage or loss components of each material property:

$$\varepsilon^e(\omega) = \varepsilon'(\omega) \qquad \text{[Equation 3-4]}$$

and

$$\sigma^e(\omega) = \sigma_{DC} + \omega\varepsilon''(\omega)\ . \qquad \text{[Equation 3-5]}$$

The effective dielectric permittivity (Equation 3-4) describes all sources of energy storage while the effective electrical conductivity (Equation 3-5) describes all sources of energy loss during GPR wave propagation (Turner and Siggins 1994, Irving and Knight 2003). The amount of EM energy lost during GPR wave propagation through a material relative to the amount of energy stored is quantified by the loss tangent:

$$\tan\delta = \frac{\sigma^e(\omega)}{\omega\varepsilon^e(\omega)}\ . \qquad \text{[Equation 3-6]}$$

As mentioned, GPR is most effective in materials where the proportion of energy stored as polarization is much greater than the proportion lost as heat, implying that the loss tangent is much less than one.

For most applications in low-loss materials ($\tan\delta \ll 1$), the fundamental behavior of GPR waves can be understood while ignoring the frequency dependence in both effective material properties (Equations 3-4 and 3-5) as well as the imaginary dielectric permittivity component

(ε'') in the effective electric conductivity. The effective dielectric permittivity of a material is then defined as a multiple of the dielectric permittivity of free space (ε_o: 8.85 x 10^{-12} F/m);

$$\varepsilon^e = \varepsilon_r \varepsilon_o \ . \qquad \text{[Equation 3-7]}$$

The constant by which ε_0 is scaled is referred to as the relative dielectric permittivity. Table 3-1 presents ε_r and σ_{DC} values for select earth materials from Jol (2009). It is clear from Table 3-1 that increasing the amount of moisture in earth materials results in significant increases to both ε_r and σ_{DC}. Also, while ε_r varies between two and 40, σ_{DC} can range over multiple orders of magnitude.

Table 3-1. Typical relative dielectric permittivity (ε_r) and DC electrical conductivity (σ_{DC}) values for select earth materials after Jol (2009).

Material		$\boldsymbol{\varepsilon_r}$	$\boldsymbol{\sigma_{DC}}$ **[mS/m]**
Air		1	0
Freshwater (25°C)		78 to 88	0.1 to 10
Clay	Dry	2 to 20	1 to 10^2
	Wet	15 to 40	10^2 to 10^3
Sand	Dry	3 to 6	10^{-4} to 1
	Wet	10 to 30	0.1 to 10
Granite	Dry	5 to 8	10^{-5} to 10^{-3}
	Wet and Fractured	5 to 15	1 to 10
Limestone	Dry	4 to 8	10^{-7} to 10^{-3}
	Wet	6 to 15	10 to 10^2

3.4.2. GPR Signal Attenuation, Velocity, and Reflection

A plane wave (Equation 3-8) is a common solution to the vector wave equation (Equation 3-1) used to represent a propagating GPR wave. The strength of a one-dimensional electric field at

time t propagating as a plane wave in the negative x-direction with an initial amplitude of E_o is described by:

$$E = E_o \exp[j(\omega t - k(\omega)x)] \; . \qquad \text{[Equation 3-8]}$$

k in Equation 3-8 is the complex and frequency-dependent propagation constant comprised of a phase velocity term (β) and an attenuation term (α):

$$k(\omega) = \beta(\omega) - j\alpha(\omega) \; . \qquad \text{[Equation 3-9]}$$

Irving and Knight (2003) demonstrate that the phase velocity term does not significantly vary over the range of frequencies employed in GPR investigations. In contrast, the attenuation term does vary in conventional GPR applications and is described by:

$$\alpha(\omega) = \omega \left[\frac{\mu\varepsilon^e}{2}\left(\sqrt{1 + \tan^2\delta} - 1\right)\right]^{1/2} . \qquad \text{[Equation 3-10]}$$

Attenuation describes the rate at which GPR waves exponentially decay in strength as they propagate through a dielectric material. The speed at which GPR waves travel through a low-loss material is expressed as:

$$v = \frac{\omega}{\beta(\omega)} = \frac{1}{\sqrt{\mu\varepsilon^e}} \; . \qquad \text{[Equation 3-11]}$$

From Equations 3-10 and 3-11, it is clear that GPR waves attenuate more rapidly at higher frequencies and in materials with a higher ε_r value (assuming $\tan\delta$ is small), while also travelling slower in more dielectric materials. These implications from Equations 3-10 and 3-11 have a significant influence on how ballast degradation is detected in low-frequency GPR investigations.

Unlike Equation 3-8, conventional GPR plane waves are two-dimensional and the electric and magnetic field components oscillate within the plane perpendicular to the direction of propagation. Within that plane, the electric and magnetic fields are always perpendicular to one another. Under such conditions, the GPR wave can be decomposed into two independent

components (modes); the transverse electric (TE) mode and the transverse magnetic (TM) mode (Figure 3-2). The two modes are differentiated by the EM field that oscillates perpendicular to the plane of propagation (plane of the page). TE-mode EM waves are the common signals recorded in the majority of GPR investigations (Annan 2008).

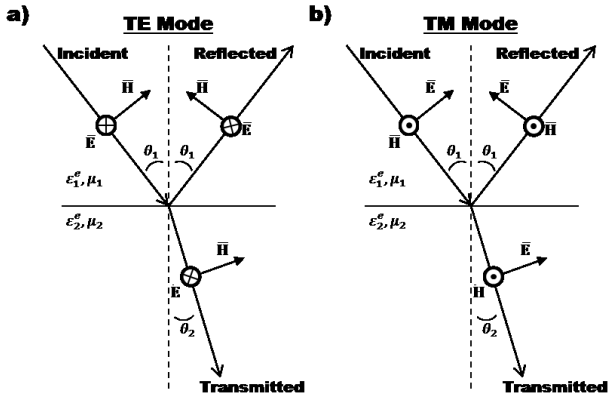

Figure 3-2. A propagating EM plane wave separated into its a) TE mode and b) TM mode components.

The strengths of the TE-mode GPR waves reflected and transmitted at an interface between materials with contrasting EM properties (Figure 3-2) are described by the reflection (R_{TE}) and transmission (T_{TE}) coefficients. The TE-mode reflection and transmission coefficients are different than those for the TM-mode. As the TM-mode is the less-common of the two GPR acquisition modes, R_{TM} and T_{TM} will not be discussed in depth here. The interested reader can find corresponding expression for R_{TM} and T_{TM} in Annan (2008) and Jol (2009). The TE-mode reflection coefficient at the interface between two low-loss materials is expressed as:

$$R_{TE} = \frac{\left(\frac{\mu_1}{\varepsilon_1^e}\right)^{-\frac{1}{2}} \cos\theta_1 - \left(\frac{\mu_2}{\varepsilon_2^e}\right)^{-\frac{1}{2}} \cos\theta_2}{\left(\frac{\mu_1}{\varepsilon_1^e}\right)^{-\frac{1}{2}} \cos\theta_1 + \left(\frac{\mu_2}{\varepsilon_2^e}\right)^{-\frac{1}{2}} \cos\theta_2}, \qquad \text{[Equation 3-12]}$$

where θ_1 and θ_2 are the angles between the reflected and transmitted rays and the vertical, while subscripts one and two refer to the material on either side of the interface (Figure 3-2). Based on Equation 3-12, the strength of a reflected TE-mode EM wave is proportional to the difference between the square-roots of the ε_r values characterizing the materials on either side of the interface; the greater the difference in ε_r, the greater the strength of the reflected wave. Finally, the amplitude of the TE-mode transmission coefficient is given by:

$T_{TE} = 1 + R_{TE}$. [Equation 3-13]

3.5. Effect of Ballast Degradation on GPR Signals

With the fundamentals of how the EM material properties affect GPR signal attenuation, velocity**,** and reflection strength established, it is now possible to evaluate the effects accumulating fines in the ballast void space, and the subsequent retention of moisture, will have on low-frequency (<1 GHz) and high-frequency (>1 GHz) GPR signals.

3.5.1. Low-Frequency GPR

The impact of ballast degradation and moisture on the ballast ε_r ($\varepsilon_{r,ballast}$) was first quantified by Clark et al. (2001). Clark et al. (2001) observed that a clean and dry ballast exhibits an $\varepsilon_{r,ballast}$ of three, while a dry ballast at the end of its service life (fully degraded) exhibits an $\varepsilon_{r,ballast}$ of 4.3. When saturated, the $\varepsilon_{r,ballast}$ of a clean and fully degraded ballast increases to 26.9 and 38.5, respectively (Clark et al. 2001). As both fines and moisture accumulate within the ballast void space, $\varepsilon_{r,ballast}$ increases. Increasing the amount of moisture in the ballast has a more dramatic effect on $\varepsilon_{r,ballast}$ than the accumulation of fines alone. This is a result of the large relative dielectric permittivity of water, which is commonly assumed to be 81 over the range of GPR frequencies employed. As both fines and moisture affect $\varepsilon_{r,ballast}$ in a similar

manner, a specific value of $\varepsilon_{r,ballast}$ is non-unique. It is possible to have multiple combinations of fines and moisture within the ballast with similar $\varepsilon_{r,ballast}$ values (Clark et al. 2001). The trends in $\varepsilon_{r,ballast}$ observed by Clark et al. (2001) are also observed in the results of De Chiara et al. (2014). Both Clark et al. (2001) and De Chiara et al. (2014) perform their tests on granitic ballast.

The impact of fines and moisture on the σ_{DC} of ballast was investigated by Parsons et al. (2014). In their study, Parsons et al. (2014) quantify the ρ_{DC} of the ballast due to the resistivity equipment used but the measured ρ_{DC} values can be readily converted to σ_{DC} (σ_{DC} is the reciprocal of ρ_{DC}). Parsons et al. (2014) observed that the ballast σ_{DC} is affected by degradation and moisture in a similar manner to $\varepsilon_{r,ballast}$. As fines and moisture are added to ballast, the ballast becomes more conductive (less resistive). Measured values for σ_{DC} range between 1.25 x 10^{-4} mS/m and 1.43 x 10^{-3} mS/m (Parsons et al. 2014).

As $\varepsilon_{r,ballast}$ and σ_{DC} increase in the presence of degraded ballast and moisture, there are predictable effects on low-frequency (<1 GHz) GPR signals. Based on Equation 3-10, degraded ballast will exhibit increased signal attenuation compared to clean ballast. In terms of propagation velocity (Equation 3-11), GPR waves will propagate slower through degraded ballast and reflections from the base of the ballast interface (Figure 3-1) will be recorded at later times relative to what would be recorded in a clean ballast layer.

The effect of ballast degradation on the reflection coefficient at the base-of-ballast interface is slightly more complicated as an assumption must be made in regards to the ε_r of the material below the ballast (Equation 3-12) if it is not known. If the ε_r of the material below the ballast is greater than the clean $\varepsilon_{r,ballast}$, as the ballast degrades the reflection coefficient will decrease and, correspondingly, the strength of the reflection in the GPR data will also decrease. If a ballast

layer degrades to a point where $\varepsilon_{r,ballast}$ equals the ε_r of the material below the ballast, no reflection will be observed. It is a subtle feature of GPR that reflections in the data may not correspond to interfaces between materials or reflections may be absent from a boundary between materials. Reflections are generated at interfaces between EM material properties, which do not always correspond to typical material interfaces. If $\varepsilon_{r,ballast}$ exceeds the ε_r of the material below the ballast, as fines or moisture accumulate within the ballast both the reflection coefficient as well as the strength of the reflection will increase.

3.5.2. High-Frequency GPR

At high GPR signal frequencies (>1 GHz), the effects of ballast degradation increasing $\varepsilon_{r,ballast}$ and σ_{DC} are the same as for lower frequencies but there is also a change in how GPR waves are scattered within the ballast. At low signal frequencies and under ideal conditions, reflected waves are backscattered only from the top and bottom of the ballast (Figure 3-1). At higher frequencies, individual air voids within the ballast begin to scatter (reflect) GPR waves. The transition between boundary reflections and volume scattering from individual air voids represents a change from Rayleigh scattering to Mie scattering (Roberts et al. 2006, Al-Qadi et al. 2008a, Al-Qadi et al. 2010b).

The transition frequency that must be attained to change between Rayleigh and Mie scattering is determined from the normalized dimension (D_N - Equation 3-14) of the individual scatterers:

$$D_N = \frac{a\pi}{\lambda}. \qquad \text{[Equation 3-14]}$$

Mie scattering becomes dominant when the sizes of the individual scatterers (a represents the scatterer diameter) approaches the GPR wavelength ($\lambda = v/f$) and the normalized dimension approaches one. At D_N values less than one, Rayleigh scattering is the dominant GPR wave

scattering mode. In ballast, typical air voids diameters range from 10 mm to 30 mm (Al-Qadi et al. 2008a).

Figure 3-3 presents D_N as a function of signal frequency and $\varepsilon_{r,ballast}$ assuming an average ballast air void diameter of 20 mm. From Figure 3-3, it is clear that Mie scattering cannot be stimulated in the ballast until the GPR signal frequency is sufficiently greater than 1 GHz. The transition between Mie scattering and Rayleigh scattering can be used to assess ballast degradation as increasing the amount of fines present within the ballast void space leads to a decrease the air void diameter. If a high enough signal frequency is used to initially stimulate Mie scattering, decreasing the air void diameter decreases D_N (Equation 3-14). Scattering will then transition from a Mie regime to a Rayleigh regime, where individual air voids no longer reflect GPR signals. GPR systems incorporating a two GHz antenna frequency are often used to differentiate between clean and degraded ballast through the transition from Mie to Rayleigh scattering (Roberts et al. 2006, Al-Qadi et al. 2008a, Al-Qadi et al. 2010b).

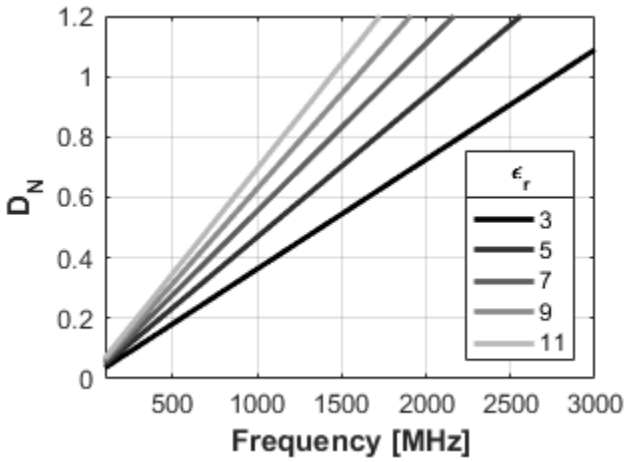

Figure 3-3. Variation in the normalized dimension (D_N) as a function of signal frequency and the relative dielectric permittivity of the ballast. Mie scattering dominates when D_N is approximately one.

3.6. GPR Interpretation Methods

The previous sections have established the fundamentals of GPR as well as the theoretical basis for how ballast degradation and moisture affect GPR data. This section details the various approaches developed for interpreting laboratory and field GPR measurements in order to estimate the amount of fines and moisture present within railway ballast. A discussion of the preliminary data processing that commonly needs to be applied to the raw GPR data prior to interpretation is beyond the scope of this paper as there is also no single best approach. The amount of preliminary data processing steps that is required is often data and application-dependent. Annan (2008), Jol (2009), and Benedetto and Pajewski (2015) all discuss common data processing techniques for GPR datasets.

Estimates of the amount of fines or moisture in the ballast are either qualitative or quantitative. Qualitative estimates yield the *relative* amount of fines or moisture present within the ballast. While quantitative approaches yield a specific numerical value. Through calibration of the quantitative estimates, it may be possible to infer either a ballast moisture content or a ballast fines index value, such as the Fouling Index (Selig and Waters 1994) or the Void Contamination Index (Indraratna et al. 2013).

Methods that have been proposed to estimate either the amount of fines or moisture within railway ballast are summarized in Table 3-2. The methods are subdivided first into low-frequency (<1 GHz) and high-frequency (>1 GHz) methods and second, by the change that ballast degradation or moisture retention exerts on the properties of the ballast layer. Each method then attempts to infer these changes in the ballast properties through its effect on the GPR signals. Table 3-2 also summarizes whether each interpretation method yields a qualitative or quantitative estimate for the amount of fines or moisture within the ballast and lists an

illustrative reference. The remainder of this paper is dedicated to the particular aspects of each interpretation method and additional references are provided when available.

Table 3-2. Summary of low- and high-frequency methods to estimate ballast degradation from GPR measurements.

Effect of Degradation or Moisture on Ballast Properties	Effect on GPR Signals	Interpretation Method	Qualitative or Quantitative	Illustrative Reference
Low-Frequency (<1 GHz) Methods				
increased $\varepsilon_{r,ballast}$	increased reflection coefficient	relative (normalized) reflectivity	Qualitative	(Khakiev et al. 2014b)
	increased signal attenuation	windowed Fourier amplitude spectrum integral	Quantitative	(Silvast et al. 2010)
	reduced propagation velocity	picked base-of-ballast reflection + known ballast thickness	Quantitative	(Clark et al. 2001)
		diffraction hyperbola fitting	Quantitative	(Carpenter et al. 2004)
		CMP/WARR curve fitting	Quantitative	(Kind 2011)
increased $\varepsilon_{r,ballast}$ and σ_{DC}	change in waveform	descriptive feature extraction after sparse signal decomposition	Qualitative	(Shao et al. 2011a)
		descriptive feature extraction after Fourier transformation	Qualitative	(Shao et al. 2011b)
High-Frequency (>1 GHz) Methods				
reduced D_N	transition from Mie to Rayleigh scattering	profile texture and Hilbert envelope	Qualitative	(Al-Qadi et al. 2008a)
		descriptive statistics of decomposed waveforms	Quantitative	(Shangguan et al. 2012)
increased $\varepsilon_{r,ballast}$	increased signal attenuation	short-time Fourier transform	Qualitative	(Al-Qadi et al. 2010b)

3.6.1. Low-Frequency (<1 GHz) Methods

As summarized in Table 3-2, the majority of low-frequency GPR interpretation methods infer the amount of fines or moisture present within railway ballast by either qualitatively or quantitatively estimating the change in $\varepsilon_{r,ballast}$. Khakiev et al. (2014b) and Khakiev et al. (2014a) investigate the effect of retained moisture and the resulting increase in $\varepsilon_{r,ballast}$ through the GPR reflection coefficient (Equation 3-12). In Khakiev et al. (2014b) the authors develop the relative (normalized) reflectivity metric, which can be used to qualitatively detect areas prone to increased ballast moisture retention based on repeated 400 MHz GPR measurements. Normalized reflectivity is the amplitude of the base-of-ballast reflection relative to the amplitude of the full GPR trace. Assuming the initial $\varepsilon_{r,ballast}$ is greater than the ε_r of the material below it, raising the ballast moisture content will increase the reflection coefficient and result in increases to both the strength of the reflection and the normalized reflectivity (Khakiev et al. 2014b).

By contrasting normalized reflectivity results calculated from GPR data acquired in a dry season with those from a wet season, sections of ballast where more moisture is being retained can be identified (Figure 3-4). The data presented in Figure 3-4 are not based on real GPR measurements and demonstrate only how retained moisture could be detected using normalized reflectivity. In the first 0.4 km of Figure 3-4, the seasonal difference in the normalized reflectivity values is less than what is observed over the last 0.6 km. The implication then is that more moisture is retained in the ballast in the last 0.6 km of the profile than is retained in the first 0.4 km (stimulating a greater seasonal change in $\varepsilon_{r,ballast}$). A quantitative estimate for how

much more moisture is being retained in the second half of Figure 3-4 cannot be determined from the normalized reflectivity results, only that more moisture is present.

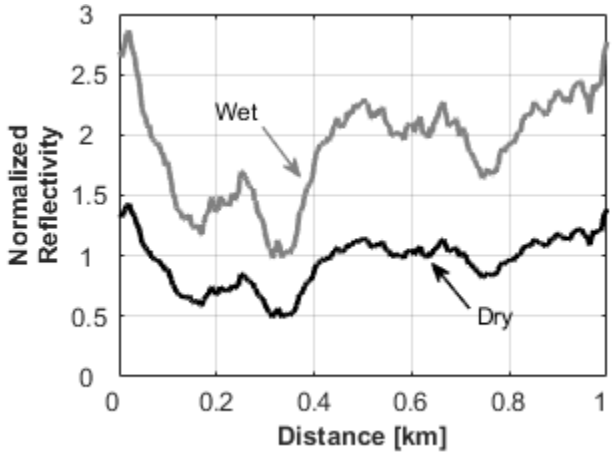

Figure 3-4. Artificial normalized reflectivity profiles illustrating how the normalized reflectivity metric can be used to infer relative increased moisture retention in the ballast. The greater seasonal difference in the ballast beyond 0.4 km would be indicative of increased moisture retention relative to the ballast prior to 0.4 km.

The effects of ballast degradation on 400 MHz GPR signal attenuation was investigated by Silvast et al. (2006) and Silvast et al. (2010). In these studies, a quantitative metric based on the integral of the Fourier amplitude spectrum was developed to estimate the amount of fines present within the ballast. As fines accumulate in the ballast void space (increasing $\varepsilon_{r,ballast}$), the higher frequency components of the GPR signal experience more attenuation than would occur in clean (fines-free) ballast (Equation 3-10). In the frequency domain, this represents a decrease in the integral of Fourier amplitude spectrum (Figure 3-5a). By selecting only the portion of the GPR signal related to signal propagation in the ballast and calculating the Fourier amplitude spectrum integral, the amount of attenuation experienced in the ballast can be quantified. Silvast et al. (2010) demonstrate that their attenuation metric can be calibrated to yield a quantitative estimate for the amount of fines present within the ballast (Figure 3-5b).

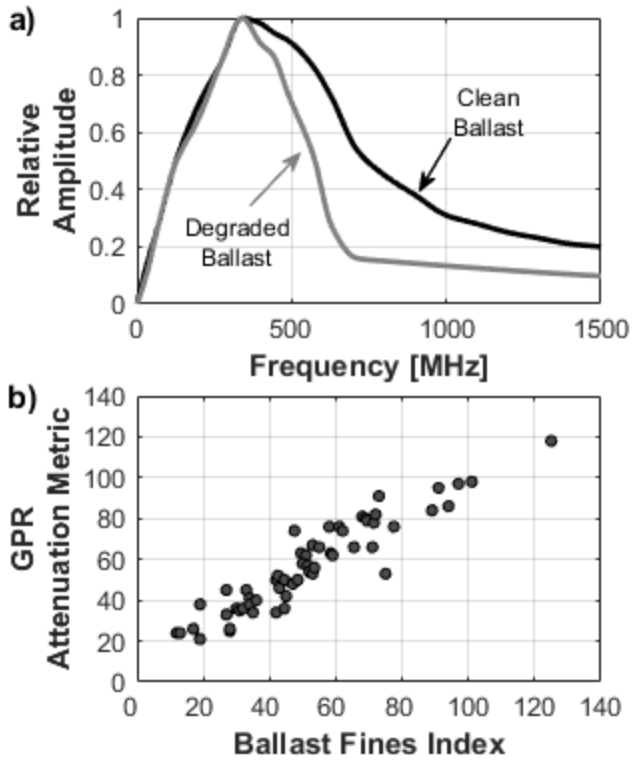

Figure 3-5. Fundamental aspects of the attenuation interpretation for low-frequency GPR data; a) a reduced Fourier amplitude spectra integral in the presence of degraded ballast due to the increased signal attenuation and b) a quantitative calibration of the GPR attenuation metric with a ballast fines index after Silvast et al. (2010).

Variations in $\varepsilon_{r,ballast}$ can also be detected through the propagation velocity. Propagation velocity methods are widely used in laboratory ballast degradation studies using GPR as both the ballast thickness and the amount of fines in the ballast are known (Clark et al. 2001, Su et al. 2010, Leng and Al-Qadi 2010, De Chiara et al. 2014, Kashani et al. 2016, Tosti et al. 2016). The GPR propagation velocity is easily determined from the known ballast thickness and the time it takes for the wave to traverse the ballast (estimated from the GPR trace – Figure 3-1). Once the propagation velocity is known, $\varepsilon_{r,ballast}$ can be calculated using Equation 3-10. When estimating the propagation velocity using this approach it is important to note that the time to the base-of-

ballast reflection read from the GPR trace (Figure 3-1) is twice the true time and must be halved. The base-of-ballast reflection time on a GPR trace is the time required for the incident wave to propagate to the base-of-ballast and for the reflected component to travel to the receiver. The calculated $\varepsilon_{r,ballast}$ can then be calibrated with the known amount of fines in the laboratory ballast model (Clark et al. 2001, Su et al. 2010, Leng and Al-Qadi 2010, De Chiara et al. 2014, Kashani et al. 2016, Tosti et al. 2016).

If the ballast thickness is not known, as is the case for the majority of field studies, more elaborate approaches are required to determine the GPR propagation velocity. Carpenter et al. (2004) demonstrate how the installation of a radar-detectable geosynthetic at the base of the ballast layer can be used to determine the GPR propagation velocity. A strip of radar-detectable geosynthetic would generate a diffraction hyperbola in the resulting GPR data (Figure 3-6). The curvature of the diffraction hyperbola is dependent on the GPR propagation velocity in the ballast and iterative curve-fitting can be used to determine $\varepsilon_{r,ballast}$. Installing a radar-sensitive geosynthetic at the base of the ballast is possible during the construction of new railways, but is more costly and disruptive for existing railways.

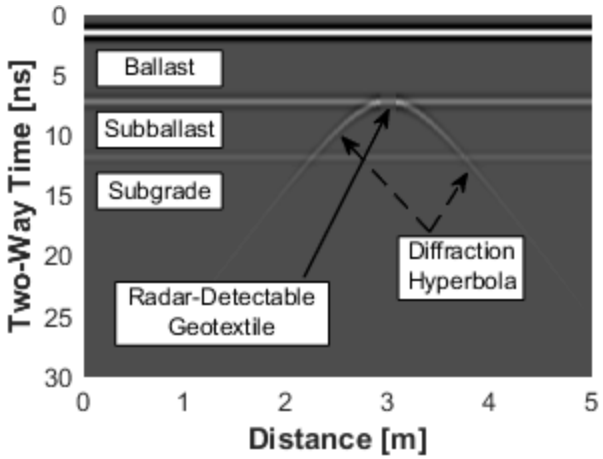

Figure 3-6. Labeled interpretation of example GPR data collected over a layered track foundation with a radar-detectable geosynthetic installed at the base of the ballast at 3.5 m. $\boldsymbol{\varepsilon_{r,ballast}}$ can be estimated from the shape of the diffraction hyperbola.

Alternatively, specialized GPR surveys such as common mid-point (CMP) and wide-angle reflection and refraction (WARR) surveys can be used to estimate GPR propagation velocities in the track foundation (Kind 2011, Cai et al. 2016). The basic design of a WARR survey and example results are presented in Figures 3-7a and 3-7b, respectively. By progressively moving the receiving antenna away from a fixed source antenna (Figure 3-7a), and assuming a flat lower interface, a hyperbolic-shaped reflection is generated in the resulting GPR data (Figure 3-7b). Similar to the diffraction hyperbola in Figure 3-6, the curvature of the hyperbolic reflected wave in Figure 3-7b is related to the GPR propagation velocity and $\varepsilon_{r,ballast}$ can be determined through curve fitting. In order for a ballast CMP or WARR survey to be conducted, EM waves from the GPR system being used must be able to penetrate deep enough such that a reflection from the base-of-ballast interface is generated (Figure 3-7a). If the GPR signal attenuates prior to the base-of-ballast interface then a hyperbolic reflection will not be observed (Figure 3-7b).

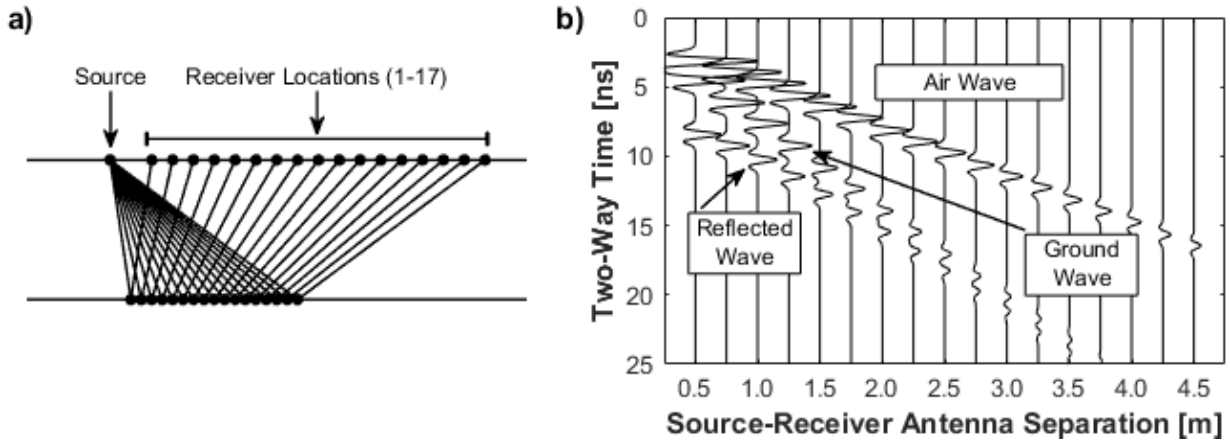

Figure 3-7. Example wide-angle reflection and refraction (WARR) GPR survey; a) survey design and b) annotated results highlighting the reflected wave from which $\boldsymbol{\varepsilon_{r,ballast}}$ can be estimated through curve fitting.

In contrast to the low-frequency interpretations methods discussed so far, Shao et al. (2011a) and Shao et al. (2011b) qualitatively detect fines within railway ballast without strict reliance on estimating the change in $\varepsilon_{r,ballast}$. In both studies, a suite of classification features are extracted from individual 800 MHz GPR traces and used to determine if the GPR data were acquired over degraded ballast. The general procedure followed by both Shao et al. (2011a) and Shao et al. (2011b) is presented in Figure 3-8. Shao et al. (2011a) utilize sparse signal decomposition to separate the GPR traces into a series of fundamental waveforms. The classification features then describe these fundamental waveforms. In Shao et al. (2011b), the classification features extracted from the GPR data are the amplitude of the Fourier amplitude spectrum at specific frequencies. By analyzing the variations in both sets of classification features, the authors could successfully differentiate between GPR traces corresponding to clean ballast and those corresponding to degraded ballast.

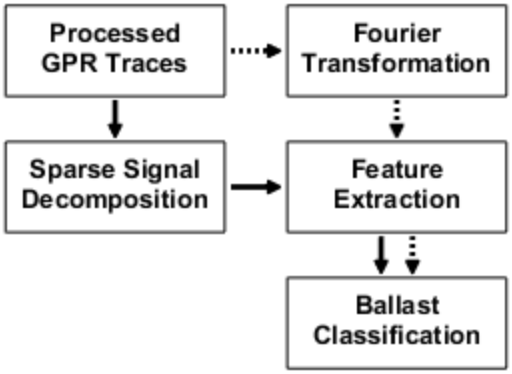

Figure 3-8. Procedure followed by Shao et al. (2011a) (solid line) and Shao et al. (2011b) (dashed line) to qualitatively differentiate between degraded and non-degraded ballast without strict reliance on estimating $\boldsymbol{\varepsilon_{r,ballast}}$.

3.6.2. High-Frequency (>1 GHz) Methods

A common method for interpreting high-frequency GPR data is based on qualitative descriptions of the change in signal scattering (transitioning from Mie to Rayleigh scattering) as ballast voids fill with fines (Roberts et al. 2006, Al-Qadi et al. 2008a, Al-Qadi et al. 2008b). When transitioning from Mie to Rayleigh scattering, GPR profiles appear less cluttered and the trace envelope (Hilbert envelope) shrinks in size. Figure 3-9 contrasts a 2 GHz GPR profile of clean ballast (Figure 3-9a) with a corresponding profile of degraded ballast (Figure 3-9b) from Al-Qadi et al. (2008b). There is a clear change in the textures of the clean ballast and degraded ballast profiles. Mie scattering in the clean ballast (Figure 3-9a) results in more reflected signal and a cluttered subsurface image, while more Rayleigh scattering in the degraded ballast (Figure 3-9b) produces lower amplitude reflections and a smoother overall profile. By visually comparing the texture in a high-frequency GPR profile along a railway, estimates for the relative amount of fines within the ballast void space can be inferred.

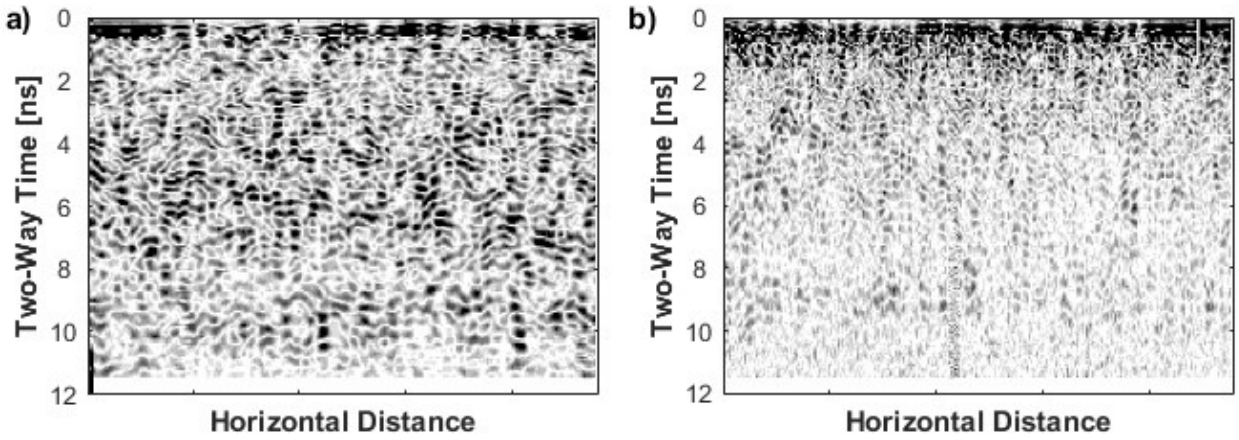

Figure 3-9. 2 GHz GPR profiles collected over a) clean ballast and b) degraded ballast after Al-Qadi et al. (2008b). GPR profiles collected over clean ballast exhibit stronger reflections and a more cluttered appearance due to Mie scattering.

Shangguan et al. (2012) and Shangguan and Al-Qadi (2014), build upon these qualitative texture descriptions and develop a procedure to quantitatively estimate the amount of fines within ballast void space. Similar to Shao et al. (2011a), their method is based on the decomposition of an individual GPR trace into a series of fundamental waveforms, followed by the extraction of descriptive statistics. The descriptive statistics used by Shangguan et al. (2012) and Shangguan and Al-Qadi (2014) all quantify the amplitude of the various fundamental waveforms after signal decomposition. As qualitatively demonstrated in Figure 3-9, GPR trace amplitudes decrease as ballast degradation increases. Through laboratory and test-pit calibration, the authors develop an inverse quantitative relationship between their descriptive statistics and the ballast Fouling Index (Selig and Waters 1994) (Figure 3-10).

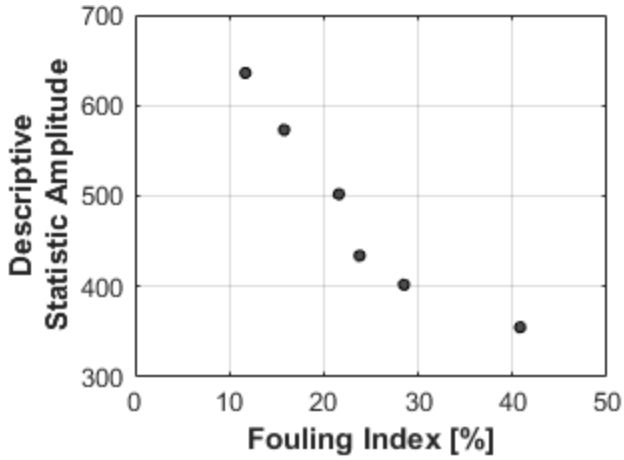

Figure 3-10. Quantitative calibration of the descriptive statistics calculated from decomposed high-frequency GPR traces with the ballast fouling index after Shangguan et al. (2012). Larger statistic amplitudes are indicative of a more cluttered GPR signal and less degraded ballast.

Unlike low-frequency data, high-frequency GPR traces can also be interpreted to vertically differentiate between clean and degraded layers within the ballast (Al-Qadi et al. 2008b, Leng and Al-Qadi 2010, Al-Qadi et al. 2010a, Al-Qadi et al. 2010b, Al-Qadi et al. 2010c). A vertical change in the concentration of fines within the ballast void space is a common side-effect of tamping. Tamping loosens and vibrates the ballast causing fines to settle to the base of the ballast layer. While the ε_r values of clean and degraded ballast are different (Clark et al. 2001, De Chiara et al. 2014), small or gradual changes in $\varepsilon_{r,ballast}$ may not result in distinct signal reflections (Al-Qadi et al. 2008a). Even in the absence of a reflected wave, high-frequency GPR signals will attenuate quicker in the presence of more degraded ballast (Equation 3-10). By representing signal attenuation along a GPR trace, relative degradation levels through the ballast can be inferred.

Attenuation along a GPR trace can be inferred though the short-time Fourier transform (STFT). The STFT is related to the S-transform (Stockwell et al. 1996) and yields a two-dimensional (time-frequency) representation of the GPR signal:

$$STFT(t,\omega) = \int x(t) * \gamma(\tau - t) * e^{-j\omega\tau} * d\tau \ . \qquad \text{[Equation 3-15]}$$

In Equation 3-15, $x(t)$ represents the GPR trace of interest and $\gamma(\tau - t)$ is a windowing function; typically a Hamming window is used (Al-Qadi et al. 2010b). The STFT result can be considered as the instantaneous Fourier amplitude spectra calculated at each time sample along the GPR trace. Similar to Figure 5a, changes in the Fourier amplitude spectra are related to the amount of signal attenuation the GPR wave experiences as it propagates through the ballast. The vertical assessment of signal attenuation is difficult to apply to low-frequency GPR data due to the limited number of reflections (compare Figure 3-6 with Figure 3-9) (Irving and Knight 2003).

Figure 3-11 presents the STFT results for two 2 GHz GPR traces: one from completely clean ballast (Figure 3-11a) and one from a layered mixture of clean and degraded ballast (Figure 3-11b). Warm colours in Figure 3-11 reflect high amplitudes in the Fourier amplitude spectra while the cool colours reflect low amplitudes. In clean ballast (Figure 3-11a), the higher frequency components of the GPR signal attenuate at a consistent rate due to normal signal attenuation. In the layered ballast case (Figure 3-11b), the upper half of the trace exhibits the same high-frequency attenuation associated with clean ballast. In the bottom half of the trace, there is an increase in the amount of signal attenuation, as illustrated by the lack of warm colours. The increase in signal attenuation is the result of an increase in the amount of fines present in the bottom half of the ballast layer (Leng and Al-Qadi 2010, Al-Qadi et al. 2010a, Al-Qadi et al. 2010b, Al-Qadi et al. 2010c). By comparing how the instantaneous Fourier amplitude spectra

change with time, changes in the relative amounts of fines with depth in the ballast can be inferred. If the attenuation observed in the STFT results could be quantified, Al-Qadi et al. (2010b) suggest a relation between the observed attenuation and the quantitative amount of fines present within the ballast void space. STFT estimates of the degree of ballast degradation can also be affected by variations in moisture content with depth (Leng and Al-Qadi 2010).

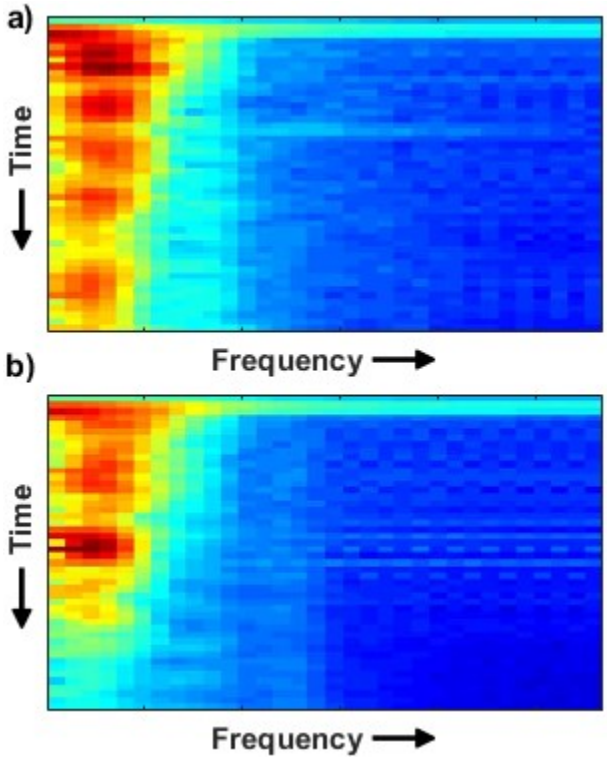

Figure 3-11. Comparison of short time Fourier transform results for GPR traces acquired in a) clean ballast and b) layered clean and degraded ballast after Al-Qadi et al. (2010b). Increased signal attenuation in the degraded ballast leads to an absence of warm colours in the bottom half of the plot.

3.6.3. Comparison of Low- and High-Frequency Methods

A comparison of the low- and high-frequency methods presented highlights one major difference between the two types. Low-frequency methods infer ballast degradation primarily through

changes in GPR signal behaviour and relate those changes to changes in the EM material properties. An implicit assumption in the low-frequency methods is then that all changes in GPR signal propagation (attenuation and speed) as well as reflection, result from the degraded ballast. The effects of any other factors that may alter either the EM material properties of the ballast or the GPR signal behaviour are not considered (for example, ballast moisture contents, ballast thicknesses, and subballast material types). In contrast, high-frequency methods rely on detecting changes in the air void sizes within the ballast. These changes in the air void sizes are directly observable from the GPR data without relying on an intermediate material property.

A potential limitation of the high-frequency GPR methods is the trade-off between resolution and depth-penetration. The ability to resolve individual air voids with high-frequency GPR is balanced by limited signal penetration into the track foundation. Low-frequency GPR methods rely on intermediate EM material properties to infer ballast degradation, but the GPR data may also contain information on the lower foundational layers due to greater signal penetration (Hugenschmidt 2000, Sussmann et al. 2003, Cai et al. 2016). Which approach is ultimately best-suited for a particular investigation will depend on the specific aims of that study.

3.7. Conclusions

The past two decades have seen significant development in the application of ground-penetrating radar to railway ballast degradation and moisture detection studies. As an alternative to conventional sampling, sieving, trenching, and test-pits, GPR technology is well-suited for railway ballast investigations as it is capable of delivering high-resolution information about the very near subsurface in a time efficient and non-destructive manner. As fines accumulate and moisture is retained within the void space during ballast degradation, the electromagnetic (EM) properties critical for GPR signal propagation and reflection are altered. These alterations lead to

predictable changes in the backscattered signals recorded during GPR data collection. A wide variety of interpretation methodologies have been proposed to both qualitatively and quantitatively describe these changes.

The methods used to estimate ballast degradation levels from rail-borne GPR data classify into two main types: (1) low-frequency methods and (2) high-frequency methods. Low-frequency methods relate changes in the ballast EM properties solely to the effects of additional fines or moisture within the ballast layer. As such, degraded ballast manifests in the GPR data as an increase in the reflection strength of the base-of-ballast interface, increased signal attenuation, and a decrease in the GPR propagation velocity. Qualitatively or quantitatively describing these changes yields an estimate for the degradation state of the ballast. In contrast, high-frequency methods rely on changes in scattering behaviour as the void space within ballast is progressively filled during degradation. Transitions from Mie to Rayleigh scattering are clearly visible in the GPR profiles and present a quick and reliable way to visually differentiate between clean and degraded ballast. It is possible to produce quantitative estimates for the amount of fines present within the ballast if the amount of Mie scattering can be quantitatively defined. Furthermore, by representing the instantaneous attenuation along high-frequency GPR traces, vertical changes in ballast degradation can also be detected.

In order to accurately and reliably quantify ballast degradation from low-frequency GPR measurements, it is critical to ensure that any detected change in the backscattered signal is a result of degradation-induced changes in the bulk EM material properties of the ballast. Changes to the base-of-ballast interface reflection strength, signal attenuation rate, or GPR propagation velocity that are not a result of ballast degradation will propagate into the estimate for the amount of fines within the ballast. If these changes are not accounted for, the accuracy and

reliability of the degradation estimate will be reduced. Additional research is required to characterize the factors behind these changes and their impact on low-frequency ballast degradation estimates. A more direct relationship between ballast degradation and GPR measurements exists at higher signals frequencies, when actual changes in air void sizes can be detected. However, in order to quantify the amount of fines present, signal scattering must be continually calibrated against field measurements of ballast degradation. Furthermore, a quantitative approach for estimating high-frequency signal attenuation has yet to be presented. Due to the variety of ways in which ballast degradation manifests as detectable changes in GPR measurements, combined low- and high-frequency interpretations may ultimately lead to a more reliable quantification of ballast degradation than either method individually.

3.8. Acknowledgments

This research was made possible by the Canadian Rail Research Laboratory (CaRRL) (www.carrl.ca), which is funded by the Natural Sciences and Engineering Research Council of Canada (NSERC), Canadian Pacific Railway, Canadian National Railway, the Association of American Railways – Transportation Technology Center Inc., the National Research Council of Canada, Transport Canada and Alberta Innovates – Technology Futures.

3.9. References

Al-Qadi, I.L., Xie, W., and Roberts, R. 2010a. Optimization of antenna configuration in multiple-frequency ground penetrating radar system for railroad substructure assessment, NDT&E International, **43**(1): 20-28.

Al-Qadi, I.L., Xie, W., and Roberts, R. 2008a. Scattering analysis of ground-penetrating radar data to quantify railroad ballast contamination, NDT&E International, **41**(6): 441-447.

Al-Qadi, I.L., Xie, W., and Roberts, R. 2008b. Time-frequency approach for ground penetrating radar data analysis to assess railroad ballast condition, Research in Nondestructive Evaluation, **19**: 219-237.

Al-Qadi, I.L., Xie, W., Jones, D.L., and Roberts, R. 2010b. Development of a time-frequency approach to quantify railroad ballast fouling condition using ultra-wide band ground-penetrating radar data, International Journal of Pavement Engineering, **11**(4): 269-279.

Al-Qadi, I.L., Xie, W., Roberts, R., and Leng, Z. 2010c. Data analysis techniques for GPR used for assessing railroad ballast in high radio-frequency environment, Journal of Transportation Engineering, **136**(4): 392-399.

Annan, A.P. 2008. Ground penetrating radar principles, procedures & applications. Sensors & Software Inc., Mississauga, Ontario, Canada.

Benedetto, A. and Pajewski, L. 2015. Civil engineering applications of ground penetrating radar. Springer International Publishing, Switzerland.

Benedetto, A. and Pensa, S. 2007. Indirect diagnosis of pavement structural damages using surface GPR reflection techniques, Journal of Applied Geophysics, **62**: 107-123.

Cai, J.Q., Liu, S.X., Fu, L., and Feng, Y.Q. 2016. Detection of railway subgrade moisture content by GPR. In 16th International Conference on Ground Penetrating Radar (GPR), pp. 1-5.

Carpenter, D., Jackson, P.W., and Jay, A. 2004. Enhancement of the GPR method of railway trackbed investigation by the installation of radar detectable geosynthetics, NDT&E International, **37**(2): 95-103.

Clark, M.R., Gordon, R., Kemp, T., and Forde, M.C. 2001. Electromagnetic properties of railway ballast, NDT&E International, **34**(5): 305-311.

De Chiara, F., Fontul, S., and Fortunato, E. 2014. GPR laboratory tests for railway materials dielectric properties assessment, Remote Sensing, **2014**(6): 9712-9728.

Gallagher, G.P., Leiper, Q., Williamson, R., Clark, M.R., and Forde, M.C. 1999. The application of time domain ground penetrating radar to evaluate railway track ballast, NDT&E International, **32**(8): 463-468.

Hubbard, S.S., Zhang, J., Monteiro, P.J.M., Peterson, J.E., and Rubin, Y. 2003. Experimental detection of reinforcing bar corrosion using nondestructive geophysical techniques, ACI Materials Journal, 6: 501-510.

Hugenschmidt, J. 2000. Railway track inspection using GPR, Journal of Applied Geophysics, **43**(2): 147-155.

Hugenschmidt, J. and Kalogeropoulos, A. 2009. The inspection of retaining walls using GPR, Journal of Applied Geophysics, **67**: 335-344.

Indraratna, B., Tennakoon, N., Nimbalkar, S., and Rujikiatkamjorn, C. 2013. Behaviour of clay-fouled ballast under drained triaxial testing, Géotechnique, **63**(5): 410-419.

Irving, J.D. and Knight, R. 2003. Removal of wavelet dispersion from ground-penetrating radar data, Geophysics, **68**(3): 960-970.

Jack, R. and Jackson, P. 1999. Imaging attributes of railway track formation and ballast using ground probing radar, NDT&E International, **32**(8): 457-462.

Jol, H. 2009. Ground penetrating radar theory and applications. Elsevier Science, Oxford, United Kingdom.

Kashani, H.F., Ho, C.L., Clement, W.P., and Oden, C.P. 2016. Evaluating the correlation between the geotechnical index and the electromagnetic properties of fouled ballasted track by a full-scale laboratory model, Transportation Research Record, **2545**: 66-78.

Khakiev, Z., Shapovalov, V., Kruglikov, A., and Yavna, V. 2014a. GPR determination of physical parameters of railway structural layers, Journal of Applied Geophysics, **106**: 139-145.

Khakiev, Z., Shapovalov, V., Kruglikov, A., Morozov, A., and Yavna, V. 2014b. Investigation of long term moisture changes in trackbeds using GPR, Journal of Applied Geophysics, **110**: 1-4.

Kind, T. 2011. GPR antenna array for the inspection of railway ballast. In National Seminar & Exhibition on Non-Destructive Evaluation, pp. 281-285.

Leng, Z. and Al-Qadi, I.L. 2010. Railroad ballast evaluation using ground-penetrating radar: Laboratory investigation and field vindication, Journal of the Transportation Research Board, **2159**: 110-117.

Lester, J. and Bernold, L.E. 2007. Innovative process to characterize buried utilities using ground penetrating radar, Automation in Construction, **16**: 546-555.

Parsons, R.L., Rahman, A.J., Han, J., and Glavinivh, T.E. 2014. Track ballast fouling and permeability characterization by using resistivity, Transportation Research Record, **2448**: 133-141.

Roberts, R., Rudy, J., Al-Qadi, I.L., Tutumluer, E., and Boyle, J. 2006. Railroad ballast fouling detection using ground penetrating radar - A new approach based on scattering from voids. In Proceedings of the 9th European Conference on Non-Destructive Testing , Berlin, Germany, pp. 1-8.

Selig, E.T. and Waters, J.M. 1994. Track geotechnology and substructure management. Thomas Telford Ltd., London.

Shangguan, P. and Al-Qadi, I.L. 2014. Content-based image retrieval approaches to interpret ground penetrating radar data, Construction and Building Materials, **69**: 10-17.

Shangguan, P., Al-Qadi, I.L., and Leng, Z. 2012. Development of wavelet technique to interpret ground-penetrating radar data for quantifying railroad ballast conditions, Journal of the Transportation Research Board, **2289**: 95-102.

Shao, W., Bouzerdoum, A., and Phung, S.L. 2011a. Sparse signal decomposition for ground penetrating radar. In 2011 IEEE Radar Conference, Kansas City, MO, USA, pp. 453-457.

Shao, W., Bouzerdoum, A., Phung, S.L., Su, L., Indraratna, B., and Rujikiatkamjorn, C. 2011b. Automatic classification of ground-penetrating-radar signals for railway-ballast assessment, IEEE Transactions on Geoscience and Remote Sensing, **49**(10): 3961-3972.

Silvast, M., Nurmikolu, A., Wiljanen, B., and Levomaki, M. 2010. An inspection of railway ballast quality using ground penetrating radar in finland, Proceedings of the Institution of Mechanical Engineers, Part F: Journal of Rail and Rapid Transit, **224**: 345-351.

Silvast, M., Levomaki, M., Nurmikolu, A., and Noukka, J. 2006. NDT techniques in railway structure analysis. In Proceedings of the 7th World Congress on Railway Research, Montreal, Canada, pp. 1-12.

Stockwell, R.G., Mansinha, L., and Lowe, R.P. 1996. Localization of the complex spectrum: The S transformation, IEEE Transactions on Signal Processing, **44**(4): 998-1001.

Su, L., Rujikiatkamjorn, C., and Indraratna, B. 2010. An evaluation of fouled ballast in a laboratory model track using ground penetrating radar, Geotechnical Testing Journal, **33**(5): 1-8.

Sussmann, T.R., Ruel, M., and Chrismer, S.M. 2012. Source of ballast fouling and influence considerations for condition assessment criteria, Transportation Research Record, **2289**: 87-94.

Sussmann, T.R., Selig, E.T., and Hyslip, J.P. 2003. Railway track condition indicators from ground penetrating radar, NDT&E International, **36**(3): 157-167.

Tosti, F., Benedetto, A., Calvi, A., and Bianchini Ciampoli, L. 2016. Laboratory investigations for the electromagnetic characterization of railway ballast through GPR. In 16th International Conference of Ground Penetrating Radar (GPR), pp. 1-6.

Turner, G. and Siggins, A.F. 1994. Constant Q attenuation of subsurface radar pulses, Geophysics, **59**(8): 1192-1200.

Chapter 4: Evaluating the Impact of Ballast Undercutting on the Roughness of Track Geometry over Different Subgrade Conditions

4.1. Contribution of the Ph.D. Candidate

All of the work presented in this chapter was performed by the Ph.D. candidate, including: literature review, data analysis and interpretation as well as manuscript preparation. This chapter details the use of historical ballast undercutting records to validate, using field observations, that reductions in the amount of fines present within railway ballast leads to reductions in long-term track geometry variability. As supervisors, Dr. M.T. Hendry and Dr. C.D. Martin reviewed all parts of the work. This chapter has been published with the following citation;

Scanlan, K.M., Hendry, M.T., and Martin, C.D. 2017. Evaluating the impact of ballast undercutting on the roughness of track geometry over different subgrade conditions. Proceedings of the Institution of Mechanical Engineers Part F: Journal of Rail and Rapid Transit, in press, online: DOI: 10.1177/0954409717720347.

4.2. Abstract

The progressive degradation of railway ballast is often cited as a primary factor contributing to the development of track roughness, while ballast renewal (undercutting) attempts to manage its long-term development. Soft subgrades have been shown to strongly influence track geometry; and are a contributing factor that has not been considered during conventional track maintenance. This study evaluated the impact of undercutting on long-term trends in track geometry roughness, and what impact softer subgrades had on the effectiveness of undercutting. A combined 6.90 km of Class II through IV heavy-haul track in Western Canada (undercut in 2010

and 2011) formed the basis for this analysis. Annual traffic on these sections typically totals 50 million gross tonnes. Long-term trends in the track crosslevel, alignment, and surface roughness after ballast renewal were derived from 50 track geometry surveys carried out over a five-year period (2010-2015). The results showed that undercutting significantly reduced track roughness over sand, silt, clay, or till subgrades; however, it was often ineffective when used over soft organic subgrades. Thus, while ballast degradation is primary cause of track roughness in segments constructed on mineral subgrades, it is not a mechanism resulting in track geometry roughness over soft organic soils.

4.3. Introduction

There is a strong notion in railway engineering that ballast degradation is a root cause of the uneven ballast deformations that lead to rough track geometry. This is evident in its inclusion in both the Canadian and United States track safety rules (Transport Canada 2012, Federal Railroad Administration 2014). Specifically, the FRA regulations allow for inspectors to issue citations for degraded ballast should corroborating "geometry conditions" (Federal Railroad Administration 2014) be present. The regulations are supported by findings from various researchers that degraded ballast, containing a significant portion of fine-grained material relative to new ballast (Figure 4-1), influences the deformation and strength characteristics of the railway foundation, and thus leaves the overlying track susceptible to the accumulation of roughness (Selig and Waters 1994, Huang et al. 2009, Sussmann et al. 2012, Indraratna et al. 2013, Mishra et al. 2013). Sadeghi and Askarinejad (2009) demonstrate this relationship by associating locations of increasing horizontal and vertical deviations in track geometry with the presence of lower quality ballast. The effect of ballast degradation is also a critical component of models developed to predict track geometry (Sadeghi and Askarinejad 2010). Recent modeling

algorithms developed to aid in railway network asset management consider changes in track roughness through time to be driven solely by ballast degradation (Andrews 2012, Prescott and Andrews 2013, Andrews et al. 2014).

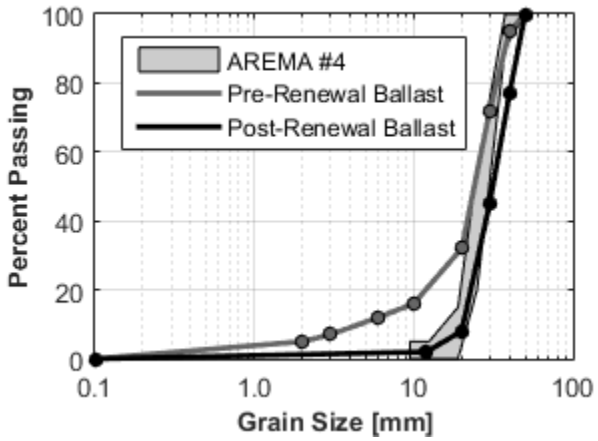

Figure 4-1. AREMA #4 recommended particle grain size distribution for new ballast and example grain size distributions for ballast pre-renewal and post-renewal after Li et al. (2016).

While ballast degradation is a primary cause of track roughness, additional factors such as rail joints and soft subgrades may also influence the track geometry (Askarinejad et al. 2010, Zong et al. 2013, Roghani and Hendry 2016). Askarinejad et al. (2010) and Zong et al. (2013) observed rough track at the locations of insulated rail joints, which was concluded to be a result of dynamic loading, and this roughness was attributed to the degradation of ballast at these locations. New research presented in Roghani and Hendry (2016) demonstrated that soft subgrades result in increased vertical track deflections. Therefore, if vertical track deflections correlate with track geometry measurements, soft subgrades may also contribute to track roughness. Conventional track maintenance methods, such as undercutting (ballast renewal), manage track geometry by removing fines that have accumulated within the ballast void space. The potential for soft subgrade related contributions to track geometry variability must be

considered by railway operators in order to efficiently manage track roughness with ballast renewal programs.

The research described in this paper investigates this suggestion that soft subgrades can have a significant contribution to track roughness. This is accomplished through an analysis of track geometry surveys and undercutting ballast renewal programs carried out between April 2010 and March 2015 along a section of heavy-haul railroad in Western Canada. Decisions regarding the track sections selected for ballast renewal along this railway are made by the railway operator; primarily in response to increased track roughness as well as the visual identification of degraded ballast. To the authors knowledge, no additional non-destructive testing (De Bold et al. 2015) or systematic visual inspection (Sadeghi and Askarinejad 2009, Sadeghi and Askarinejad 2010, Sadeghi and Askarinejad 2011) of the ballast conditions was performed by the railway operator prior to selecting these sections of track for ballast renewal**.** This paper discusses the observed changes in the long-term trends in track geometry measurements prior to and after the ballast renewal program in the presence of soft and organic subgrades as well as relatively stiffer mineral (sand, silt, clay and till) subgrades. After analyzing the changes in the long-term trends in track geometry after undercutting, potential sources for these changes are described.

4.4. Datasets

The >300 km railway subdivision used for this study is situated in Alberta, Canada with annual freight loads in excess of 50 million gross tonnes (MGT). Maximum allowable train speeds vary within the subdivision between 40 km/h (25mph – Class II) and 97 km/h (60 mph – Class IV). The 2010 and 2011 ballast maintenance records provided by the operator indicate that ballast renewal took place over 11 km of the subdivision between August 2010 and November 2011. Approximately 2.45 km of these records were found to lack sufficient information to be included

in this study. The remaining undercutting operations used for this study varied in length between 10 m and 3.21 km, and covered a total distance of 8.55 km. Continuously welded rail (CWR) and concrete ties are the dominant rail and ties type across the 8.55km of undercut railway.

Subgrade conditions under the track were determined using the Agricultural Region of Alberta Soil Inventory Database (AGRASID). The AGRASID database was accessed through the Alberta Soil Information Viewer map (Alberta Agriculture and Forestry 2012). Soil conditions were identified from the AGRASID database using Global Positioning System (GPS) coordinates. Dominant soil materials are reported in the AGRASID database at a scale of 1:100,000; therefore localized pockets of other soil types too small to be delineated on the Alberta Soil Information Viewer map may be present.

Fifty historical track geometry records from April 2010 through March 2015 were analyzed to characterize the behavior of the track geometry. Over this timeframe, the geometry of the track within the undercut track segments was measured an average of 32 times (approximately six times per year). The exact number of geometry surveys covering each undercut segment varied slightly as each geometry survey did not span the entire length of the subdivision. Hence, certain segments were covered more than others. These measurements were primarily collected during the spring, summer and fall with only one set acquired during the winter (February 2012).

A standard set of track geometry measures were recorded during each survey at 0.30 m (1 ft) increments. These measures included, but were not limited to, the track crosslevel, alignment and surface. Track crosslevel quantifies the difference in elevation between the top of the two rails, while alignment and surface quantify the horizontal and vertical differences between the true rail profile and an 18.9 m (62 foot) long straight-line datum (chord) (Li et al. 2016). The alignment and surface measurements are made at the mid-point of the reference chord and are then

commonly referred to as a mid-chord offset (MCO). Due to the fixed length of the reference chord and its varying orientation along the rails, mechanical filtering removes long-wavelength irregularities from the MCO measurements that would have otherwise been measured from a stationary reference point (Li et al. 2016).

Figure 4-2 presents examples of crosslevel (Figures 4-2a and 4-2d), alignment (Figures 4-2b and 4-2e), and surface (Figures 4-2c and 4-2f) track geometry data collected over mineral (dominantly sand/silt; Figures 4-2a-c) and organic (dominantly peat; Figures 4-2d-f) subgrades at five different times throughout the study period. Deviations in the track geometry data are of similar scale between the repeated surveys, as well as between the two subgrade types. Track crosslevel, alignment and surface measurements were selected for this investigation as they have been identified as the most responsive to changes in ballast quality by both Transport Canada (2012) and the FRA (2014). Sadeghi and Askarinejad (2009) demonstrate that variability in track alignment and surface has a stronger correlation with ballast conditions than either track gauge or twist. Finally, track crosslevel and surface are the track geometry variables the most likely to be related to vertical track deflections.

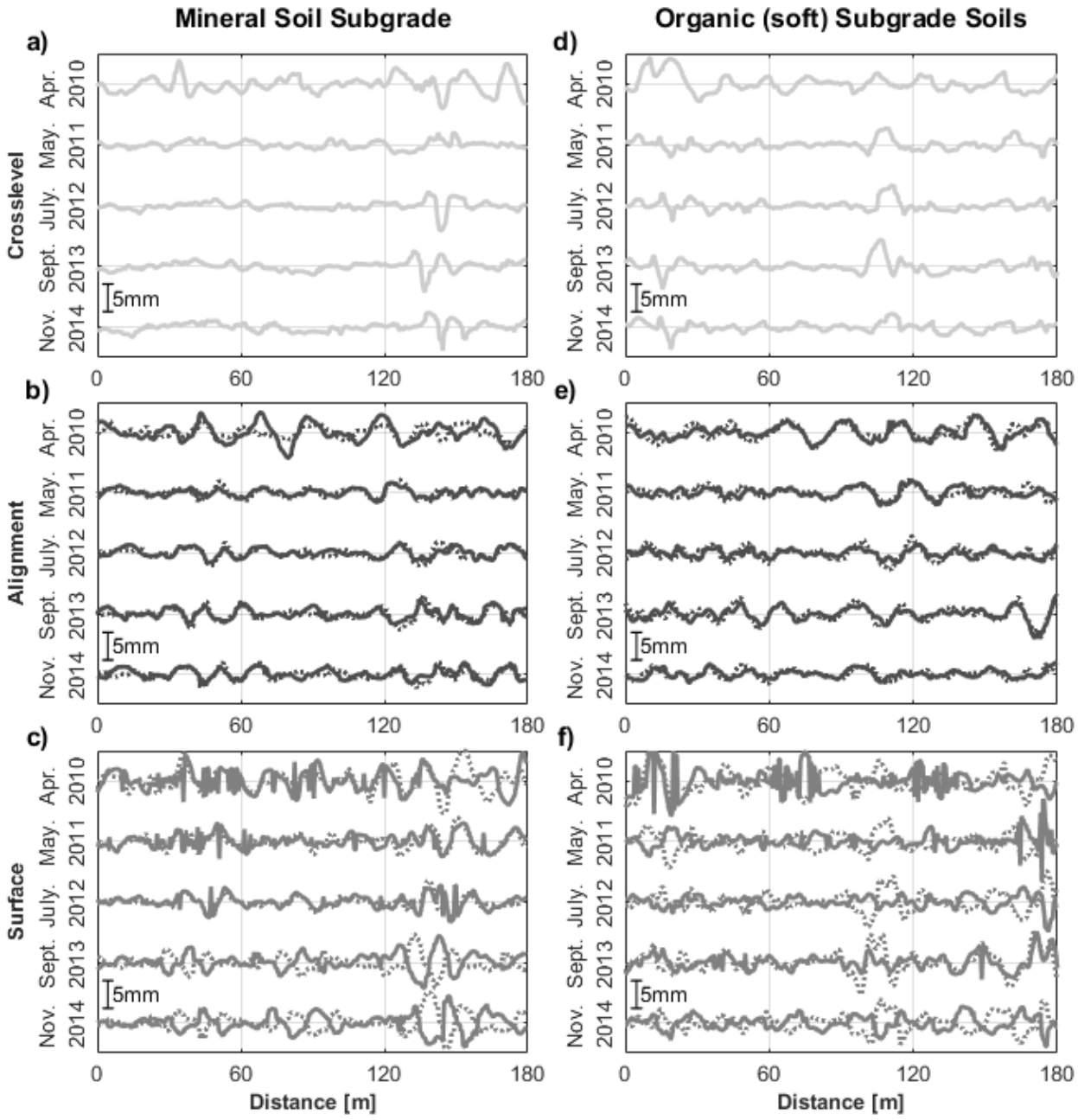

Figure 4-2. Example repeated crosslevel [a) and d)], alignment [b) and e)], and surface [c) and f)] datasets collected over mineral [a)-c)] and organic [d)-f)] subgrades. Solid and dashed lines in b), c), e), and f) represent measurements for the left and right rail, respectively.

4.5. Quantification of Track Roughness

There are two common approaches used in railroad operations to evaluate if the track geometrical roughness is acceptable after collecting track geometry data. The first is to identify locations where the track geometry exceeds defined thresholds and the second is to evaluate the variability, i.e. roughness, of the track geometry. The former is the basis of North American regulations and the more stringent thresholds that are often imposed by the operator so as to avoid track conditions degrading below the regulated standard (Transport Canada 2012, Federal Railroad Administration 2014).

The geometry measurements included in this study were from well-maintained track with few locations at which the measurements exceeded either regulator- or operator-imposed thresholds. As such, the only practical method to track the trend in track geometry with time was to compute the track roughness from each track geometry dataset. This provided a continuous measure of track roughness across the study sites to quantify the effectiveness of any remedial measures.

The roughness of track geometry measurements has commonly been expressed through the standard deviation (σ) of the track geometry data within a length of track (Sadeghi 2010, Andrews 2012, Audley and Andrews 2013, Andrews et al. 2014). Standard deviations are useful when defining a single track roughness metric within discrete segments of a railway, which is why they have been chosen for this analysis. Other roughness measurements, such as the running roughness (Ebersöhn and Selig 1994), yield a continuous track roughness profile.

The σ of N track geometry measurements within a length of track is defined by

$$\sigma = \sqrt{\frac{1}{N}\sum_{i=1}^{N}(d_i - \mu)^2}, \qquad \text{[Equation 4-1]}$$

where d_i represents the individual track geometry measurements and μ represents the mean of the N measurements. Once calculated for a specific track geometry variable, the σ then quantifies the roughness in that track geometry measure within that length of track. The σ calculated from left and right rail geometry measurements (for alignment and surface) are commonly averaged into a single roughness estimate (Andrews 2012, Audley and Andrews 2013). Many Track Quality Indices (TQI) arithmetically combine the σ of multiple track geometry measures to derive an overall roughness index for a section of track (Berawi et al. 2010, Sadeghi 2010, Scanlan et al. 2016). In this analysis, the σ values calculated for the crosslevel, alignment and surface were analyzed individually, though the alignment and surface σ values represent averages of the individual left and right rail σ measurements.

The lengths of track over which σ was evaluated were set to a constant length such that all roughness estimates were derived using the same number of data points and the results were comparable. A σ segment length of 201 m ($\frac{1}{8}^{th}$ mile) is prescribed in the United Kingdom (Rail Safety and Standard Board Limited 2011, Andrews 2012, Audley and Andrews 2013) and a 250 m length is used in the calculation of some TQI (Sadeghi 2010). No data-dependent justification is given for why lengths of 201 or 250 m are prescribed; they are taken to be practical lengths used to assess track geometry as they are simple fractions of miles and kilometers, respectively. Figure 4-3 presents the range of σ amplitudes calculated from the measured geometry over a 1 km section of undercut track with segment lengths varying between 10 and 250 m. The choice of which segment length to use in this analysis represented a balance between effectively capturing the spread in σ, maintaining a statistically significant number of data points during σ calculation and maximizing the spatial resolution of the roughness estimates. As such, a 60 m segment length was chosen as it best represented these three competing considerations.

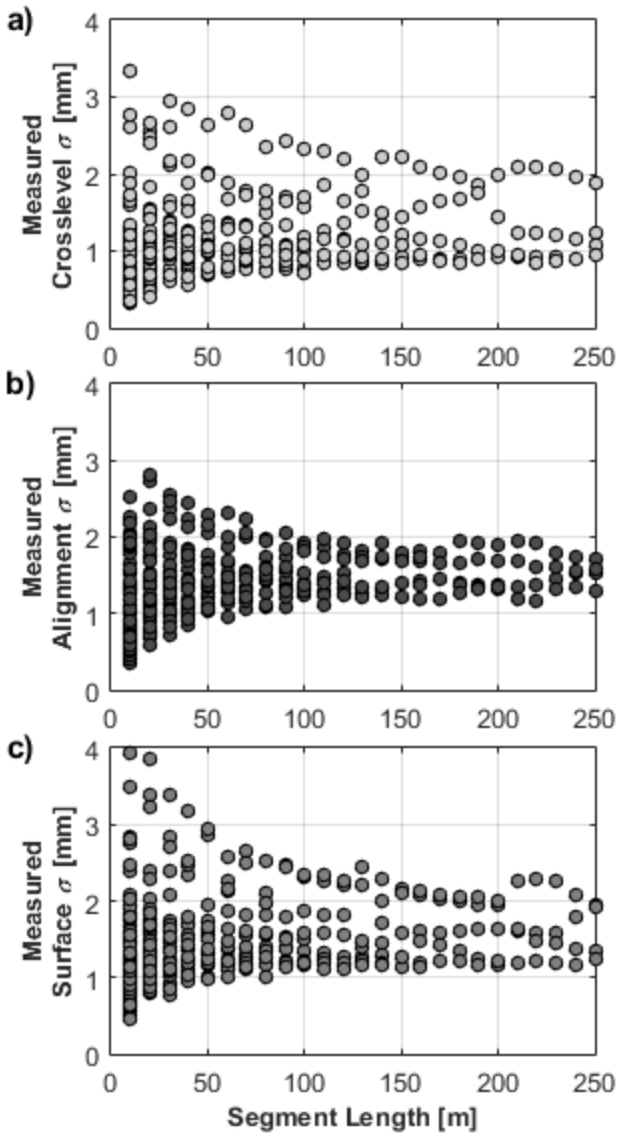

Figure 4-3. Variation in a) crosslevel, b) alignment, and c) surface standard deviation (σ) as a function of segment length.

Subdivision of the undercut track segments was done with the first 60 m segment located in the middle of each of the undercut sections, with additional segments extending towards the limits. This resulted in two sections at either end with lengths less than 60 m, which were removed from the data set. Locating the first 60m segment in the center of the ballast renewal and excluding data from the edges, minimizes the impact of incomplete ballast renewal before the undercutting

reaches its desired operational depth. Similarly, sections of track that were undercut but less than 60 m in length were also removed from the data set. The final data set consisted of 115 60 m-long segments that covered a total length of 6.90 km.

Sand and silt soils underlie the majority (62) of the undercut segments, whereas peat (25), heavy clay (16), and glacial till (9) soils comprise the dominant soil types underlying the remaining segments. Subgrade conditions underlying three undercut segments could not be identified as these segments were beyond the area covered by the AGRASID database. Only one segment was on Class II track; whereas, 18 were on Class III, and 96 on Class IV track. All undercutting on Class III track was over organic subgrades.

Once σ had been calculated for each segment and for each track geometry survey, trends in roughness were developed. Figure 4-4 presents the trends in σ considering the five example track geometry datasets presented in Figure 4-2. The trends in Figure 4-4 are divided by geometry measure (crosslevel in Figures 4-4a and 4-4d; alignment in Figures 4-4b and 4-4e; surface in Figures 4-4c and 4-4f) and by subgrade type (mineral in Figures 4-4a-c; organic in Figures 4-4d-f). The different symbols in Figure 4-4 correspond to one of the individual 60 m-long segments in Figure 4-2. For each geometry measure, similar σ levels were observed independent of the material on which the track segment was founded. Only through the trends in σ developed for each track geometry survey can the impact of degraded ballast and subgrade type be evaluated.

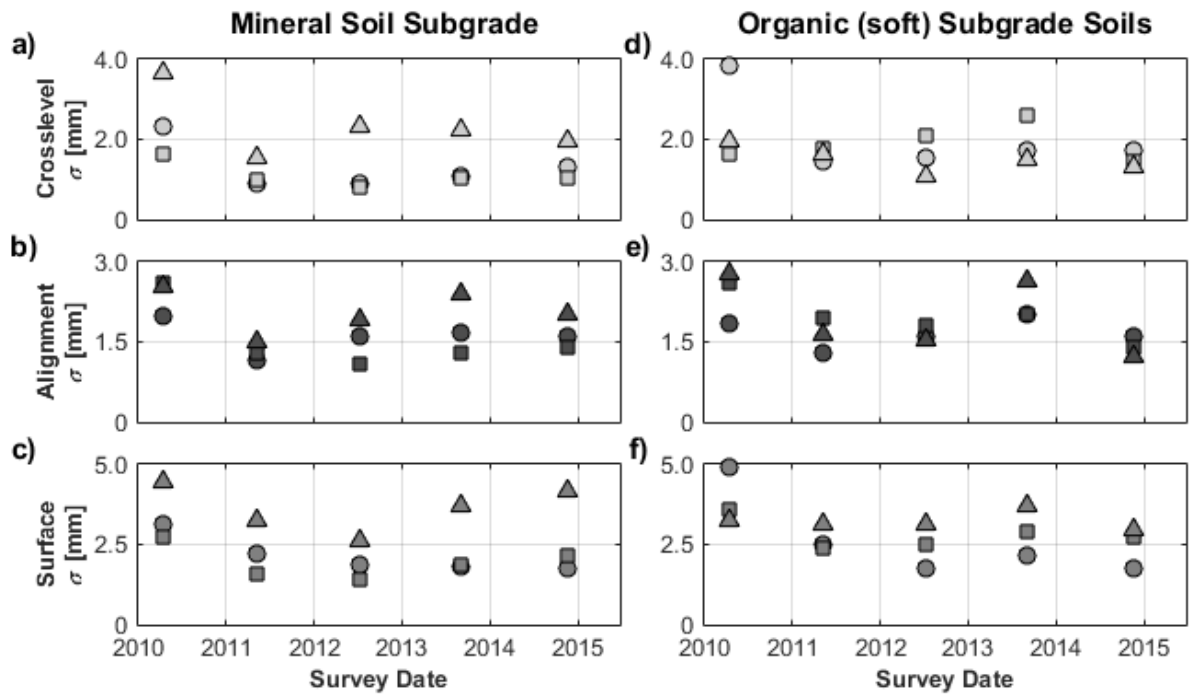

Figure 4-4. Trends in standard deviation (σ) calculated from the example track geometry data presented in Figure 2. Circles represent σ calculated for the segment between 0 and 60 m; squares for the segment between 60 and 120 m and triangles for the segment between 120 and 180 m.

4.6. Trends in Track Roughness

4.6.1. Expected Trends

Previous investigations of the impact of ballast maintenance on track settlement and track geometry roughness have focused on the effect and effectiveness of maintenance efforts to correct the geometry through tamping (Selig and Waters 1994, Sussmann et al. 2003, Andrews 2012, Audley and Andrews 2013, Andrews et al. 2014). This focus has led to the development of an idealized model for the behavior of track roughness that is illustrated in Figure 4-5 (Andrews 2012, Audley and Andrews 2013). Within this idealized model, the track roughness σ, increases

with time until a defined maximum limit is reached. Corrective maintenance is required to smooth the track geometry (commonly tamping) once this limit is reached. The maximum limit may be a regulated level of roughness or a tighter limit imposed by the operator to ensure the regulated level of roughness is never exceeded. After the corrective action, the accumulation of roughness begins again but at an accelerated rate. As a result, the time interval between tampings becomes shorter. The length of time between subsequent corrective maintenance interventions is approximately 1 to 2 years (Sussmann et al. 2003, Andrews 2012, Audley and Andrews 2013).

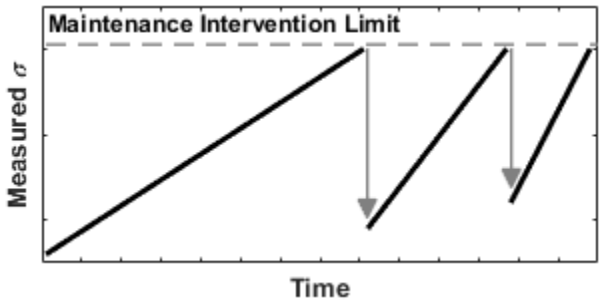

Figure 4-5. The idealized standard deviation (σ) behavior derived from measured track geometry showing the effect of repeated tamping after Audley and Andrews (2013).

The expected effect that ballast renewal will have on temporal trends in track geometry roughness is more central to this investigation. The idealized tamping model in Figure 4-5 illustrates that, while track geometry roughness may be reduced by tamping, the effect is short-lived. Andrews (2012) and Audley and Andrews (2013) attribute this phenomenon to tamping-induced ballast degradation. They conclude that tamping accelerates the rate at which the track roughness increases after each correction; therefore, many maintenance cycles were observed within a five-year period. For North American freight operations, continual rail traffic makes ballast renewal programs difficult to schedule and uneconomic. Under these conditions, repeated tamping is more advantageous as tamping can be performed between individual trains without an

associated traffic disruption. However, if the notion of tamping-induced ballast degradation accelerating the rate at which track roughness accumulates is correct, complete ballast renewal, through undercutting, would be expected to result in a rapid and *sustained* decrease in track roughness. As undercutting removes the bulk of the fines from the ballast void space, an extended period would be required for the fines to re-accumulate. Laboratory results by Huang et al. (2009), Indraratna et al. (2013), and Mishra et al. (2013) support this notion. Thus, the premise of subgrade conditions influencing roughness is evaluated by comparing whether ballast renewal was effective in producing sustained improvements in track geometry conditions in areas of mineral and organic subgrades.

4.6.2. Classification of Observed Trends

Once trends in σ were prepared, they were assigned one of four classifications that reflected the effectiveness of ballast undercutting at producing sustained reductions in σ at the end of a 3- to 4-year observation period after ballast renewal. The same classifications were applied to both mineral and organic subgrades and are described in Table 4-1. Figures 4-6 and 4-7 present examples of track geometry trends for each of the classifications as observed in one of the 115 segments. The σ amplitudes plotted in Figures 4-6 and 4-7 are normalized to the average σ of the geometry measure being evaluated as determined from all segments and all surveys.

Table 4-1. Description of the four track geometry trend classification types.

Roughness	Trend Description
Type I	A sustained three-to-four year reduction in σ (roughness) after ballast undercutting (example records are presented as Figure 4-6a).
Type II	A temporary reduction in σ after ballast undercutting but no long-term (three-to-four year) change (example records are presented as Figure 4-6b).
Type III	No notable reduction in σ after ballast undercutting and no long-term (three-to-four year) change (example records are presented as Figure 4-7a).
Type IV	An increase in σ three-to-four years after ballast undercutting (example records are presented as Figure 4-7b).

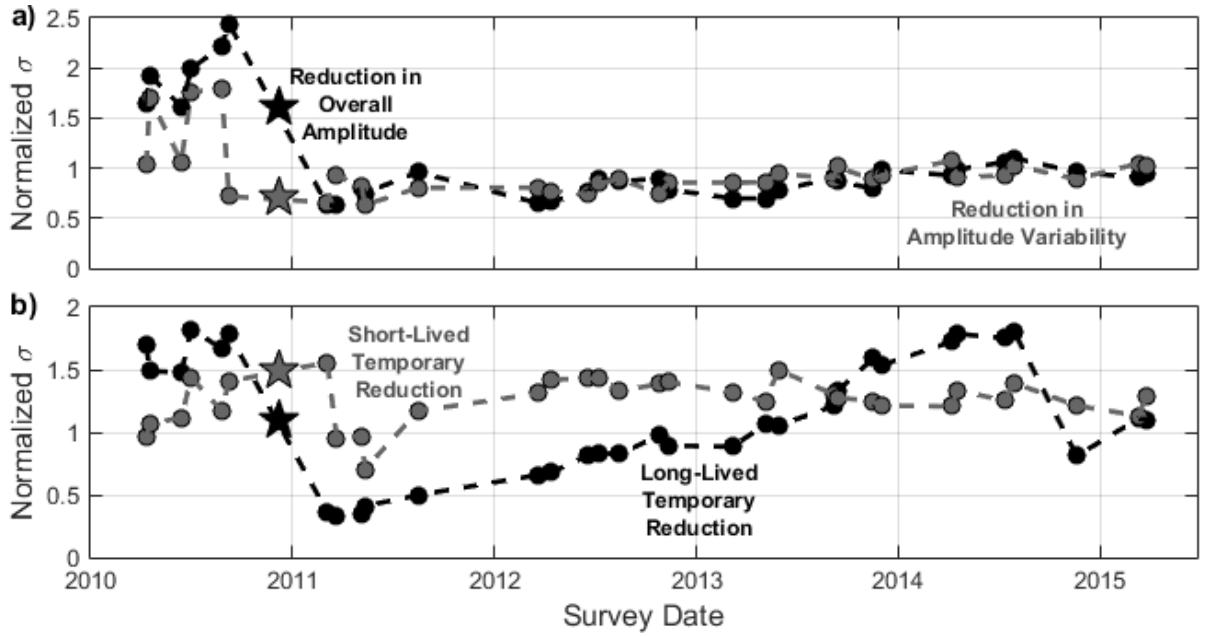

Figure 4-6. Trends in standard deviation (σ) showing a) a long-term reduction after ballast undercutting (Type I trends) and b) a temporary reduction after ballast undercutting but no long-term change (Type II trends). Stars indicate the interval between geometry surveys where the ballast renewal occurred.

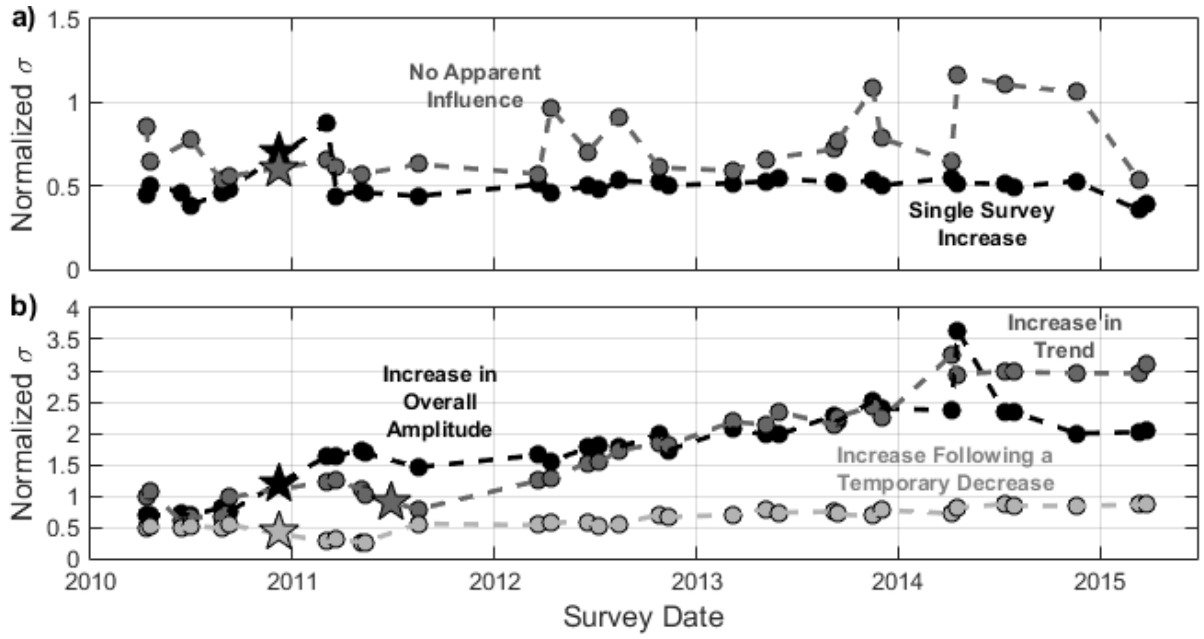

Figure 4-7. Trends in standard deviation (σ) showing a) no notable reductions after ballast undercutting and no long-term change (Type III trends) and b) a long-term increase after ballast undercutting (Type IV trends). Stars indicate the interval between geometry surveys where the ballast renewal occurred.

Figure 4-6a presents examples of alignment σ trends that show a sustained reduction after undercutting; they are classified as Type I. Reductions in track roughness appear as either an overall (step) decrease or a reduction in variability following ballast renewal. A Type I trend is interpreted as evidence that the rough track before ballast renewal was the result of degraded ballast. Figure 4-6b presents examples of crosslevel trends that show only a temporary reduction in σ after ballast renewal; these are classified as Type II. Both long- and short-lived reductions in roughness after undercutting were observed in the data. A Type II trend is interpreted as evidence that rough track at the site may have been influenced by degraded ballast conditions; however, by itself, ballast renewal did not result in a sustained decrease in roughness.

Figure 4-7a presents example crosslevel trends that show no reduction as well as no sustained change in track roughness after ballast renewal; these are classified as Type III. Type III roughness trends are either very flat with only slight variations near the time of ballast undercutting or highly variable but with no apparent relationship to ballast renewal. Type III trends are regarded as evidence that undercutting was not effective and that ballast conditions were not the underlying cause of track roughness at these locations.

Finally, Figure 4-7b presents example surface trends that show a sustained increase in σ after ballast renewal; these are classified as Type IV. Different forms of Type IV trends are evident, including overall (step) increases, gradually increasing roughness, and long-term increases after a temporary decrease. In all cases, the post-maintenance roughness exceeds that measured before maintenance for this Type. A Type IV trend is interpreted as evidence of the compacted structure of the ballast and subballast being disturbed to a loose state, thus leading to increasing roughness (Sussmann et al. 2012, Li et al. 2016).

4.7. Classification Results and Discussion

4.7.1. Spatial Distribution of Roughness Classifications

The effectiveness of the ballast undercutting at producing sustained reductions in track roughness was mapped using the Type I to Type IV classifications. Four examples of this mapped response are presented in Figures 4-8, 4-9, and 4-10. These four sections of track comprise most of the ballast renewal operations investigated as part of this study. Specifically, Figures 4-8, 4-9, and 4-10 present the classifications assigned to each undercut segment based on the σ trends developed for each geometric measure. The gaps within undercut sections three and four (Figure 4-10) reflect gaps between ballast maintenance operations in the records provided by the operator. An

aerial view of each undercut track section is also presented (sections one through four in Figures 4-8d, 4-9d, 4-10d, and 4-10h, respectively). Using these maps, it was possible to evaluate how ballast renewal affected track roughness in each segment as well as any spatial variation in the ballast quality-track roughness relationship.

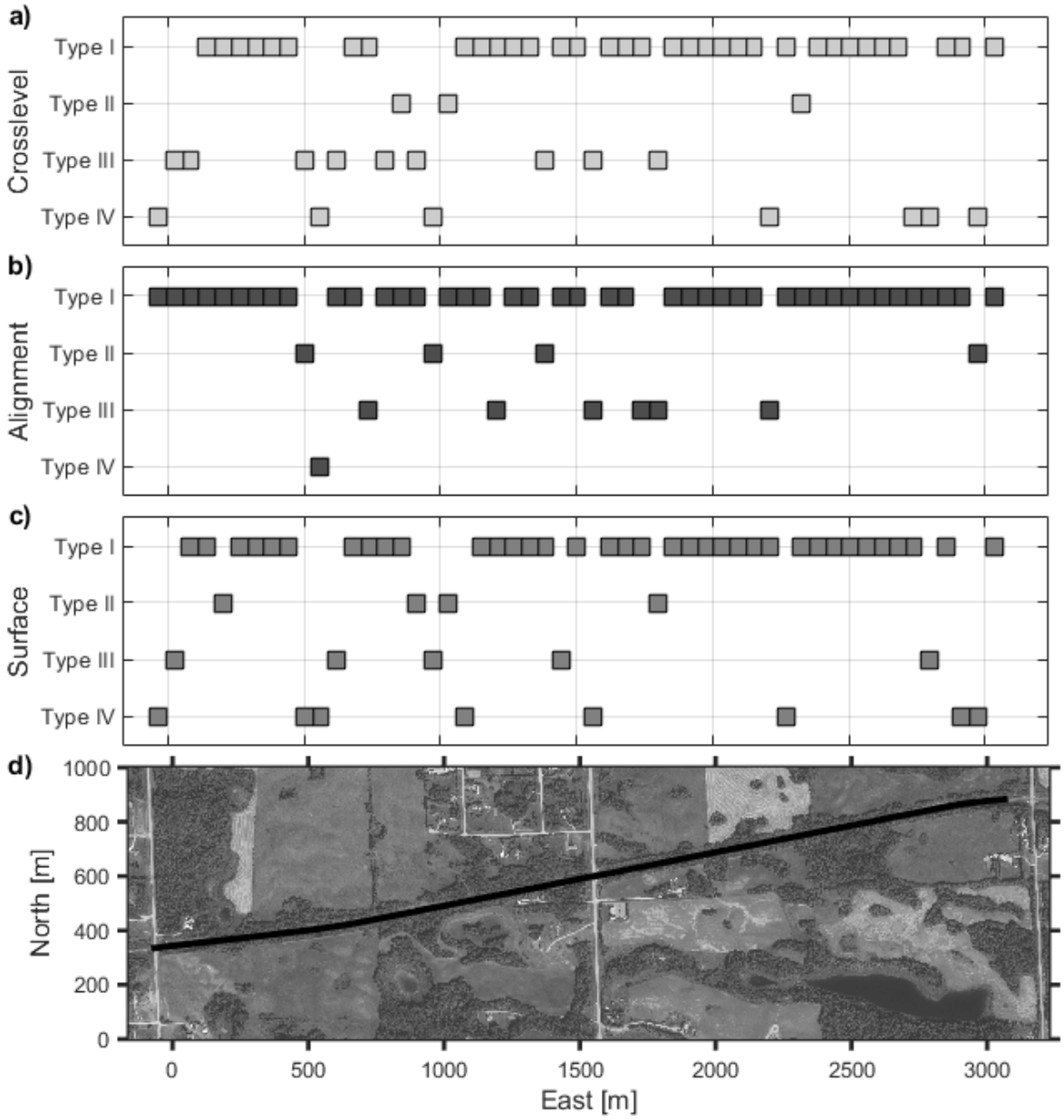

Figure 4-8. Along track variation in the classification results for a) track crosslevel, b) track alignment, and c) track surface in undercut section one illustrated in d).

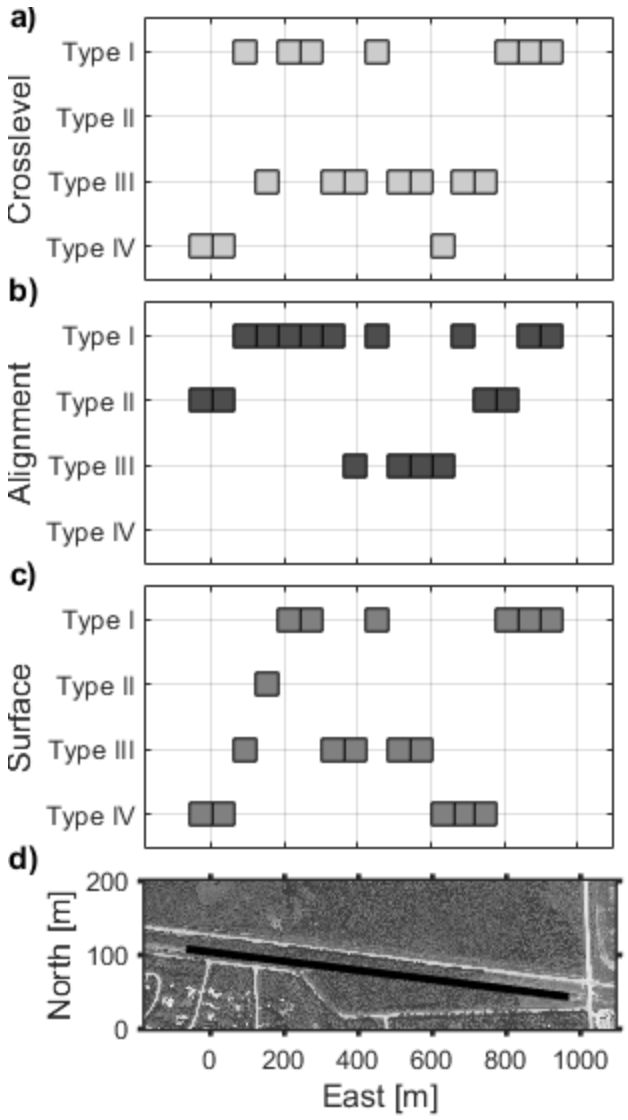

Figure 4-9. Along track variation in the classification results for a) track crosslevel, b) track alignment, and c) track surface in undercut section two illustrated in d).

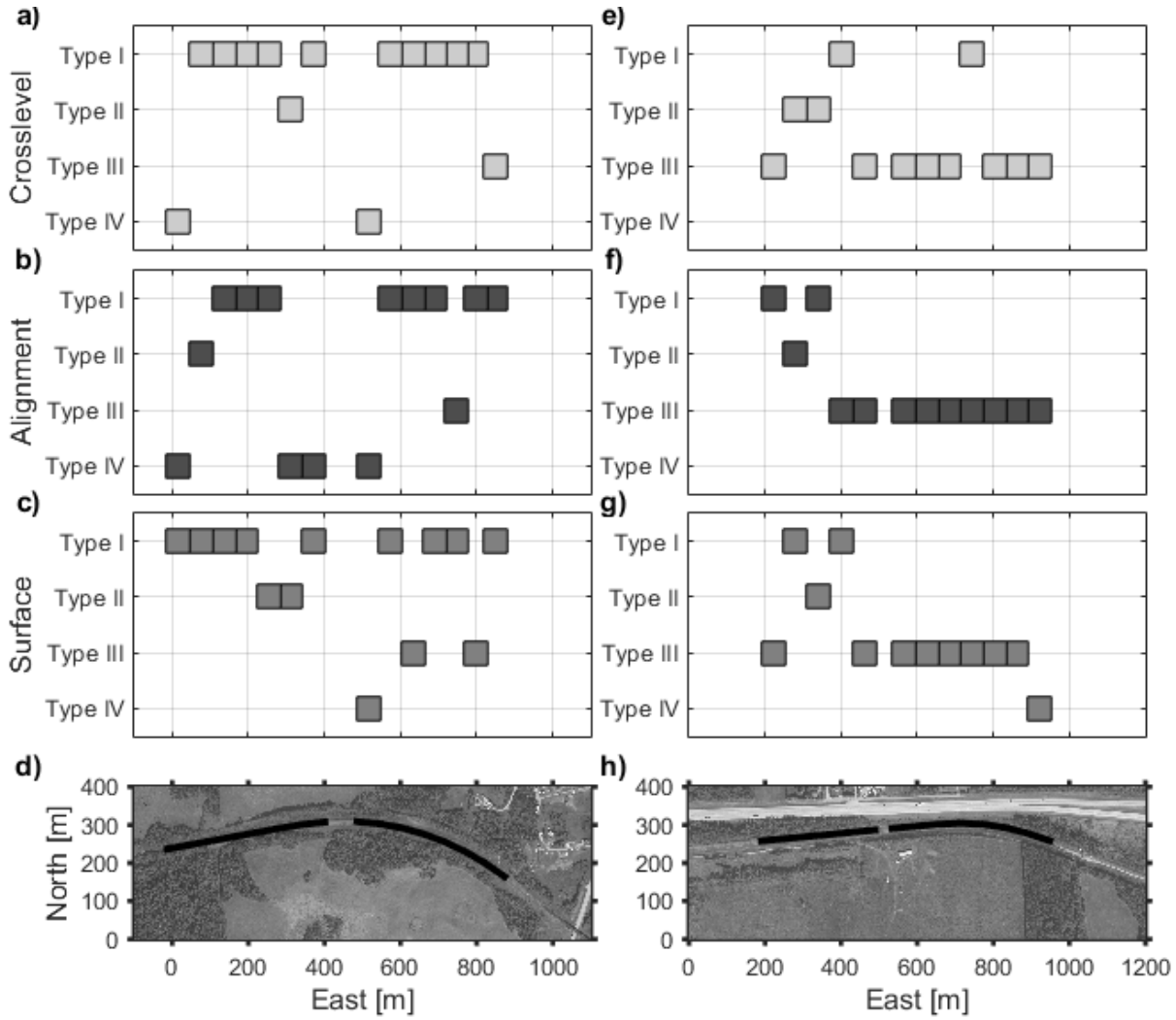

Figure 4-10. Along track variation in the classification results for track crosslevel [a), e)], track alignment [b), f)], and track surface [c), g)] for undercut section three illustrated in d) and four illustrated in h).

The mapped responses (Figures 4-8, 4-9, and 4-10) demonstrate that the relationship between ballast conditions and roughness is spatially variable. The value of σ is consistently reduced after improving ballast conditions for certain segments (Types I and II), while unaffected (Type III) or increased (Type IV) in others. This variation occurred at a local scale, i.e., within a single ballast renewal area, as well as at the large scale, i.e., between different renewal areas. The results

presented in Figure 4-8c show that the data for the majority (68%) of the segments reveal sustained decreases in surface roughness following ballast renewal (Type I classification). However, segments at 500 m East and 1000 m East exhibit a localized concentration of Type II, III, and IV trend classifications, where ballast renewal did not result in a sustained decrease in track roughness. Similar localized effects are present in the alignment classifications results (Figure 4-8a).

The trends presented for undercut track section one (Figure 4-8) can be contrasted with results for undercut section two (Figure 4-9) to highlight differences in the response between track areas. In Figure 4-9c, sustained improvements (Type I) were observed in only 35% of the segments. Type III and Type IV trends were much more prevalent in Figure 4-9c (29 and 29%, respectively) compared to Figure 4-8c (9 and 15%, respectively). Crosslevel trends presented in Figure 4-10a and Figure 4-10e also emphasize the large-scale differences between different sections of track. Roughness trends in 71% of the segments presented in Figure 4-10a, but only 17% of the segments presented in Figure 4-10e are classified as Type I.

The mapped responses also allow a direct comparison of the impacts of ballast renewal on the roughness trends observed in the three geometric measures (crosslevel, alignment, and surface). The results illustrate that the roughness types assigned to each geometric measure within a specific segment do not always agree with one another. Undercut section three, Figures 4-10(a-d), exhibits the least amount of agreement between the three geometric measures considered (36% of all segments), whereas agreements were observed in 51, 47, and 50% of the segments in sections one, two, and four, respectively (Figure 4-8, Figure 4-9, and Figures 4-10(e-h)). Thus, ballast renewal does not affect track roughness in the three geometric measures in the same manner. Crosslevel and surface roughness trends tend to agree with one another more so than

either does with alignment. Between 64 and 76% of crosslevel and surface segments classified similarly depending on the track section. This agreement between crosslevel and surface, more so than either with alignment, is likely a result of both measures being generated from vertical measurements to the top of the rails.

4.7.2. Effect of Subgrade on Track Roughness

To evaluate the impact of subgrade on track roughness, the 112 segments for which subgrade conditions could be determined were differentiated by the dominant subgrade type and the relative proportion of each type classification was evaluated. Figure 4-11a presents the classification results for segments overlying mineral (sand, silt, clay and glacial till) soils, while Figure 4-11b presents the classification results for those constructed on organic (peat) soils.

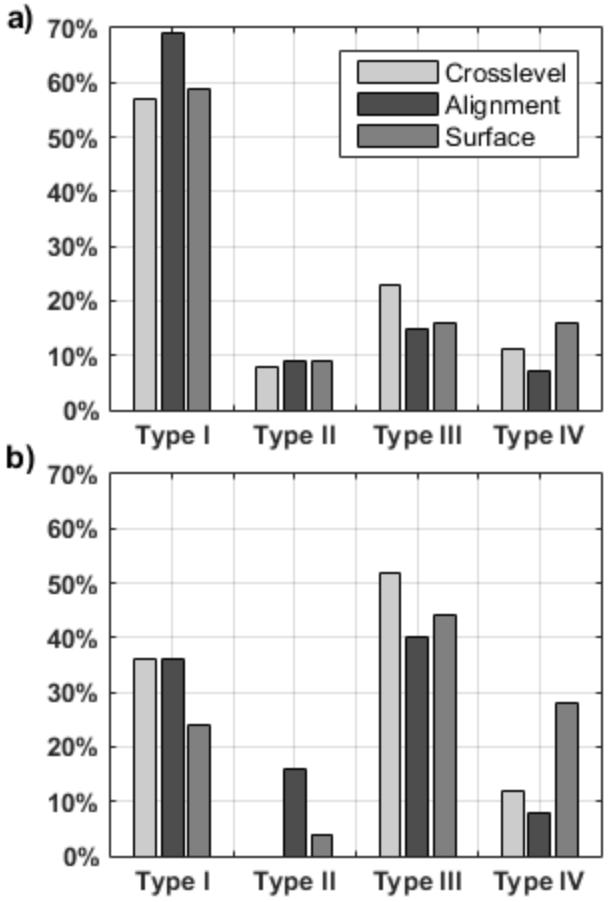

Figure 4-11. Percentage of undercut segments belonging to each classification type for track constructed on subgrades where the dominant materials were a) mineral (till, sand, silt, and clay) and b) organic (peat). The total number of undercut segments represented in a) and b) are 87 and 25, respectively.

The proportion of segments constructed on mineral subgrades (Figure 4-11a) that demonstrate the tendency for a sustained reduction in roughness after ballast renewal (Type I) is significantly greater than for those constructed on organic subgrades (Figure 4-11b) by upwards of 33%. In addition, Type III segments are much more prevalent in areas of organic subgrades compared to mineral subgrades (by upwards of 30%). A careful inspection of the surface classification results presented in Figure 4-11b also highlights that a slightly greater number of segments exhibit a

long-term increase in surface σ after ballast renewal (Type IV) than a long-term decrease (Type I). These results imply that degradation of the ballast is a common misdiagnosis for the root cause of roughness over very soft organic terrain; indeed, improvements made to ballast degradation conditions do not often translate into reduced long-term track roughness.

Several segments continue to exhibit behavior in contrast to the general tendencies based on subgrade type. Track constructed on mineral subgrades (Figure 4-11a) featured segments with track roughness trends classified as either Type III or Type IV, while track constructed on organic subgrades (Figure 4-11b) featured Type I segments. This may be related to isolated pockets of other soil types underlying individual undercut segments.

4.8. Conclusions

Two seasons (2010 and 2011) of ballast undercutting records and five years (April 2010 through March 2015) of track geometry data were used to evaluate the impact of undercutting on geometry roughness trends across 6.90 km of railway track in Alberta Canada. The post ballast renewal track quality was evaluated based on trends in track roughness. The track roughness was quantified using a standard deviation of track geometry calculated over 60 m long segment. The results of this analysis show that 60% of the track (4.14 km) exhibited a sustained decrease in roughness after ballast renewal supporting the notion that degraded ballast is a primary cause of increased track geometry roughness. However, the remaining 40% (2.76 km) of track suggest that other factors, beyond ballast conditions, are also influencing track roughness at a significant scale.

Contrasting the relationship between degraded ballast and track roughness by subgrade type quantified the influence of soft subgrades on trends observed in the track geometry data. The results of this analysis show that 69% (3.60 km) of the ballast renewal results in reduced track

roughness when constructed on stiffer mineral subgrade soils (sand, silt, clay and glacial till). This further supported the notion that the management of ballast degradation is an effective control against the development of track roughness. A total of 5.22 km of the undercut track was constructed on mineral subgrade soils. In contrast, track roughness on softer, organic (peat) subgrades (a total of 1.50 km) is not as strongly influenced by undercutting and ballast renewal, with only 36% of the track (0.54 km) showing improvement. This implies that undercutting of degraded ballast may not be sufficient to correct track geometry roughness for track constructed over soft organic subgrades.

4.9. Acknowledgements

The authors thank both Canadian National Railway and Canadian Pacific Railway for their support and facilitation of this project. Specifically, we thank Tom Edwards and Eddie Choi for facilitating the collection of these data sets. This research was made possible through the Canadian Rail Research Laboratory (CaRRL) (www.carrl.ca), which is funded by the Natural Sciences and Engineering Research Council of Canada, Canadian Pacific Railway, Canadian National Railway, the Association of American Railways – Transportation Technology Centre Inc., the National Research Council of Canada, Transport Canada, and Alberta Innovates – Technology Futures.

4.10. References

Alberta Agriculture and Forestry. 2012. Alberta soil information viewer [online]. Available from http://www4.agric.gov.ab.ca/agrasidviewer/ [cited 03/16 2016].

Andrews, J. 2012. A modelling approach to railway track asset management, Proceedings of the Institution of Mechanical Engineers, Part F: Journal of Rail and Rapid Transit, **227**(1): 56-73.

Andrews, J., Prescott, D., and De Rozières, F. 2014. A stochastic model for railway track asset management, Reliability Engineering and System Safety, **130**: 76-84.

Askarinejad, H., Dhanasekar, M., and Simson, S. 2010. Effect of vertical misalignment of adjacent sleepers on the increase in dynamic loads around rail joints. In Conference on Railway Engineering, Wellington, NZ, pp. 169-179.

Audley, M. and Andrews, J.D. 2013. The effects of tamping on railway track geometry degradation, Proceedings of the Institution of Mechanical Engineers, Part F: Journal of Rail and Rapid Transit, **227**(4): 376-391.

Berawi, A.R.B., Delgado, R., Calçada, R., and Vale, C. 2010. Evaluating track geometrical quality through different methodologies, International Journal of Technology, **1**: 38-47.

De Bold, R., O'Connor, G., Morrissey, J.P., and Forde, M.C. 2015. Benchmarking large scale GPR experiments on railway ballast, Construction and Building Materials, **92**: 31-42.

Ebersöhn, W. and Selig, E.T. 1994. Use of track geometry measurements for maintenance planning, Transportation Research Record, **1470**.

Federal Railroad Administration. 2014. Track and rail and infrastructure integrity compliance manual. Federal Railroad Administration, Washington DC, USA.

Huang, H., Tutumluer, E., and Dombrow, W. 2009. Laboratory characterization of fouled railroad ballast behavior, Transportation Research Record, **2117**: 93-101.

Indraratna, B., Tennakoon, N., Nimbalkar, S., and Rujikiatkamjorn, C. 2013. Behaviour of clay-fouled ballast under drained triaxial testing, Géotechnique, **63**(5): 410-419.

Li, D., Hyslip, J.P., Sussmann, T.R., and Chrismer, S.M. 2016. Railway geotechnics. Taylor & Francis Group LLC, Boca Raton, FL, USA.

Mishra, D., Kazmee, H., Tutumluer, E., Pforr, J., Read, D., and Gehringer, E.:. 2013. Characterization of railroad ballast behavior under repeated loading: Results from new large triaxial setup, Transportation Research Record, **2374**: 169-179.

Prescott, D. and Andrews, J. 2013. A track ballast maintenance and inspection model for a rail network, Proceedings of the Institution of Mechanical Engineers, Part O: Journal of Risk and Reliability, **227**(3): 251-266.

Rail Safety and Standard Board Limited. 2011. Track system requirements. United Kingdom, London.

Roghani, A. and Hendry, M.T. 2016. Continuous vertical track deflection measurements to map subgrade condition along a railway line: Methodology and case studies, Journal of Transportation Engineering, **142**(12): 04016059-1-04016059-8.

Sadeghi, J. 2010. Development of railway track geometry indexes based on statistical distribution of geometry data, Journal of Transportation Engineering, **136**(8): 693-700.

Sadeghi, J. and Askarinejad, H. 2011. Development of track condition assessment model based on visual inspection, Structure and Infrastructure Engineering: Maintenance, Management, Life-Cycle Design and Performance, **7**: 895-905.

Sadeghi, J. and Askarinejad, H. 2010. Development of improved railway track degradation models, Structure and Infrastructure Engineering: Maintenance, Management, Life-Cycle Design and Performance, **6**: 675-688.

Sadeghi, J. and Askarinejad, H. 2009. An investigation into the effects of track structural conditions on railway track geometry deviations, Proceedings of the Institution of Mechanical Engineers, Part F: Journal of Rail and Rapid Transit, **233**: 415-425.

Scanlan, K.M., Hendry, M.T., and Martin, C.D. 2016. Evaluating the equivalency between track quality indices and minimum track geometry threshold exceedances along a Canadian freight railway. Proceedings of the 2016 ASME Joint Rail Conference, April 12-15, Columbia SC, USA. DOI: 10.1115/JRC2016-5748.

Selig, E.T. and Waters, J.M. 1994. Track geotechnology and substructure management. Thomas Telford Ltd., London.

Sussmann, T.R., Ruel, M., and Chrismer, S.M. 2012. Source of ballast fouling and influence considerations for condition assessment criteria, Transportation Research Record, **2289**: 87-94.

Sussmann, T.R., Selig, E.T., and Hyslip, J.P. 2003. Railway track condition indicators from ground penetrating radar, NDT&E International, **36**(3): 157-167.

Transport Canada. 2012. Rules respecting track safety. Canada, Ottawa.

Zong, N., Askarinejad, H., Heva, T.B., and Dhanasekar, M. 2013. Service condition of railroad corridors around the insulated rail joints, Journal of Transportation Engineering, **139**(6): 643-650.

Chapter 5: Evaluating the sensitivity of low-frequency ground-penetrating radar attributes to estimate ballast fines in the presence of variable track foundations through simulation

5.1. Contribution of the Ph.D. Candidate

All of the work presented in this chapter was performed by the Ph.D. candidate, including literature review, data modelling, processing, analysis, and interpretation as well as manuscript preparation. This chapter details the use of synthetic ground-penetrating radar measurements of a modelled two-layer ballasted track foundation to evaluate the sensitivity of various ground-penetrating radar attributes as conditions within the track foundation are progressively altered. Specifically, how changes in ballast thickness, saturation, conductivity, and subballast material type influence the ability to use the attribute values as a reliable estimate for the amount of fines within the ballast. As supervisors, Dr. M.T. Hendry, Dr. C.D. Martin, and Dr. D.R. Schmitt reviewed all parts of the work. This chapter has been published with the following citation;

Scanlan, K.M., Hendry, M.T., Martin, C.D., and Schmitt, D.R. 2017. Evaluating the sensitivity of low-frequency ground-penetrating radar attributes to estimate ballast fines in presence of variable track foundations through simulation. Proceedings of the Institution of Mechanical Engineers Part F: Journal of Rail and Rapid Transit, in press, online: DOI: 10.1177/0954409717710408.

5.2. Abstract

The sensitivity of three low-frequency (<1 GHz) ground-penetrating radar (GPR) attributes commonly used to infer the amount of fines present within railway ballast was evaluated using

synthetic datasets. Variations in ballast thickness, saturation, and subballast material type are not often considered during laboratory or small-scale (few kilometers of track) field studies. If GPR were to be applied as a ballast degradation detection tool on a subdivision (hundreds of kilometers) scale, it is critical to assess the impact variations in these track foundation conditions will have on the inferred amount of fines present within the ballast.

In this analysis, a two-layer (ballast and subballast) track foundation model was incorporated into in a series of GPR simulations where the physical dimensions and electromagnetic properties of the model were systematically varied. It was through the electromagnetic properties that the volumetric amount of fines and moisture present within the ballast and the type of subballast material were altered. The GPR response of each model was simulated using a finite-difference time-domain solver for Maxwell's equations (gprMax). The amount of fines present in the ballast was then inferred through attributes calculated from the synthetic GPR measurements and related to the known model input. This comparison revealed that ambiguities in the GPR attribute amplitudes were common. Specific GPR attribute amplitudes could not be uniquely associated with the known amounts of fines present within the ballast as the other conditions in the track foundation (ballast saturation, ballast thickness, and subballast material) were varied. As such, a quantitative and reliable estimation for the amount of fines present within ballast using GPR measurements over large scales would be difficult without first constraining the variability in the track foundation.

5.3. Introduction

Ballast is a fundamental component of a track foundation providing (amongst other functions) structural support to the ties and water-shedding pathways (Selig and Waters 1994). With time, ballast degrades as fine-grained particles (fines) accumulate within the void space between the

ballast aggregate (Sussmann et al. 2012). Degradation limits the ability of the ballast to perform its intended functions, which leads to track geometry issues and increased maintenance costs (Huang et al. 2009, Audley and Andrews 2013, Indraratna et al. 2013, Mishra et al. 2013). Consequently, both economic and safety concerns mandate that the quality of the ballast be periodically assessed and that developing methodologies to accomplish this both inexpensively and reliably is necessary.

Ground-penetrating radar (GPR) is one such geophysical tool that is often applied during railway foundation investigations (Gallagher et al. 1999, Hugenschmidt 2000, Sussmann et al. 2003, Anbazhagan et al. 2011). GPR is non-destructive and capable of yielding spatially extensive, high-resolution information on track foundations in a short period of time. Figure 5-1 illustrates how low-frequency (<1 GHz) GPR waves propagate and reflect within a typical ballasted track foundation. Reflections generated at interfaces between contrasting electromagnetic (EM) properties are recorded by the receiving antenna to produce a single GPR trace.

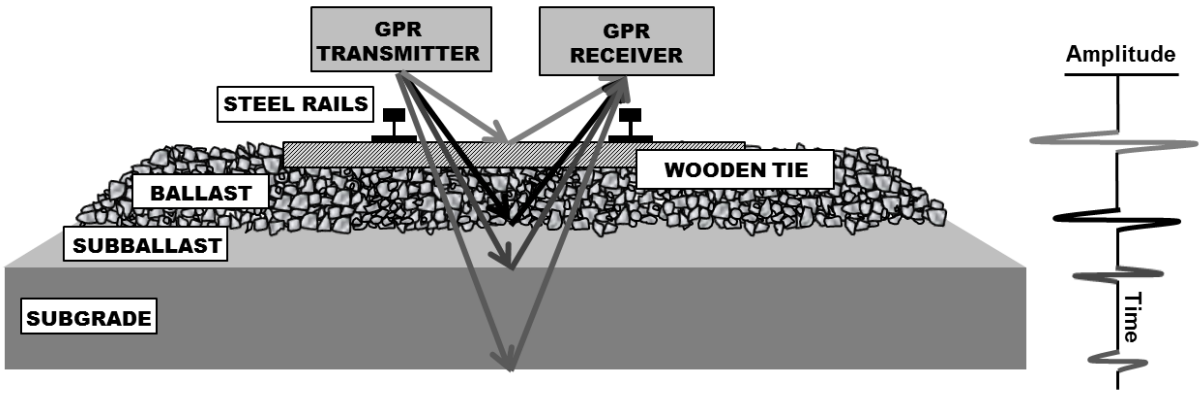

Figure 5-1. Typical ballasted track foundation structure and important ground-penetrating radar reflections (top-of-ballast, base-of-ballast, base of subballast and subgrade reflections).

Railway GPR datasets are often analyzed to qualitatively or semi-quantitatively estimate the degradation and moisture conditions within the ballast with the goal of aiding in targeted track

foundation maintenance (Roberts et al. 2006, Al-Qadi et al. 2008, Plati et al. 2010, Silvast et al. 2010, Khakiev et al. 2014b). This is possible as the accumulation of fine-grained particles and moisture alter the material properties influencing GPR wave propagation and scattering in a detectable manner (Clark et al. 2001, Roberts et al. 2006, De Chiara et al. 2014, Parsons et al. 2014). This interpretation of GPR datasets is similar to the analysis of attributes commonly performed on seismic reflection datasets (Chopra and Marfurt 2005). Specifically for GPR, the accumulation of fines within the ballast alters the speed at which GPR waves traverse the ballast, the amount of signal attenuation that occurs in the ballast, and the strength of the reflection from the ballast-subballast interface. Quantification of these attributes has been shown to be representative of ballast degradation conditions in both laboratory studies as well as local (a few kilometers of track) field investigations (Silvast et al. 2010, Su et al. 2010, Khakiev et al. 2014a, Khakiev et al. 2014b, Kashani et al. 2016). In addition, the presence of fines also alters GPR wave scattering in the ballast at high (>1 GHz) signal frequencies (Roberts et al. 2006, Al-Qadi et al. 2008). At high signal frequencies, the GPR wavelength approaches the diameter of the individual voids within the ballast, resulting in a transition from Rayleigh-type behavior to Mie scattering.

During laboratory and local-scale GPR studies conducted at low (<1 GHz) signal frequencies, the impact of variations in ballast thickness, saturation and subballast material type have not often been assessed. However, if GPR were to be applied as a ballast degradation identification tool on a subdivision (hundreds of kilometers) scale, variations in these track foundation conditions would ultimately arise. Therefore, it is critical to assess whether these variations impact the ability to quantitatively infer ballast degradation levels from GPR signals. As such, this paper reviews the sensitivity of three GPR-based ballast degradation estimation attributes to

changes in ballast thickness, saturation, and the type of subballast material using synthetic 400MHz GPR datasets.

This analysis begins with a basic outline of the electromagnetic (EM) material properties critical in GPR and how they have been observed to vary in response to ballast degradation. This is then followed by an overview of the various low-frequency GPR attributes used to infer changes in the EM properties associated with ballast degradation. Next are descriptions of the synthetic model, how the EM properties of the modeled materials are varied to reflect the different conditions in the track foundation, and a discussion of the preliminary processing applied to the synthetic GPR dataset prior to calculating the various attributes. Finally, the various attributes are calculated from the synthetic data and used to evaluate the sensitivity of the model as well as the impact of a variable track foundation on their relationship with the volumetric amount of fines within the ballast.

5.4. Effect of Ballast Degradation on Electromagnetic Material Properties

The accumulation of fines within ballast void space alters the bulk EM material parameters of the ballast layer and forms the premise for using GPR in ballast degradation studies (Clark et al. 2001, De Chiara et al. 2014, Parsons et al. 2014). At low antenna frequencies (<1 GHz), GPR behaviour in non-magnetic granular materials is dominantly controlled the dielectric permittivity (ε; measured in Farads per meter, F/m) and electrical conductivity (σ; measured in millisiemens per meter, mS/m) (Jol 2009). In reality, both ε and σ are complex valued; although for the purposes of this analysis and to limit overall complexity, their imaginary components will not be considered. For a more thorough discussion of the complex nature of EM material properties, the interested reader is directed to Jol (2009) and Bano (2004).

The dielectric permittivity of earth materials are commonly represented as *relative* dielectric permittivities (ε_r), which are the ratio of the true dielectric permittivity of a material (ε) and the dielectric permittivity of free space (ε_0; 8.8542 x 10^{-12} F/m)

$$\varepsilon_r = \frac{\varepsilon}{\varepsilon_0}. \qquad \text{[Equation 5-1]}$$

The impact of ballast degradation on the bulk ε_r of ballast was first quantitatively studied by Clark et al. (2001). These authors observed that the bulk ε_r of a ballast increases with ballast degradation and moisture content; ranging between 3.0 for a dry clean ballast to 38.5 for a water-saturated spent ballast. The impact of increasing moisture contents is greater than that from increasing degradation due to the large ε_r of water (81). Similar trends of ε_r increasing with ballast degradation and moisture content are also observed by De Chiara et al. (2014) and Kashani et al. (2016).

Parsons et al. (2014) investigated the effect of ballast degradation on effective ballast electrical resistivity (ρ; measured on Ohm-meters, Ωm). Electrical resistivity quantifies the ability of a material to resist the flow of an electric current and is the reciprocal of the electric conductivity (σ)

$$\sigma = \frac{1}{\rho}. \qquad \text{[Equation 5-2]}$$

Parsons et al. (2014) originally quantified ballast ρ as opposed to σ due to the electrical resistivity equipment used. Their tests demonstrated that, similar to ε_r, ballast σ increased with degradation and moisture content. Under dry conditions, they report a bulk σ of 1.67 mS/m (corresponding to an approximate resistivity of 600 Ωm) for the least degraded ballast and 10 mS/m (100 Ωm) for the most degraded ballast tested. Both Clark et al. (2001) and Parsons et al. (2014) conducted their respective testing using granitic ballasts and crushed ballast aggregate as the fines material but the specific quantities of fines associated with each test were not reported.

5.5. Estimating Ballast Degradation Levels from GPR Data

Estimating ballast degradation levels from low-frequency GPR measurements involves either estimating the altered EM material properties directly or quantifying their subsequent effect on the recorded GPR signals (Clark et al. 2001, Silvast et al. 2006, Silvast et al. 2010, De Chiara et al. 2014, Khakiev et al. 2014b). The first interpretation attribute investigated as part of this study is the direct calculation the bulk ballast ε_r based on GPR propagation velocity, while the second and third attributes attempt to indirectly represent variations in ε_r (related to variations in the amount of fines present within the ballast) through GPR signal attenuation and reflectivity, respectively.

5.5.1. Propagation Velocity

The GPR propagation velocity within the ballast can be used to directly estimate ε_r, which subsequently reflects ballast degradation conditions (Clark et al. 2001, De Chiara et al. 2014). The velocity of a propagating GPR wave (v) is defined as the ratio between the speed of light (c) (2.9979×10^8 m/s) and the square-root of the ballast ε_r:

$$v = \frac{c}{\sqrt{\varepsilon_r}}. \qquad \text{[Equation 5-3]}$$

GPR wave velocities can be estimated from the time interval between the air-ballast and ballast-subballast interface reflections, determined from individual GPR traces (Figure 5-1), and the ballast thickness. GPR data are commonly presented in terms of two-way times. A two-way time is the time required for a GPR wave to travel from the transmitting antenna to an interface between two materials with contrasting ε_r (at which point a reflected wave is generated) and for the reflected wave to propagate and be recorded by the receiving antenna. Assuming a negligible time shift resulting from the lateral offset between a transmitting and a receiving antenna, the

GPR wave travel-time within the ballast is equal to half the two-way time between the air-ballast reflection and ballast-subballast reflection. When determining the two-way time between the air-ballast and ballast-subballast reflections, the same position on both reflections must be selected. Erroneous shortening or lengthening of the two-way time will result in the true GPR wave velocity being either overestimated or underestimated. Once both the ballast thickness and the proper time interval between the bounding reflections are known, the ε_r of the ballast can be estimated.

While in principle estimating the propagation velocity within the ballast is straightforward, it can be difficult to determine from single GPR traces acquired along operational railways. Interference from reflections off of the surrounding railway infrastructure (rails, ties, and signaling) can obscure the air-ballast and ballast-subballast reflections (Olhoeft 2005). The ballast thickness is also often variable along a given track section (Roghani and Hendry 2016). and difficult to determine without destructive investigations (boreholes or trenching). As this study incorporates simulated GPR measurements, undesirable GPR signals can be minimized or removed prior to velocity determination and the ballast thickness is known. Specialized GPR survey designs, such as common midpoint (CMP) surveys or wide angle reflection-refraction (WARR) surveys, can be used to estimate propagation velocities directly (Jol 2009) but have not been commonly applied to ballast degradation studies.

5.5.2. Windowed Fourier Amplitude Spectrum Integral

The first indirect GPR attribute used to quantify degradation in the ballast, initially proposed by Silvast et al. (2006) and Silvast et al. (2010), exploits the effect of ballast degradation on intrinsic GPR signal attenuation. GPR signals attenuate exponentially at a rate quantified by α (Liu et al. 1998, Irving and Knight 2003) :

$$\alpha = \omega[\frac{\mu\varepsilon}{2}\left(\sqrt{1 + tan^2\delta} - 1\right)]^{1/2} \ .$$ [Equation 5-4]

While the loss tangent ($tan\delta = \sigma/\omega\varepsilon$) is considered to be relatively small due to the frequency range (MHz to GHz) at which GPR surveys operate (Liu et al. 1998), it still exerts an effect. For non-magnetic earth materials, the relative magnetic permeability (μ_r) is equal to unity and the magnetic permeability of the material is equal to that of free space ($\mu = \mu_o = 4\pi \times 10^{-7}$ Henries per meter, H/m) and the magnetic properties of the material can be ignored. α is then solely dependent on the material ε and σ as well as the angular frequency ($\omega=2\pi f$). GPR signal attenuation is greatest at higher frequencies and in a material with a larger ε_r and σ.

Silvast et al. (2006) and Silvast et al. (2010) demonstrate that the presence of degraded ballast (ballast with a greater ε_r) increases the attenuation of the high frequency components of a propagating GPR signal. Due to the increased signal attenuation, the integral of the normalized Fourier amplitude spectrum across all frequencies is smaller for degraded ballast compared to non-degraded (clean) ballast (Figure 5-2). The authors were able to isolate the signal attenuation within the ballast by windowing individual traces prior to conducting the Fourier transformation, and including only the portions related to wave propagation in the ballast. The resulting normalized amplitude spectrum integrals quantitatively correlated with the level of degradation present in the ballast. This approach to evaluating GPR data is referred to throughout the remainder of this analysis as the windowed Fourier amplitude spectrum integral (WFASI) attribute.

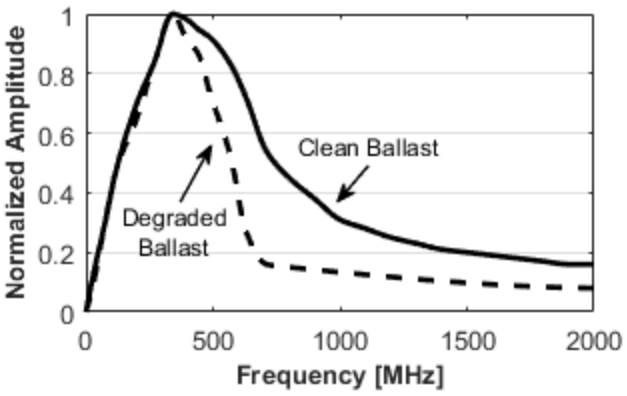

Figure 5-2. Normalized Fourier amplitude spectra of two ground-penetrating radar traces, one recorded over clean ballast (solid line) and one over degraded ballast (dashed line), based on Silvast et al. (2010). Note the reduced integral area under the degraded ballast spectrum compared to the clean ballast spectrum.

5.5.3. Normalized Reflectivity

The second indirect attribute, developed by Khakiev et al. (2014b) and Khakiev et al. (2014a) is intended to monitor relative moisture changes within ballast. Similar to the accumulation of fines, increasing ballast moisture contents result in increases in the bulk ε_r and σ of the ballast (Clark et al. 2001, De Chiara et al. 2014, Kashani et al. 2016), and the methodology applied in Khakiev et al. (2014b) is transferrable to a relative study of ballast degradation. Increased moisture retention in the ballast is also considered to be a secondary effect of fines accumulating within the ballast (Selig and Waters 1994, Sussmann et al. 2012).

Khakiev et al. (2014b) demonstrate that changes in moisture content alter the strength of the reflection from the ballast-subballast interface. The amplitude of a propagating GPR wave is described by the strength of its associated electric field. Such a wave is reflected when it impinges of an interface between two materials with contrasting ε_r. The strength of the reflection

coefficient depends on the contrast between the ε_r and is quantified by the reflection coefficient *R*, which is the ratio of the reflected and incident amplitudes. The normal incidence reflection coefficient for a transverse-electric (TE) polarized mode wave from the interface between the ballast (ε_{r1}) and the subballast (ε_{r2}) is (Jol 2009):

$$R = \frac{\sqrt{\varepsilon_{r1}}-\sqrt{\varepsilon_{r2}}}{\sqrt{\varepsilon_{r1}}+\sqrt{\varepsilon_{r2}}}. \qquad \text{[Equation 5-5]}$$

While, in reality, perfect normal wave incidence on the ballast-subballast interface does not occur due to small lateral offsets between the transmitting and receiving GPR antennae, the main aspects of reflection behaviour can be understood by considering as if this were the case.

As the ballast moisture content increases (increasing ε_{r1}), Khakiev et al. (2014b) observe that the proportion of amplitude reflected from the ballast-subballast interface relative to the total scan amplitude also increases. By comparing GPR measurements of the same ballast performed at different times under different moisture conditions, the relative change in moisture content could be assessed, provided that the subballast remains unchanged. A similar principle may be applied to the relative estimation of ballast degradation levels. As degradation progressively accumulates within the void space (increasing ε_{r1}) the normalized reflectivity from the ballast-subballast interface would also increase.

5.6. The Synthetic Track Foundation Model

In this analysis, the impact of varying track foundation conditions on the attributes used to detect ballast degradation from GPR signals is evaluated using a simulated track foundation model and synthetic GPR signals. Constructing a representative full-scale laboratory model to test the various track foundation configurations was considered to be too time consuming and laborious. An efficient alternative is a simulated track foundation model comprised of homogeneous layers

whose physical size and EM properties were easily altered when considering various track foundation conditions. Synthetic GPR signals generated from the simulated track foundation model are also noise-free. Any sensitivity in the GPR attributes reflect changes made to the foundation model and is not noise related.

The GPR measurements are simulated using a three-dimensional track foundation model constructed in the finite-difference time-domain (FDTD) GPR modeling gprMax software (Warren et al. 2016). Benedetto et al. (2016) demonstrate that synthetic GPR signals produced with gprMax agree well with laboratory GPR measurements of ballasts containing variable amounts of fines. The simulated model is restricted to a three-layer combination of air, ballast, and subballast and the influence of ties is not considered.

The physical dimensions and EM properties (ε_r and σ) of the individual layers as well as the GPR signal inputs are communicated to gprMax through a command file. The model is subdivided into individual $0.005 \times 0.005 \times 0.005$ m cells to facilitate the FDTD approach to solving the EM wave equations governing GPR wave propagation and reflections (Warren et al. 2016). This cell size was chosen to ensure that the gprMax criterion of cell size being less than one-tenth the dominant GPR wavelength is satisfied (Warren et al. 2016). Ten-cell thick absorbing boundary conditions are placed around the outer edges of the model domain to suppress undesirable reflections from the model boundaries. Variations in lateral model dimensions between 0.50 m and 4.00 m and subballast thicknesses between 0.30 m and 0.70 m are used to evaluate any model size-dependency in the GPR attributes. Ballast thicknesses varying between 0.30 m and 0.60 m are incorporated into the analysis of GPR attribute sensitivities.

A 400 MHz Ricker wavelet is used to represent the GPR signal. The GPR wave is stimulated by a Hertzian dipole positioned 0.25 m above the ballast surface. A receiving antenna, also

positioned 0.25 m above the ballast surface, records the direct wave travelling directly from the transmitter as well as all backscattered energy from material contrasts. The transmitting and receiving antennae are laterally offset 0.10 m with the midpoint between antennas located in the middle of the model domain.

An example synthetic model is shown in Figure 5-3. In this version of the model, the dimensions of the model in the X and Y direction are both 1.00 m and the thickness of the ballast and subballast are 0.40 m and 0.30 m, respectively. In all models, a fractal surface roughness is added to the top surface of the ballast to provide a more realistic surface topography as may be encountered along an operational railway (Giannakis et al. 2016).

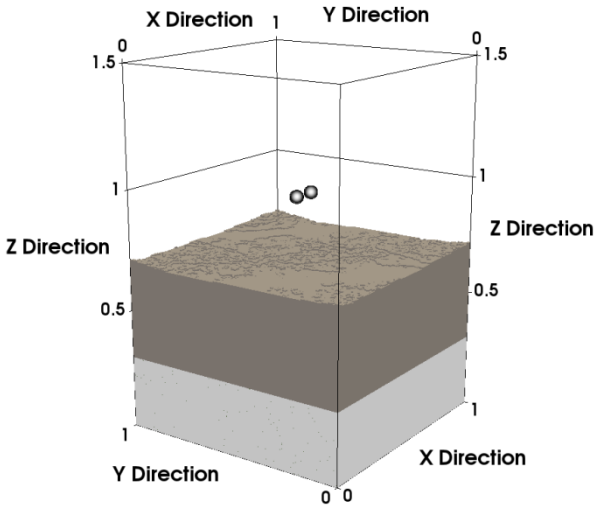

Figure 5-3. Example gprMax model highlighting a 0.40 m thick ballast overlying a 0.30 m thick subballast with the transmitting and receiving antennas suspended 0.25 m above the ballast surface.

5.7. EM Properties Assigned to the Synthetic Model

As has been established, the most critical material properties to consider in the synthetic model are the bulk ε_r and σ of the ballast and the subballast. Variations in these bulk material properties reflect changes in degradation and moisture conditions in the ballast as well as different soil types in the subballast.

Degraded ballast is considered here to be a mixture of four components; aggregate, fines, moisture and air. Each component is characterized by a unique ε_r and a volume-based mixture of the different components yields the bulk ε_r of the ballast ($\varepsilon_{r,ballast}$). In this analysis, $\varepsilon_{r,ballast}$ is determined using the Bruggeman-Hanai-Sen (BHS) volumetric mixing model (Bano 2004, Jol 2009). The BHS mixing model is based on a scale-independent model of spheres-within-spheres. Through the BHS mixing model it is possible to derive four-component $\varepsilon_{r,ballast}$ values based on a series of two-component mixtures. For the two-component mixture of a matrix (ε_m) and a pore fluid (ε_w), with a known porosity (n), the BHS-mixed relative dielectric permittivity (ε_{mix}) in an implicit form is given by:

$$n = \left(\frac{\varepsilon_{mix}-\varepsilon_m}{\varepsilon_w-\varepsilon_m}\right) * \left(\frac{\varepsilon_w}{\varepsilon_{mix}}\right)^c \quad . \qquad \text{[Equation 5-6]}$$

The c factor is related to the shape of the grains and a value of 1/3 is used in this analysis as the grains are assumed to be spherical. Equation 5-6 assumes that the void volume fraction (n) is completely filled by the pore fluid. BHS is one of two common mixing models applied in GPR studies, with the other being the Complex Refractive Index Model (CRIM) (Bano 2004, Theune et al. 2006, Jol 2009). This analysis incorporates BHS as opposed to CRIM as CRIM is intended to estimate bulk ε_r values of layered media.

For use in ballast, the ε_r of the individual components are mixed according to the individual volumes fractions present, to eventually arrive at the bulk $\varepsilon_{r,ballast}$. The volume fractions of fines,

pore moisture, and air are defined in terms of the volume of *void space* each component occupies and vary between 0 and 1. The pore moisture void volume fraction is equivalent to the ballast saturation. The procedure adopted for mixing the individual components first considers the fines and the pore fluid. In this first BHS mixture, the intermediate porosity required by the mixing law is defined as the volume of pore fluid relative to the total volume of fines and pore fluid.

A consequence of defining the volumetric amounts of fines, moisture, and air present within the ballast in terms of the available void space is that the superposition of their volume fractions cannot exceed one, as this would imply more void space is occupied than exists in the modeled ballast. For any combination of fines and saturation whose superposition does not exceed 1, the remaining void space is assumed to be filled by air. The volume fraction of void space filled by air is the second intermediate porosity required during the second BHS mixing step considering the pore fluid/fines ε_{mix} and the ε_r of air. This mixture defines an ε_r of the voids ($\varepsilon_{r,void}$) within the ballast. Finally, $\varepsilon_{r,void}$ is mixed with the ballast aggregate ε_r at the porosity of a clean and dry ballast (ballast free of fines and moisture) to derive the bulk $\varepsilon_{r,ballast}$.

Values for the porosity of a clean and dry ballast as well as the relative dielectric permittivities of ballast aggregate and fines are derived from measurements reported by Kashani et al. (2016). In their study, Kashani et al. (2016) report void ratios, and bulk $\varepsilon_{r,ballast}$ values for various states of ballast degradation. ε_r values for the aggregate and fines components are derived from these bulk $\varepsilon_{r,ballast}$ values using the BHS mixing model, common ε_r values for air and water, and the assumption that the volume fraction ballast aggregate remains constant (0.575). Results of this analysis are summarized in Table 5-1. ε_r values calculated for the ballast aggregate and the fines are within the ranges associated with dry granite and dry sand as presented by Jol (2009).

Table 5-1. Relative dielectric permittivities (ε_r) of the various components of a degraded ballast as calculated from Kashani et al. (2016) or as presented by Jol (2009).

Ballast Component	$\boldsymbol{\varepsilon_r}$
Ballast aggregate	6.5
Ballast fines	4.4
Air	1.0
Pore Water	81.0

With an ε_r defined for each ballast component, $\varepsilon_{r,ballast}$ is calculated for all possible void volume fraction combinations of air, fines, and moisture. Figure 5-4 presents the resulting $\varepsilon_{r,ballast}$ distribution. The inadmissible zone in Figure 5-4 is a consequence of not allowing the superposition of the fines, moisture, and air void volume fractions to exceed one. Specific $\varepsilon_{r,ballast}$ values presented in Figure 5-4 are unique for an aggregate volume fraction of 0.575. A different aggregate volume fraction will yield slightly different $\varepsilon_{r,ballast}$ values for the same saturation and fines void volume fraction levels.

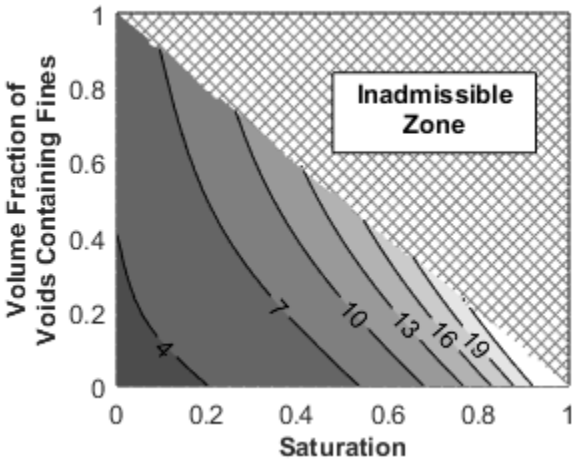

Figure 5-4. Variation in bulk ballast relative dielectric permittivity as a function of the void volume fraction filled with fines and saturation. Values determined using the Bruggeman-Hanai-Sen (BHS) mixing model.

The BHS-derived $\varepsilon_{r,ballast}$ values presented in Figure 5-4 exhibit similar amplitudes and variations as has been observed previously (Clark et al. 2001, De Chiara et al. 2014); bulk $\varepsilon_{r,ballast}$ values increase with increasing void volume fractions containing fines as well as saturations, and the rate of increase associated with increasing saturation is greater. The distribution of $\varepsilon_{r,ballast}$ amplitudes in Figure 5-4 clearly show that a specific value is non-unique. Multiple volumetric combinations of fines, moisture and air result in the same $\varepsilon_{r,ballast}$ value. Non-uniqueness in material properties is a common occurrence in geophysical studies.

During GPR data simulation, to simulate progressive ballast degradation, $\varepsilon_{r,ballast}$ values are extracted from Figure 5-4 and assigned to the ballast in the track foundation model at 21 linearly-spaced fines void volume fraction levels. The specific $\varepsilon_{r,ballast}$ values assigned depend on the ballast saturation. As part of the GPR attribute sensitivity analysis, three ballast saturations are considered; 0, 0.1, and 0.2.

After $\varepsilon_{r,ballast}$, the bulk ballast σ is the material property most influential for GPR. Unlike $\varepsilon_{r,ballast}$, there has been much less characterization of σ at various levels of ballast degradation and moisture content. The authors are also unaware of volumetric mixing model for electrical conductivities directly applicable to a complex composite material such as ballast, which incorporates large aggregates with intervening voids filled with differing volume fractions of fines, water and air. In this analysis, the bulk ballast σ is assumed to be independent of saturation and the void volume fraction filled with fines. The impact of a varying σ is assessed by varying the bulk ballast σ between 1 mS/m and 10 mS/m (Parsons et al. 2014) as part of the model size-dependency analysis.

The EM material properties (ε_r and σ) of the subballast are not treated as thoroughly as those for the ballast as a greater emphasis is placed on the effect large-scale differences in subballast

materials have on the GPR attributes. The bulk subballast material properties are varied in order to represent three general soils types on which ballast may be placed; a dry sand, an average soil, and a wet clay. Table 5-2 presents the bulk ε_r and σ used to represent these soil types (Jol 2009). The specific composition of the average soil is unclear. Based on the EM properties presented in Table 5-2, the soil is considered to be a mixture of sand and clay. For this analysis, variations in the subballast EM material properties are related solely to changes in the subballast materials themselves. Changes in the EM properties resulting from variations in subballast moisture contents are not considered.

Table 5-2. Relative dielectric permittivity (ε_r) and electrical conductivity (σ) for the different subballast materials considered (Jol 2009).

Material Type	**ε_r**	**σ [mS/m]**
Dry Sand	6	1
Average Soil	16	5
Clay	20	200

5.8. Preliminary Data Processing

The synthetic GPR data are read into MATLAB for preliminary data processing and attribute calculation. The synthetic datasets output from gprMax contain the backscattered GPR amplitudes for both the electric and magnetic fields in all three Cartesian directions (x, y and z directions – Figure 5-3) for each simulation. To mimic the common mode of GPR data collection (the TE-mode), all GPR signal interpretation is performed on the electric field component polarized in the same direction as the transmitting antenna (set to be the y-direction).

Preliminary processing of the synthetic GPR datasets involves the removal of the direct wave travelling directly from the transmitting antenna to the receiving antenna. Figure 5-5 presents a series of simulated GPR signals for the physical model presented in Figure 5-3 and dry ballast (Figure 5-4). The main signal in all simulated datasets is the direct wave (~ 4 ns). To remove the direct wave, the signal recorded at the receiving antenna separated 0.10 m from a transmitting antenna while suspended in air was also simulated (Figure 5-6a). This simulation captures only the amplitude of the GPR wave traveling directly between the transmitting and receiving antennae. Figure 5-6b presents the same synthetic dataset as Figure 5-5 after a simple subtraction of the direct wave.

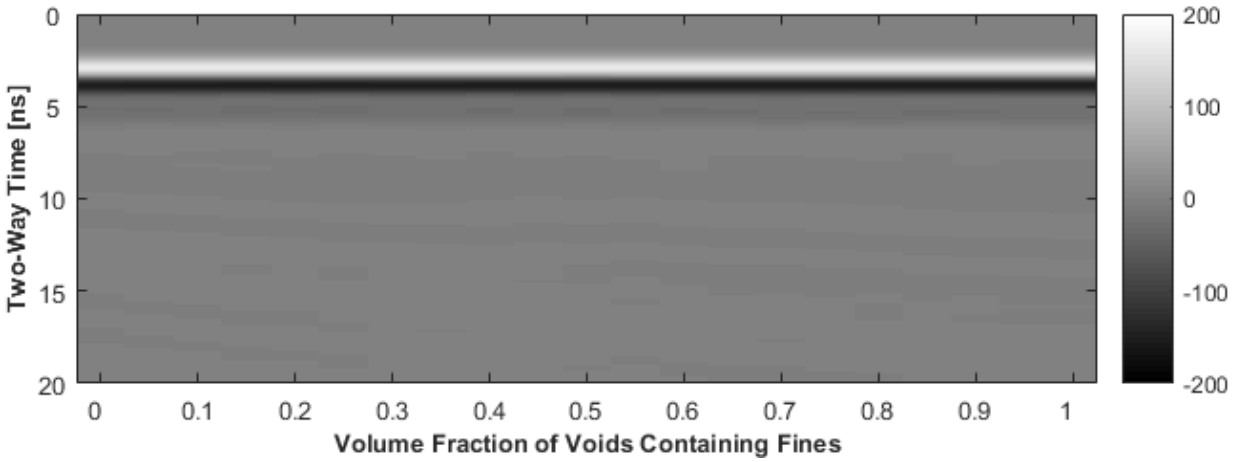

Figure 5-5. Example raw synthetic GPR data dominated by the direct wave.

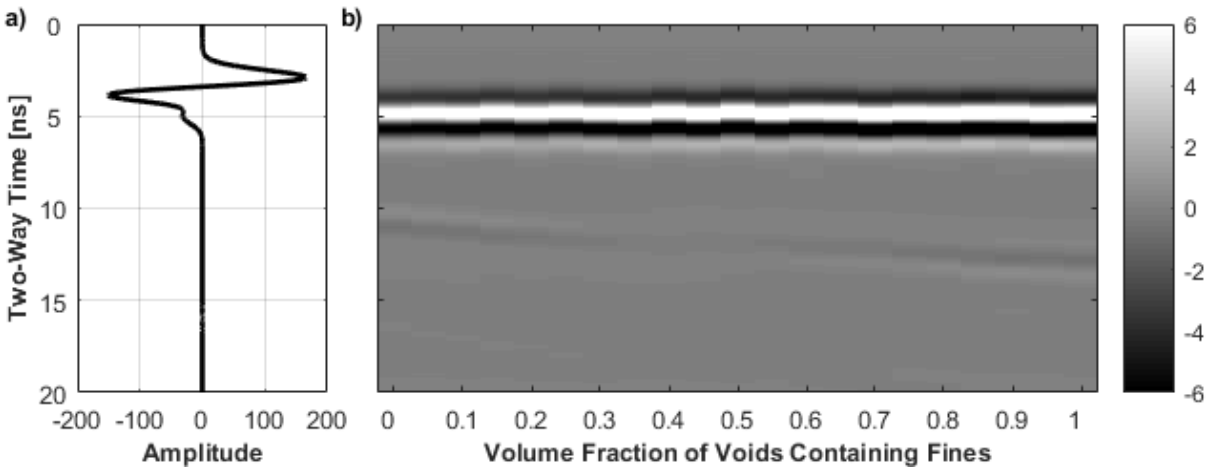

Figure 5-6. a) Direct wave simulated for a transmitting and receiving antenna pair suspended in free space and b) synthetic GPR data after subtraction of the direct wave.

Two reflection 'events' remain after the direct wave removal: a flat-lying reflection from the air-ballast interface at ~5 ns and a weaker and apparently dipping reflection from the ballast-subballast interface. The reflection from the ballast-subballast interface arrives at progressively later two-way times as the volume fraction of voids containing fines increases (increasing $\varepsilon_{r,ballast}$); the thickness of the ballast does not change. The amplitudes of the two backscattered reflections are significantly less than the strength of the direct wave (Figure 5-6a versus 5-6b). The same direct wave removal procedure is applied to all simulated datasets prior to attribute calculation as the orientation of the transmitting and receiving antennas is consistent for all simulations (separated by 0.10 m).

5.9. Modeling Results and Discussion

5.9.1. Model Sensitivity

Prior to evaluating the impact of varying ballast thickness, saturation, and subballast material, the sensitivity of the model to changing physical model dimensions and ballast conductivities is investigated. The purpose of this exercise is to ensure that these factors do not significantly influence the later sensitivity analyses. In these initial simulations the ballast saturation is fixed at 0.2. The GPR attribute results are not affected by variations in the horizontal extent of the model (Figure 5-7a) or by the subballast thickness (Figure 5-7b). As neither lateral model size or subballast thickness influences the GPR attribute results, all subsequent simulations are performed using a lateral model size of 0.50 m and a subballast thickness of 0.30 m to minimize simulation times. In contrast, altering the bulk ballast σ does affect the results (Figure 5-7c), and it is important to discuss these results in more detail.

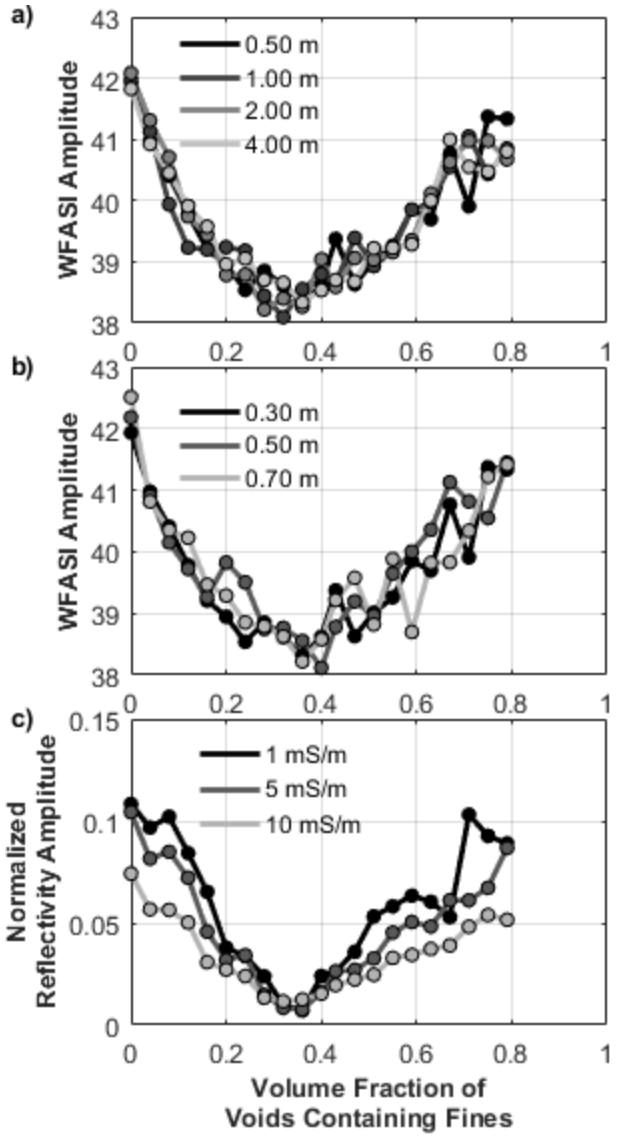

Figure 5-7. Track foundation model sensitivity analysis showing the effect of a) the horizontal dimensions of the model, b) the subballast thickness, and, c) the bulk ballast conductivity. Interpreted GPR data are not sensitive to variations in horizontal model dimensions and subballast thickness; variations in ballast conductivity do exert a systematic influence.

As the bulk σ of the ballast layer is increased (Figure 5-7c), there is a clear systematic flattening in the distribution of the normalized reflectivity amplitudes. A reduction in the proportion of energy associated with the ballast-subballast interface reflection as the bulk σ increases is a result

of increased attenuation within the ballast. Increases in the ballast σ increase the attenuation factor (α – Equation 5-4) and the proportion of energy associated with the ballast-subballast reflection decreases. All subsequent modeling results are simulated assuming a bulk ballast σ of 0.01 S/m.

Every WFASI and normalized reflectivity curve presented in Figure 5-7 is U-shaped. U-shaped WFASI curves are not anticipated based on Silvast et al. (2006) and Silvast et al. (2010), where the authors observed a continuous decrease in WFASI with continually degrading ballast. While based on results presented in Khakiev et al. (2014b), an increase in normalized reflectivity with increasing volume content of fines is expected. A physical explanation for these discrepancies between the simulated results and the previously established observations will be presented in a following section where the similarities between the WFASI and normalized reflectivity results are discussed in-depth.

5.9.2. Propagation Velocity

Relating changes in ballast transit times (Figure 5-6b) to ballast degradation levels through the $\varepsilon_{r,ballast}$ as determined from the GPR propagation velocity is the only approach where ambiguities are not introduced by changes in the known ballast thickness and the nature of the subballast material (Figure 5-8). Figure 5-8a presents the relationship between the $\varepsilon_{r,ballast}$ calculated from the simulated GPR measurements at all three saturation levels (0, 0.1, and 0.2) as the volume fraction of voids containing fines increases. It is clear that varying the depth of ballast does not influence the ability to uniquely estimate fines volume fraction. Figure 5-8b contrasts the calculated $\varepsilon_{r,ballast}$ and the $\varepsilon_{r,ballast}$ originally input in the gprMax model for each simulation. The input $\varepsilon_{r,ballast}$ values are reliably recovered through the estimation of ballast propagation velocities.

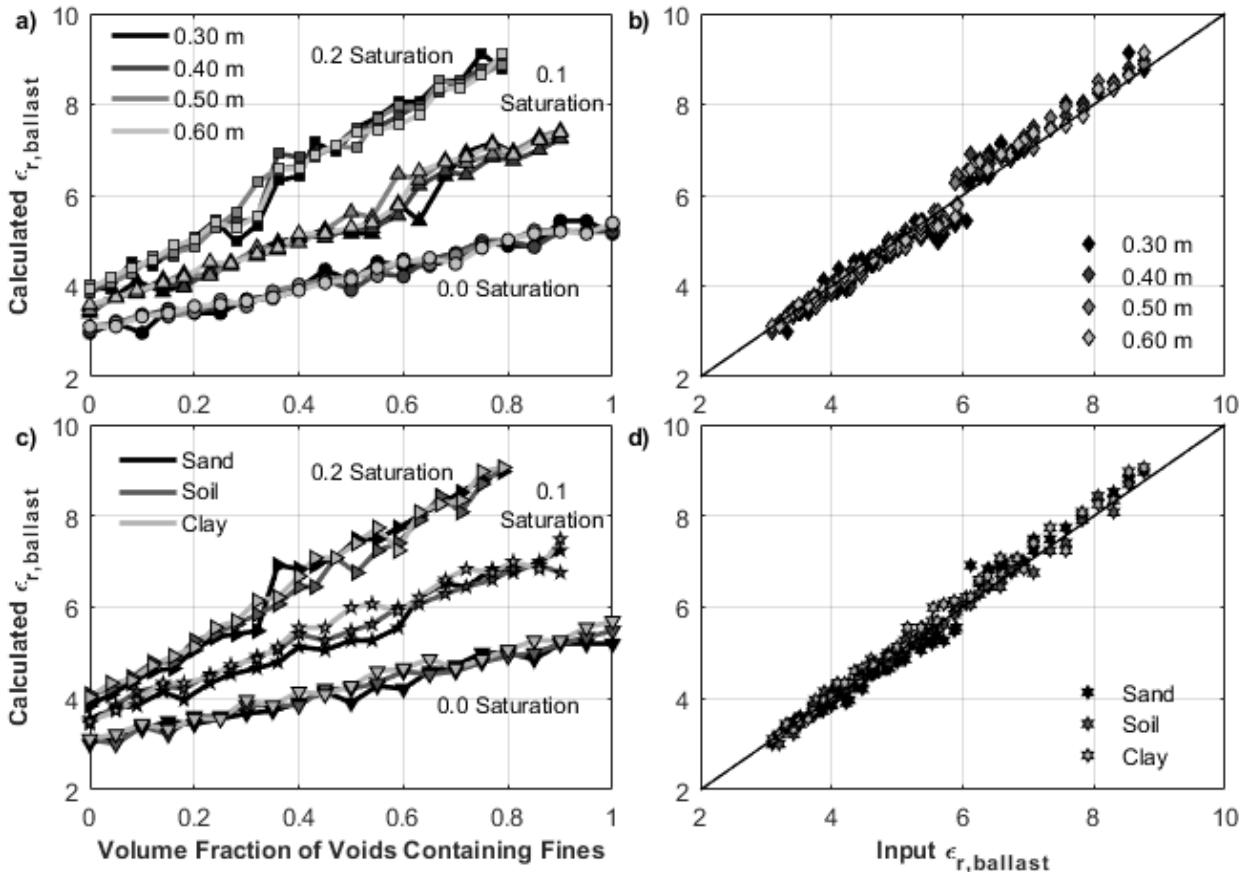

Figure 5-8. Calculated ballast relative dielectric permittivity ($\varepsilon_{r,ballast}$) as a function of the volume fraction of voids containing fines and model input $\varepsilon_{r,ballast}$ showing no systematic effects of changes in ballast thickness [a), and b)] or subballast composition [c), and d)].

There is a slight offset in the linear trend presented in Figure 5-8b at an input $\varepsilon_{r,ballast}$ value of 6.0. This is related to difficulties when manually selecting the ballast-subballast reflection at the point where $\varepsilon_{r,ballast}$ approaches the subballast ε_r. A sand subballast is used in all simulations represented in Figures 5-8a and 5-8b. Following from Equation 5-5, as $\varepsilon_{r,ballast}$ approaches the subballast ε_r the contrast in permittivity across the ballast-suballast interface is small and **a** weak reflection is generated. It is then difficult to accurately select a consistent point on the base-of-ballast reflection. A similar situation is shown in Figure 5-6b where the volume fraction of voids containing fines is equal to 0.5.

Figure 5-8c and 5-8d illustrate the same comparisons as presented in Figures 5-8a and 5-8b but for the situation where the subballast material is varied. A ballast thickness of 0.40 m is assigned to each model. Variations in subballast material do not impact the ability to uniquely determine the volume fraction of voids containing fines at each saturation level (Figure 5-8c). The $\varepsilon_{r,ballast}$ calculated from the synthetic GPR datasets is also very similar to the input $\varepsilon_{r,ballast}$ (Figure 5-8d). The offset in the calculated $\varepsilon_{r,ballast}$ at 6.0 is not as noticeable in Figure 5-8d, compared to Figure 5-8b, as the bulk ballast ε_r is always less than that of a soil or clay subballast (Table 5-2).

The unique relation between the calculated $\varepsilon_{r,ballast}$ and the volume fraction of voids containing fines as ballast thicknesses and subballast materials vary demonstrates the robustness of the GPR propagation velocity attribute. This relation breaks down in the presence of variable ballast saturations. Consider the results for a calculated $\varepsilon_{r,ballast}$ of 4.5 in Figures 5-8a and 5-8c. Depending on the specific ballast saturation, dramatically different inferences of the degradation state of the ballast could be made.

5.9.3. Windowed Fourier Amplitude Spectrum Integral

The sensitivity of the WFASI GPR attribute to changes in ballast thickness, ballast saturation and subballast material are presented in Figure 5-9. Figure 5-9a presents the WFASI results as the thickness of a ballast with a saturation of 0.1 is varied, while Figure 5-9b presents the results as the ballast saturation is varied and the ballast thickness is kept uniform at 0.40 m. A sand subballast is incorporated in all simulations presented in Figures 5-9a and 5-9b. Finally, Figure 5-9c illustrates the impact varying the subballast material exerts on the WFASI results considering a 0.40 m thick ballast with a saturation of 0.2. For all interpretation results presented in Figure 5-9, the base-of-ballast is defined at the first major peak of the ballast-subballast

reflection. This peak may change between positive and negative polarizations depending on the volume fraction of voids filled by fines (see Figure 5-6b).

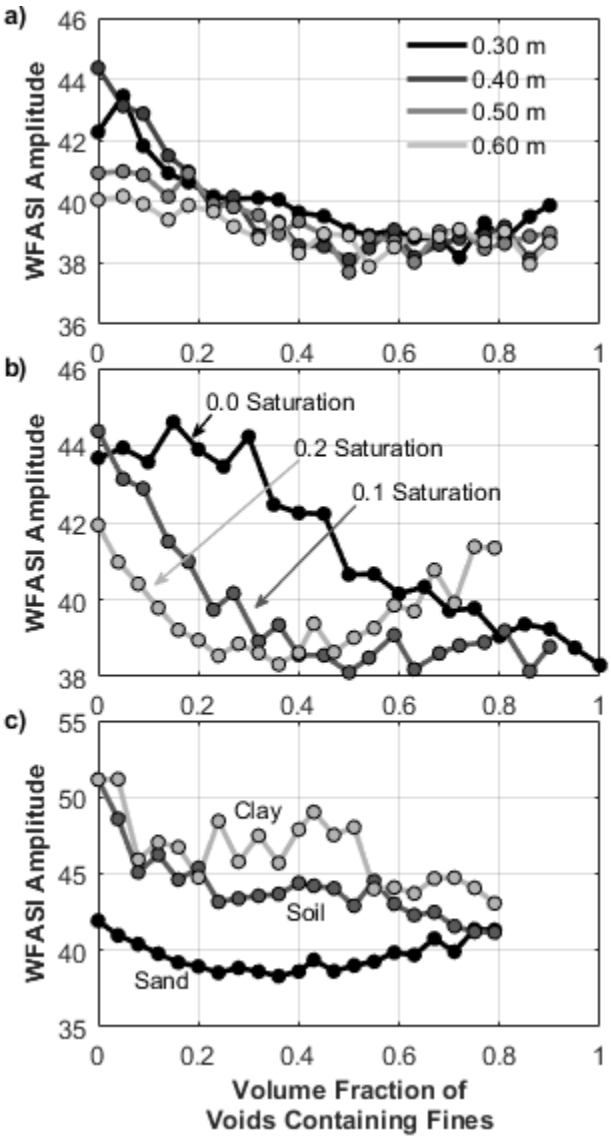

Figure 5-9. Windowed Fourier amplitude spectrum integral (WFASI) attribute results derived from simulated GPR data as a) the ballast thickness, b) the ballast saturation, and c) the subballast material are varied. All variations lead to ambiguities in the WFASI amplitudes with respect to the volume fraction of voids filled by fines.

Modifying the depth of the ballast has the least disruptive effect on the WFASI attribute results (Figure 5-9a). All results are characterized by a decrease in WFASI amplitudes with an increasing concentration of fines until a consistent level is reached after approximately half the void space is filled with fines. The increase in ballast thickness serves to flatten the rate at which the WFASI amplitudes decrease. Situations do exist where the progressive flattening with increasing ballast thickness is not always observed. For the least degraded ballasts (0 to 0.2 volume fraction of voids filled with fines) and 0.30 m and 0.40 m ballast thicknesses, the thicker ballast layer returns larger WFASI amplitudes. This may be related to thin-bed effects in the GPR data. For GPR, a thin-bed is considered to be any layer whose thickness is less than three-quarters of the GPR wavelength (Bradford and Deeds 2006). In clean ballast ($\varepsilon_{r,ballast}$ of 3.5), a 400 MHz GPR wavelength is approximately 0.40 m and the 0.30 m thick ballast layer constitutes a thin-bed. Interference between the air-ballast and ballast-subballast reflections will then impact the WFASI attribute results.

Variations in ballast saturation (Figure 5-9b) and subballast material (Figure 5-9c) dramatically alter both the WFASI amplitudes as well as the general trends in the results leading to significant discrepancies in the inferred amount of fines present in the ballast. WFASI attribute results decrease almost linearly as fines accumulate within the ballast void space for a dry ballast (0 saturation – Figure 5-9b), which is similar to what was observed by Silvast et al. (2006) and Silvast et al. (2010). As the saturation increases, the WFASI amplitudes may decrease until reaching a relatively consistent level or appear U-shaped as fines accumulate in the ballast. The WFASI amplitudes are then indicative of multiple fine concentrations depending on the ballast saturation.

WFASI attribute results exhibit similar general decreasing trends when considering either clay or soil subballasts (Figure 5-9c). A decrease in WFASI amplitudes with increasing ballast degradation is the anticipated behaviour (Silvast et al. 2006, Silvast et al. 2010, Kashani et al. 2016). The soil subgrade results exhibit lower amplitudes for the same void volume fraction filled by fines when compared to the clay subballast results. For sand subballast, the WFASI attribute exhibits a U-shaped pattern and amplitudes that are, in general, significantly less than those calculated for either clay or soil subballast. While a single WFASI amplitude is indicative of different volume fractions of voids filled by fines depending on whether the subballast is comprised of either clay and soil, WFASI results for a sand subballast rarely attain the same amplitude level. The sand subballast results contain their own uncertainty considering that an amplitude of 42 corresponds to either a ballast free of fines or a ballast whose available void space is completely filled by fines.

5.9.4. Normalized Reflectivity

The effects of a variable track foundation on the normalized reflectivity attribute results (Figure 5-10) are very similar to those observed when considering the WFASI attribute (Figure 5-9). Figure 5-10 demonstrates how the normalized reflectivity amplitudes respond to a variable ballast thickness (Figure 5-10a), ballast saturation (Figure 5-10b), and subballast material (Figure 5-10c). Simulated GPR datasets used to derive the normalized reflectivity results presented in Figure 5-10a incorporate ballast with a saturation of 0.2, while those represented in Figure 5-10b incorporate a ballast thickness of 0.40 m. A sand subballast is assigned to all simulations represented in Figures 5-10a and 5-10b. Dry and 0.40 m thick ballast layers are used to generate the synthetic GPR data represented in Figure 5-10c.

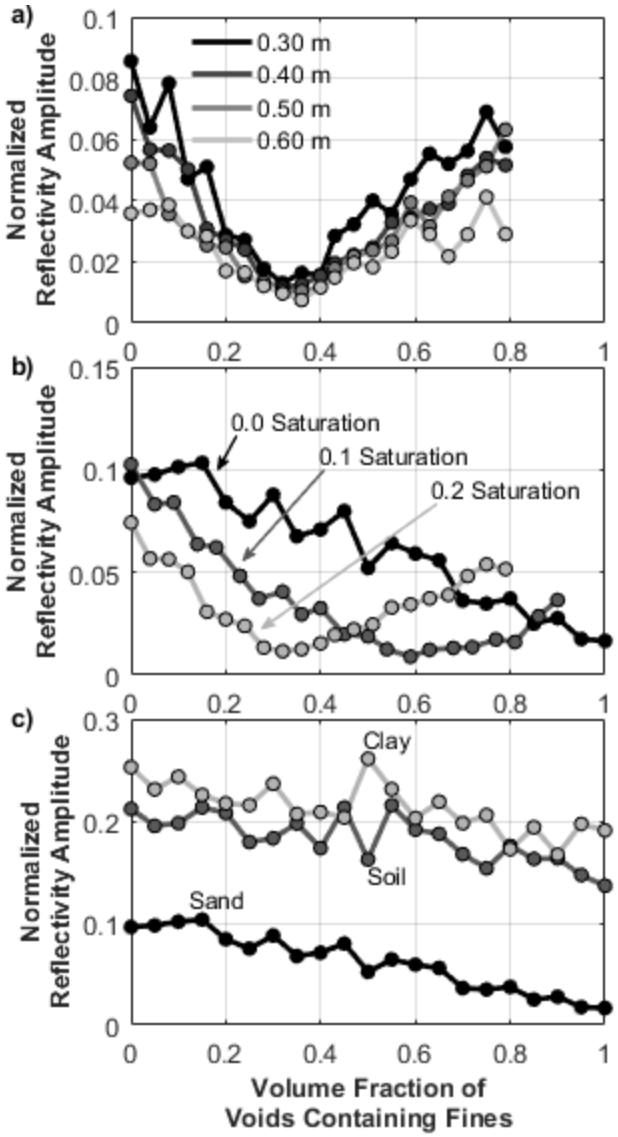

Figure 5-10. Normalized reflectivity attribute results derived from simulated GPR data as a) the ballast thickness, b) the ballast saturation, and c) the subballast material are varied. All variations lead to ambiguities in the normalized reflectivity amplitudes with respect to the volume fraction of voids filled by fines.

In Figure 5-10a, all normalized reflectivity curves exhibit a U-shape that is progressively flattened as the ballast thickness increases. The U-shape and progressive flattening lead to uncertainty in the inferred volume of fines present within the ballast for specific attribute

amplitudes. The normalized reflectivity curves do not exhibit the continuously increasing amplitude with increasing ballast fines content as anticipated based on Khakiev et al. (2014b). This distribution of U-shaped curves in Figure 5-10a is very similar to the normalized reflectivity results presented in Figure 5-7c, where the ballast σ is progressively varied. As with the increase in bulk ballast σ, the flattening of the U-shaped normalized reflectivity curves in Figure 5-10a is attributed to increased signal attenuation as the ballast thickness increases.

The patterns in the normalized reflectivity results related to varying ballast saturations (Figure 5-10b) and subballast materials (Figure 5-10c) are very similar to those observed for the WFASI attribute (Figures 5-9b and 5-9c). Normalized reflectivity amplitudes exhibit a general decrease as the void volume fraction containing fines increases. The only situation where this is not observed is when the ballast saturation is set to be 0.2 (Figure 5-10b). Changes in ballast saturation result in specific attribute amplitudes no longer corresponding to a unique volume fraction of voids filled by fines. A similar situation exists in Figure 5-10c when considering either soil or clay subballasts. The normalized reflectivity amplitudes derived for the sand subballast are significantly lower and do not intersect with those from either clay or soil subballasts.

5.9.5. Similarity between the WFASI and Normalized Reflectivity GPR Attributes

As observed in Figures 5-7, 5-9, and 5-10, a number of the WFASI and normalized reflectivity results exhibit qualitative patterns different to what is anticipated based on previous investigations (Silvast et al. 2006, Silvast et al. 2010, Khakiev et al. 2014b). In many situations, the attribute results are U-shaped as opposed to either the expected continuous decrease (WFASI) or increase (normalized reflectivity). The U-shaped attribute response results from

changes in the reflection coefficient (Equation 5-5) as the volume of the fines component in the ballast increases.

Considering a sand subballast (ε_r of 6.0 – Table 5-2), as fines accumulate within the ballast void space, $\varepsilon_{r,ballast}$ will progressively increase from an initial value below the subballast ε_r (Figure 5-4). The absolute value of the reflection coefficient, and subsequently the strength of the ballast-subballast reflection, decreases as $\varepsilon_{r,ballast}$ approaches the subballast ε_r (Equation 5-5). If fines continue to accumulate within the ballast, $\varepsilon_{r,ballast}$ may begin to exceed the subballast ε_r and the absolute value of the reflection coefficient will increase. The overall result is then a U-shape in the amplitude of the ballast-subballast reflection. Consistently decreasing or increasing trends in the GPR attribute amplitudes can occur depending on which side of the U-shaped distribution the data lie. Whether the reflection coefficient is positive or negative influences the polarity of the ballast-subballast reflection (Figure 5-6b).

Depending on the ballast saturation, the volume fraction of fines within the ballast voids required for $\varepsilon_{r,ballast}$ to meet and exceed the subballast ε_r varies. This is the exact scenario represented in Figures 5-9b and 5-10b. For increasing ballast saturations, the minimum of the U-shaped distribution occurs at progressively lower fines volume fractions. Figures 5-11a and 5-11b present again the WFASI and normalized reflectivity attribute results shown in Figures 5-9b and 5-10b, but instead of being compared with the volume fraction of voids filled by fines, the attribute amplitudes are compared with the $\varepsilon_{r,ballast}$ input into the simulation. In this representation it becomes clear that the separate saturation curves are select portions of a single larger U-shaped pattern. GPR attribute amplitudes may either increase or decrease depending on how the bulk $\varepsilon_{r,ballast}$ varies relative to that of the subballast. GPR attributes derived from simulations

incorporating soil or clay subballasts (Figures 5-9c and 5-10c) do not exhibit this characteristic U-shape, as the bulk ε_r of the subballast is always greater than that of the ballast.

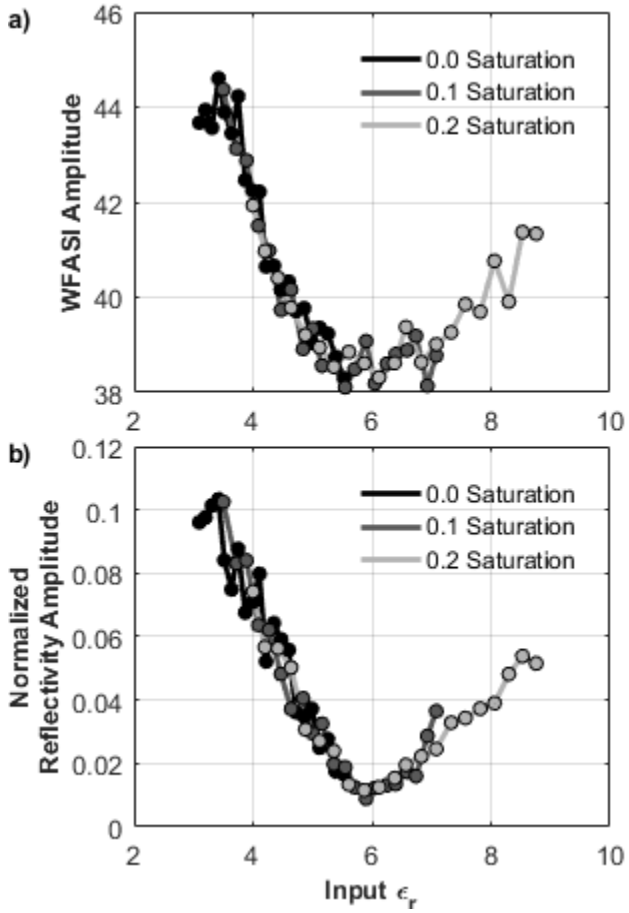

Figure 5-11. Windowed Fourier amplitude spectral integral (WFASI) [a)] and normalized reflectivity [b)] attribute results for different ballast saturations as a function of the input bulk ballast relative permittivity. Different saturation curves are part of the same larger U-shaped behaviour.

Implicitly, U-shaped variations in ballast-subballast interface reflection amplitudes are more likely to manifest in the normalized reflectivity results as this attribute is directly related to the proportional strength of this reflection. U-shaped patterns occur in the WFASI attribute results as a result of where the base-of-ballast is being defined. Recall that the base-of-ballast is defined at

the first major peak in the ballast-subballast reflection. When the windowed trace is transformed to the frequency domain, it does contain a portion of the ballast-subballast reflection energy and, as expressed by Parseval's theorem (Equation 5-7), energy is preserved through Fourier transformation, where *X(f)* is the Fourier transformation of *x(t)*:

$$\int_{-\infty}^{\infty}|x(t)|^2dt = \int_{-\infty}^{\infty}|X(f)|^2df \ . \qquad \text{[Equation 5-7]}$$

Through Parseval's theorem, U-shaped variations in the ballast-subballast reflection energies propagate into the frequency-domain based WFASI results.

Figure 5-12 contrasts the WFASI results when the base-of-ballast is defined at different positions; just prior to the ballast-subballast reflection and at the peaks of the first and second major lobes of the reflection. The WFASI results presented in Figure 5-12 are derived from the simulated GPR measurements of a 0.40 m thick ballast with a saturation of 0.2 and sand subballast. It is clear that if no portion of the ballast-subballast reflection is incorporated in the WFASI calculation, the attribute results exhibit little variation with ballast degradation. Selecting either the first or second major lobe leads to a U-shaped WFASI amplitude distribution. While the shapes of the WFASI distributions are similar when selecting either the first or second major lobes, to uniquely determine the volume of fines present within the ballast the choice of where to define the base-of-ballast must be consistent.

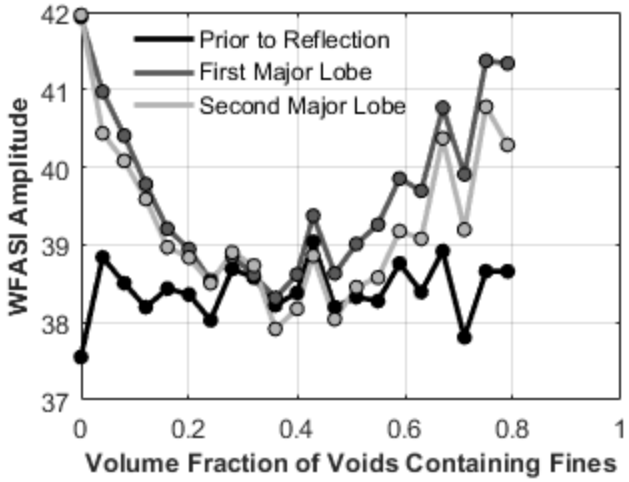

Figure 5-12. Variation in windowed Fourier amplitude spectral integral (WFASI) results as the base-of-ballast is defined at different positions relative to the ballast-subballast reflection.

5.10. Conclusions

Synthetic 400 MHz GPR data have been used to evaluate the impact changes in track foundation conditions have on three GPR attributes used to infer the amount of fines present with the ballast. Estimating ballast degradation from GPR using these attributes has been successfully applied on laboratory and local-scale field data. However, the impact of varying track foundation conditions that would be encountered when analyzing a spatially extensive railway GPR datasets has yet to be thoroughly analyzed. Varying track foundations have been represented by varying ballast thicknesses, saturations, and subballast materials.

A continuum of bulk ballast relative dielectric permittivities has been derived for varying volumetric fines content and saturation combinations using the Bruggeman-Hanai-Sen (BHS) mixing model. Select combinations of fines contents and saturations were chosen and incorporated into GPR data simulation and subsequent attribute calculation. A sensitivity analysis was performed to ensure the size of the simulated track foundation model and the

thickness of the subballast layer did not impact the GPR attribute results. In addition, the impact of different bulk ballast electrical conductivities was also analyzed.

All attributes derived from the simulated GPR measurements could not be related to a unique void volume fraction filled by fines if the ballast saturation was not known. In terms of the bulk ballast permittivity estimates derived through the calculated ballast propagation velocity, this was a direct result of the non-uniqueness of the ballast permittivity in the presence of variable fines contents and ballast saturations. Variable ballast thicknesses and subballast material types did not affect the linear GPR propagation velocity-volumetric fines content relationship. The GPR propagation velocity attribute is limited in that without independently establishing the ballast thickness, the GPR propagation velocity cannot be estimated from single-trace field GPR measurements.

Specific WFASI and normalized reflectivity attributes amplitudes yielded different estimates for the volumetric amounts of fines within the ballast as the ballast thickness and subballast material type were varied. Increasing the ballast thicknesses resulted in a flattening of the attribute distributions and was related to increased signal attenuation within a thicker ballast. Variations in the subballast material altered both the amplitude and shape of the attribute distributions by affecting the TE-mode reflection coefficient. The overall similarity between the WFASI and normalized reflectivity attributes was a consequence of Parseval's theorem and the fact that both attributes included a portion of the ballast-subballast reflection in their respective calculation.

The WFASI and normalized reflectivity attributes can be readily calculated from field GPR datasets, as they do not require any additional information on the track foundation. Therefore, producing reliable qualitative estimates of the amount of fines within the ballast from field GPR data may be possible if the identified track foundation conditions could be constrained. In order

to produce accurate quantitative estimates for the volumetric amount of fines within ballast on a subdivision-scale, ballast thicknesses, saturations and subballast material types must be know at each GPR measurement position.

5.11. Acknowledgements

The authors thank both Canadian National Railway and Canadian Pacific Railway for their support and facilitation of this project. This research was made possible through the Canadian Rail Research Laboratory (CaRRL) (www.carrl.ca), which is funded by the Natural Sciences and Engineering Research Council of Canada, Canadian Pacific Railway, Canadian National Railway, the Association of American Railways – Transportation Technology Centre Inc., the National Research Council of Canada, Transport Canada, and Alberta Innovates – Technology Futures.

5.12. References

Al-Qadi, I.L., Xie, W., and Roberts, R. 2008. Scattering analysis of ground-penetrating radar data to quantify railroad ballast contamination, NDT&E International, **41**(6): 441-447.

Anbazhagan, P., Su, L., Buddhima, I., and Cholachat, R. 2011. Model track studies on fouled ballast using ground penetrating radar and multichannel analysis of surface wave, Journal of Applied Geophysics, **74**: 175-184.

Audley, M. and Andrews, J.D. 2013. The effects of tamping on railway track geometry degradation, Proceedings of the Institution of Mechanical Engineers, Part F: Journal of Rail and Rapid Transit, **227**(4): 376-391.

Bano, M. 2004. Modelling of GPR waves for lossy media obeying a complex power law of frequency for dielectric permittivity, Geophysical Prospecting, **52**: 11-26.

Benedetto, A., Tosti, F., Bianchini Ciampoli, L., Pajewski, L., Pirrone, D., Umiliaco, A., and Brancadoro, M.G. 2016. A simulation-based approach for railway applications using GPR. In The Proceedings of the 2016 16th International Conference of Ground Penetrating Radar (GPR), Hong Kong, pp. 1-6.

Bradford, J.H. and Deeds, J.C. 2006. Ground-penetrating radar theory and application of thin-bed offset-dependent reflectivity, Geophysics, **71**(3): K47-K57.

Chopra, S. and Marfurt, K.J. 2005. Seismic attributes - A historical perspective, Geophysics, **70**(5): 3SO-28SO.

Clark, M.R., Gordon, R., Kemp, T., and Forde, M.C. 2001. Electromagnetic properties of railway ballast, NDT&E International, **34**(5): 305-311.

De Chiara, F., Fontul, S., and Fortunato, E. 2014. GPR laboratory tests for railway materials dielectric properties assessment, Remote Sensing, **2014**(6): 9712-9728.

Gallagher, G.P., Leiper, Q., Williamson, R., Clark, M.R., and Forde, M.C. 1999. The application of time domain ground penetrating radar to evaluate railway track ballast, NDT&E International, **32**(8): 463-468.

Giannakis, I., Giannopoulos, A., and Warren, C. 2016. A realistic FDTD numerical modeling framework of ground penetrating radar for landmine detection, IEEE Journal of Selected Topics in Applied Earth Observations and Remote Sensing, **9**(1): 37-51.

Huang, H., Tutumluer, E., and Dombrow, W. 2009. Laboratory characterization of fouled railroad ballast behavior, Transportation Research Record, **2117**: 93-101.

Hugenschmidt, J. 2000. Railway track inspection using GPR, Journal of Applied Geophysics, **43**(2): 147-155.

Indraratna, B., Tennakoon, N., Nimbalkar, S., and Rujikiatkamjorn, C. 2013. Behaviour of clay-fouled ballast under drained triaxial testing, Géotechnique, **63**(5): 410-419.

Irving, J.D. and Knight, R. 2003. Removal of wavelet dispersion from ground-penetrating radar data, Geophysics, **68**(3): 960-970.

Jol, H. 2009. Ground penetrating radar theory and applications. Elsevier Science, Oxford, United Kingdom.

Kashani, H.F., Ho, C.L., Clement, W.P., and Oden, C.P. 2016. Evaluating the correlation between the geotechnical index and the electromagnetic properties of fouled ballasted track by a full-scale laboratory model, Transportation Research Record, **2545**: 66-78.

Khakiev, Z., Shapovalov, V., Kruglikov, A., and Yavna, V. 2014a. GPR determination of physical parameters of railway structural layers, Journal of Applied Geophysics, **106**: 139-145.

Khakiev, Z., Shapovalov, V., Kruglikov, A., Morozov, A., and Yavna, V. 2014b. Investigation of long term moisture changes in trackbeds using GPR, Journal of Applied Geophysics, **110**: 1-4.

Liu, L., Lane, J.W., and Quan, Y. 1998. Radar attenuation tomography using the centroid frequency downshift method, Journal of Applied Geophysics, **40**: 105-116.

Mishra, D., Kazmee, H., Tutumluer, E., Pforr, J., Read, D., and Gehringer, E.:. 2013. Characterization of railroad ballast behavior under repeated loading: Results from new large triaxial setup, Transportation Research Record, **2374**: 169-179.

Olhoeft, G.R. 2005. Working in a difficult environment: GPR sensing on the railroads. In IEEE Antennas and Propagation Society International Symposium, Washington DC, USA, Vol. 3B, pp. 108-111.

Parsons, R.L., Rahman, A.J., Han, J., and Glavinivh, T.E. 2014. Track ballast fouling and permeability characterization by using resistivity, Transportation Research Record, **2448**: 133-141.

Plati, C., Loizos, A., and Papavasiliou, V. 2010. Inspection of railroad ballast using geophysical method, International Journal of Pavement Engineering, **11**(4): 309-317.

Roberts, R., Rudy, J., Al-Qadi, I.L., Tutumluer, E., and Boyle, J. 2006. Railroad ballast fouling detection using ground penetrating radar - A new approach based on scattering from voids. In Proceedings of the 9th European Conference on Non-Destructive Testing , Berlin, Germany, pp. 1-8.

Roghani, A. and Hendry, M.T. 2016. Continuous vertical track deflection measurements to map subgrade condition along a railway line: Methodology and case studies, Journal of Transportation Engineering, **142**(12): 04016059-1-04016059-8.

Selig, E.T. and Waters, J.M. 1994. Track geotechnology and substructure management. Thomas Telford Ltd., London.

Silvast, M., Nurmikolu, A., Wiljanen, B., and Levomaki, M. 2010. An inspection of railway ballast quality using ground penetrating radar in Finland, Proceedings of the Institution of Mechanical Engineers, Part F: Journal of Rail and Rapid Transit, **224**: 345-351.

Silvast, M., Levomaki, M., Nurmikolu, A., and Noukka, J. 2006. NDT techniques in railway structure analysis. In Proceedings of the 7th World Congress on Railway Research, Montreal, Canada, pp. 1-12.

Su, L., Rujikiatkamjorn, C., and Indraratna, B. 2010. An evaluation of fouled ballast in a laboratory model track using ground penetrating radar, Geotechnical Testing Journal, **33**(5): 1-8.

Sussmann, T.R., Ruel, M., and Chrismer, S.M. 2012. Source of ballast fouling and influence considerations for condition assessment criteria, Transportation Research Record, **2289**: 87-94.

Sussmann, T.R., Selig, E.T., and Hyslip, J.P. 2003. Railway track condition indicators from ground penetrating radar, NDT&E International, **36**(3): 157-167.

Theune, U., Rokosh, C.D., Sacchi, M., and Schmitt, D.R. 2006. Mapping fractures with GPR: A case study from turtle mountain, Geophysics, **71**: B139-B150.

Warren, C., Giannopoulos, A., and Giannakis, I. 2016. gprMax: Open source software to simulate electromagnetic wave propagation for ground penetrating radar, Computer Physics Communications, **209**: 163-170.

Chapter 6: The Spatial Correlation between Track Roughness and Ground-Penetrating Radar Inferred Ballast Degradation

6.1. Contribution of the Ph.D. Candidate

All of the work presented in this chapter was performed by the Ph.D. candidate, including literature review, data processing, analysis, and interpretation as well as manuscript preparation. This chapter details an attempt to correlate track locations exhibiting increased geometrical roughness with the presence of degraded ballast as estimated from field-collected ground-penetrating radar data. The analysis is performed at the full subdivision scale as well as at a highly localized scale where either sustained or increasing trends in track roughness are observed. As supervisors, Dr. M.T. Hendry, Dr. C.D. Martin, and Dr. D.R. Schmitt reviewed all parts of the work. This chapter has been accepted for publication with the following citation;

Scanlan, K.M., Hendry, M.T., Martin, C.D., and Schmitt, D.R. 2018 (accepted December 12 2017). The spatial correlation between track roughness and ground-penetrating radar inferred ballast degradation. Institution of Mechanical Engineers Part F: Journal of Rail and Rapid Transit.

6.2. Abstract

Ballast degradation is considered to be a primary factor contributing to the development of track roughness, and as such it is important to develop efficient techniques to assess the state of the ballast. Ground-penetrating radar (GPR) is one method that has been applied in a variety of railway foundation studies including those attempting to non-destructively assess ballast degradation. However, there has yet to be a large-scale study attempting to correlate GPR-based

estimates of ballast degradation with observed track roughness. This study investigates this correlation along 335 km-long heavy-haul railway subdivision in Alberta, Canada. Track roughness is quantified from repeated track alignment and surface measurements spanning the 15 months prior to GPR data acquisition. Three sets of 400 MHz GPR measurements were performed in August 2012, one along each ballast shoulder and one along the track centreline. The results of this study reveal that significant correlations between the observed track roughness and the GPR-based interpretation of ballast degradation are rare and only exist when the data are compared at very small spatial scales. The absence of significant correlations between track roughness and the estimates of ballast degradation is primarily interpreted as being the result of ambiguous GPR data caused by local scale variations in the track foundation un-related to ballast degradation. To address these issues, potential improvements in the application of GPR as a ballast degradation detection tool are proposed.

6.3. Introduction

Ballast is a fundamental component of railway foundations providing, amongst other functions, resilience against the accumulation of differential track settlements, water drainage pathways, and storage space for fine-grained particles (fines) (Selig and Waters 1994, Sussmann et al. 2012, Li et al. 2016). As fines accumulate within the ballast void space, i.e. ballast degradation, the strength and deformation properties of ballast are altered and the ballast is considered no longer capable of performing its intended functions (Huang et al. 2009, Indraratna et al. 2013, Tennakoon and Indraratna 2014). Differential deformations resulting from ballast degradation are often cited as a primary, but not sole, factor contributing to the development of irregular track geometry (track roughness) along operational railways (Sadeghi and Askarinejad 2009, Sadeghi and Askarinejad 2010, Andrews 2012, Audley and Andrews 2013). However, recent research has

demonstrated that the removal of ballast fines does not always result in a reduction in track variability (Scanlan et al. 2017a). Therefore, in order to efficiently manage track roughness and minimize the potential for vehicle derailment, it is critical for railway operators to continually assess degradation conditions within the ballast as they relate to observed track geometry.

Conventional methods to determine the amount of fines within ballast (sampling followed by sieving or test-pits) are expensive and inefficient for use along spatially extensive (100's of km) railways. Furthermore, visual ballast inspection methods (Sadeghi and Askarinejad 2009, Sadeghi and Askarinejad 2011) cannot account for the accumulation of fines below the ballast surface. Alternatively, ground-penetrating radar (GPR) has been developed and is currently in commercial use as an efficient and non-destructive tool for the detection and quantification of ballast degradation (Gallagher et al. 1999, Al-Qadi et al. 2008, Silvast et al. 2010). At signal frequencies below 1 GHz, GPR can be used to detect degraded ballast as the accumulation of fines within the ballast void space alters the electromagnetic (EM) properties of the ballast layer critical for GPR signal propagation and reflection (Clark et al. 2001, Parsons et al. 2014). The reliable detection of degraded ballast from low-frequency GPR signals is complicated by a demanding operational environment (Olhoeft 2005) as well as potentially unknown and variable track foundation conditions that may introduce ambiguities in the inferred amount of fines (Scanlan et al. 2017b). However, if the influence of these complicating factors can be constrained, reliable estimates of ballast degradation may be derived from GPR measurements.

This paper describes new research into how 400 MHz GPR measurements can be used, based on current industry practices, to evaluate track performance issues; specifically, the development of track roughness. This is accomplished by evaluating the spatial correlation between track roughness and GPR-inferred ballast degradation along a 335 km-long subdivision of heavy-haul

track in Western Canada. Ballast degradation is inferred from the GPR measurements using an industry standard GPR attribute (Silvast et al. 2006, Silvast et al. 2010). Correlations were evaluated at the subdivision scale as well as at a highly-localized scale in an attempt to constrain the influence of unknown track foundation conditions on the GPR-based ballast degradation estimate. The local scale correlations are assessed in sections of track where sustained or increasing trends in track roughness extend through multiple track geometry surveys. The authors are unaware of an existing study that has investigated the spatial correlation between track roughness and GPR-inferred ballast degradation over such an extensive section of railway.

The paper begins with a description of the basic track geometry and GPR datasets and the procedures followed to calculate both track roughness and the GPR attribute related to ballast degradation. This is followed by a discussion of the procedure to co-locate the track roughness and GPR-based datasets, the editing that is required to that combined dataset to remove infrastructure-related signals, and the comparison of the results for the full subdivision. Finally, the specifics of how local sections of rough track are identified from repeated track geometry surveys as well as the spatial association results within these localized areas are presented and discussed.

6.4. Datasets

The track geometry and GPR measurements that form the basis of this study were obtained for a 335 km-long subdivision of heavy-haul railway in Alberta, Canada with annual loads exceeding 50 million gross tonnes (MGT). Maximum freight train speeds vary across the subdivision between 32 km/h (20mph) and 97 km/h (60mph), classifying various sections of the railway as either Class II, III, or IV according to Transport Canada regulations (Transport Canada 2012). Concrete ties and continuously welded rail (CWR) are the dominant tie and rail types across the

subdivision. The railway operator performs track geometry surveys throughout the year while the GPR datasets were collected in August 2012.

An analysis of the Agricultural Region of Alberta Soil Inventory Database (AGRASID) maintained by Alberta Agriculture and Forestry (2012) reveals surficial soil conditions vary significantly across the subdivision. Mineral soils (sands, silts, clays, and tills) as well as organic deposits underlie various sections of the railway. The major soil units identified by AGRASID, either mineral or organic, often contain minor components of other soils (sandy soils with minor clay fractions, or organic soils with minor silt components, etc.) though knowledge of their exact distribution at any point immediately below the track is limited by the resolution of AGRASID (1:100,000).

6.4.1. Track Geometry

The three-dimensional orientation of the rails is quantified with a wide variety of track geometry variables (Transport Canada 2012, Federal Railroad Administration 2014, Li et al. 2016). This analysis focuses on track roughness derived from the surface and alignment geometry variables as both Transport Canada (2012) and the US Federal Railroad Administration (2014) identify these variables, along with track crosslevel, as being the most responsive to the presence of degraded ballast. Crosslevel roughness is not explicitly investigated here as previous studies have shown it to behave similarly to the track surface in response to changes in ballast degradation levels (Scanlan et al. 2017a).

Track surface quantifies the vertical offset between a rail projected onto a vertical plane and the co-planar projection of a reference straight-line chord (with a specific length) at the mid-chord position (defined as a mid-chord offset or MCO) (Li et al. 2016). Similarly, track alignment is **an** MCO measurement, only with the rail and chord projected onto a horizontal plane. As each rail

can be projected separately, track surface and alignment are defined for both the left and right rails individually. Track geometry data used in this analysis are derived from measurements using the common chord length of 18.9 m (62 feet). As alignment and surface are defined relative to an 18.9 m reference chord that is constantly changing orientation with position along the railway, the measured deviations are not equivalent to those that would be measured from a fixed reference location located adjacent to the rails. In addition, the fixed chord length mechanically filters out long-wavelength track geometry signals (Li et al. 2016).

Track geometry data are collected at 0.3 m (one foot) increments along the track using a specially designed railcar. Figure 6-1a presents example surface track geometry data for the left (light gray) and right (dark grey) rails. The overall amplitudes of the measured surface deviations are similar for both the left and right rails. While not shown, similar observations can be made for the alignment track geometry profiles. The track geometry measurements presented in Figure 6-1a were recorded approximately two weeks prior to GPR data collection in August 2012.

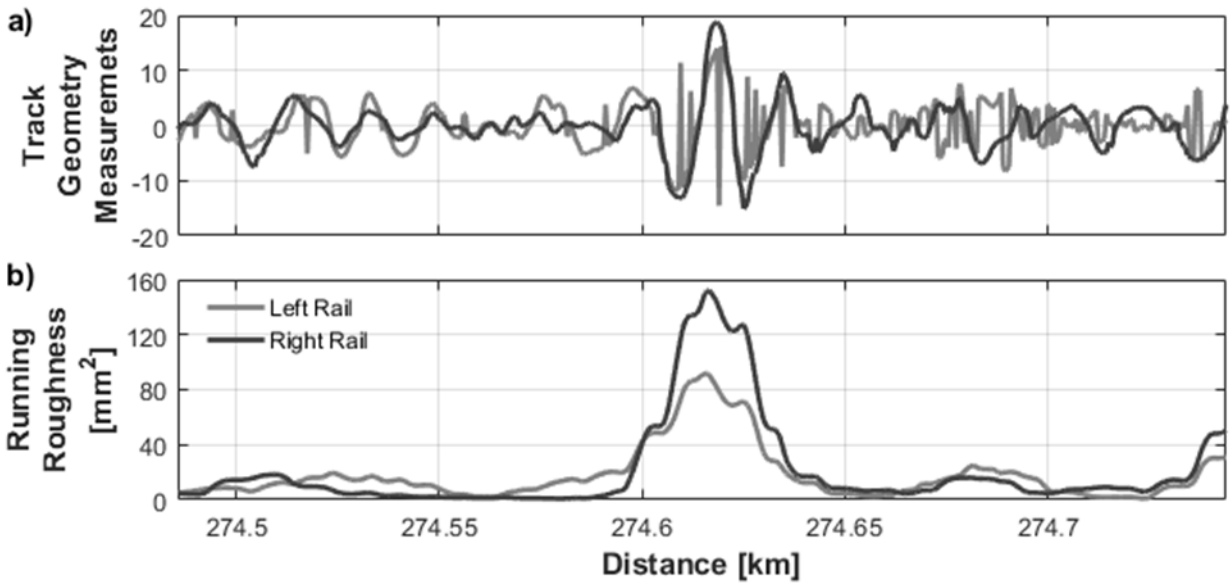

Figure 6-1. Example left and right rail a) 62-foot MCO surface track geometry deviations and b) running roughness profiles based on the deviation measurements. A 20 m filter length is used during running roughness calculation.

6.4.2. Quantification of Track Roughness

The roughness (or variability) in track geometry data can be quantified in multiple ways. A regulated approach in North America is to analyze track roughness by identifying individual locations where the track geometry measurements exceed pre-defined minimum safety thresholds (Transport Cananda 2012, Federal Railroad Administration 2014). For example, the Transport Canada (2012) minimum safety thresholds for the 18.9 m MCO track surface and alignment deviations in Class IV track are 50.8 mm (2 inches) and 38.1 mm (1.5 inches), respectively. For lower class track (Class II or III), larger surface and alignment deviations are permitted. The subdivision selected for this study is very well maintained and an analysis of track roughness in terms of threshold exceedances yields a very sparse and discontinuous dataset. As few thresholds exceedances occur within the section of track under analysis, it is difficult to

reliably compare these limited data with the continuous ballast degradation estimates derived from the GPR data.

Two other common approaches to the quantification of continuous track roughness are 1) as a track quality index (TQI) and 2) as a running roughness. TQIs represent a broad assortment of track roughness measures that are commonly, but not always, based on the standard deviation of one or more track geometry variables (El-Sibaie and Zhang 2004, Sadeghi 2010, Berawi et al. 2010, Sadeghi and Askarinejad 2011, Scanlan et al. 2017a). Many TQIs combine calculated standard deviations from a variety of track geometry variables into a single index value in order to characterize overall track roughness. A limitation of this arithmetic combination is a loss in the ability to identify where in the track foundation that roughness may be originating; as not all track geometry variables reflect changes in the same track foundation components (rails, fasteners, ties, ballast etc.) (Sadeghi and Askarinejad 2009, Transport Canada 2012, Federal Railroad Administration 2014). As this analysis deals specifically with the impact of ballast degradation on track roughness, track roughness as represented by a TQI is deemed to be inappropriate.

In this study, track geometry variability is represented using the running roughness. The running roughness (RR) was developed by Ebersöhn and Selig (1994) as a running average of the square of the measured track geometry deviations (d) and intended to aid in track maintenance planning;

$$RR = \frac{\sum_{i=1}^{n} d_i^2}{n}. \qquad \text{[Equation 6-1]}$$

The number of track geometry measurements over which the squared track geometry deviations are averaged (n) is not a defined value. Li et al. (2016) suggest that the baseline length of track to include in the running roughness calculation be equal to the truck spacing of typical rail vehicles traversing the railway of interest. For this analysis, the length of the running roughness window

is set to 20 m, which is a round approximation for the average length of the various rail vehicles traversing the subdivision. The standard deviation of individual track geometry variables have also been used to relate track roughness to conditions in the ballast (Sadeghi and Askarinejad 2009, Scanlan et al. 2017a). However, both of these studies investigated track roughness within fixed sections of track. As this analysis requires a continuous representation of track roughness, the running roughness is considered the more appropriate metric.

Figure 6-1b presents the running roughness of the surface track geometry data presented in Figure 6-1a. Identification and differentiation between the zones of rough track is clear when the track geometry data are presented in terms of running roughness as opposed to the original measured deviations. A comparison of the left and right rail datasets in Figure 6-1b reveals that the location of rough track is fairly consistent between the left and right rails, although the magnitude of the track roughness may vary. Due to the occasional discrepancy between the left and right rail roughness, the datasets are analyzed individually.

6.4.3. GPR

A common commercial practice within the railway industry is to perform GPR measurements and then use an attribute to estimate ballast degradation without collecting ballast samples to act as a ground-truth or for attribute calibration. The GPR measurements used in this study are collected at 0.2 m increments using three 400 MHz GSSI antennas suspended from a hi-rail vehicle. Each GPR antenna acts as its own transmitter and receiver and individual GPR measurements last for 60 nanoseconds (ns; 10^{-9} seconds) and incorporate a temporal sampling frequency of 8.53 GHz. The three antennas are suspended from the hi-rail in such a way as to allow simultaneous data collection along both ballast shoulders and the track centreline; thereby providing a three-dimensional representation of the railway foundation. GPR antennas acquiring

data along the ballast shoulders are suspended from the rear of the hi-rail vehicle, while the centreline antenna is suspended from the front. The offset between front and rear antennas is 7.6 m while each shoulder antenna is offset 1.2 m from the track centreline.

An example section of raw centreline GPR data is presented in Figure 6-2a. The vertical axis is presented as recorded arrival times as the GPR wave velocity in the track foundation is unknown. A recorded GPR arrival time of a particular subsurface reflection is the time required for the GPR wave to travel from the antenna, reflect off that subsurface impedance contrast and propagate back to the antenna. The main features in the raw GPR data are a series of horizontal bands that span the entire length of the dataset. These bands are interpreted to be a combination of the direct reflection from the steel rails and subsequent signal reverberation between the antenna and the rail. As the steel rails are highly conductive, they preferentially reflect stronger EM waves compared to other track foundation components. As such, the desired signals reflected from within the track foundation (ballast, subballast etc.) require additional data processing (Figure 6-3) in order to become visible. While Figure 6-2a presents only GPR data acquired along the track centreline, the unprocessed left and right shoulder datasets are also dominated by reverberations from the rails.

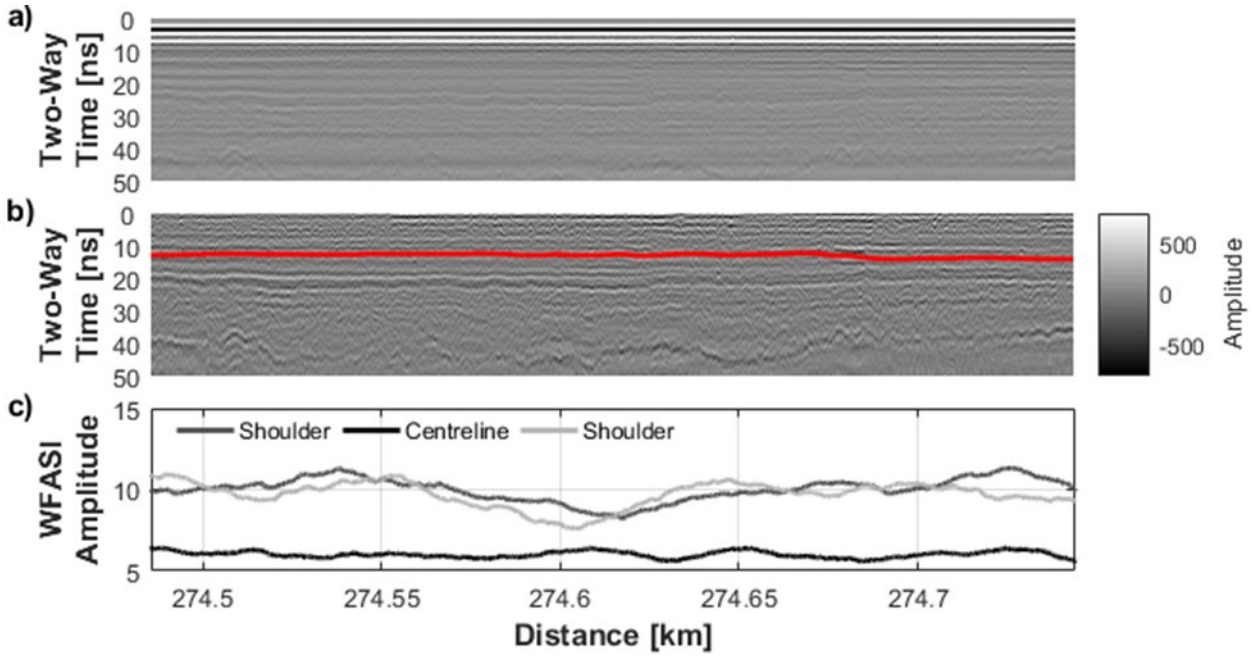

Figure 6-2. Example of an a) unedited and b) processed centreline GPR profile acquired using the 400 MHz GSSI antenna. The user-defined base-of-ballast reflection is overlaid on the processed GPR image [b)]. For each GPR dataset (two ballast shoulders and the track centreline), the WFASI attribute [c)] is calculated based on the user-defined base-of-ballast and subsequently smoothed with a 20 m running average filter.

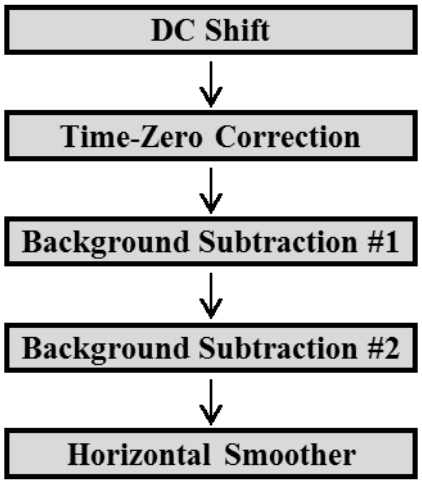

Figure 6-3. Preliminary GPR data processing algorithm applied prior to WFASI attribute calculation.

Scanlan et al. (2017b) demonstrate the significant impact variations in ballast moisture can exert on the ability to accurately infer degradation from low-frequency (<1 GHz) GPR measurements. These moisture related effects are the result of the high dielectric permittivity of the water (~ 80) entrapped within the ballast void space compared to either air (1) or other granular materials (< 10). While no ballast samples were collected at the time of GPR data acquisition, precipitation records for the area may be useful in evaluating the potential for significant moisture variations to be present across the subdivision. Records for five Government of Canada weather stations spread through the subdivision reveal that precipitation exceeding 10 mm occurred in the two weeks prior to GPR data collection at various locations (Government of Canada November 18 2015). While the climatic data also demonstrate that August 2012 was generally hot and dry, the spatial variability in precipitation suggest the potential for moisture variations to exist within the ballast across the subdivision.

A simple data processing algorithm is applied to each GPR dataset in order to remove the direct rail reflection and subsequent signal reverberation, while also enhancing subsurface reflection visibility prior to calculating the attribute related to ballast degradation. The data processing algorithm is presented in Figure 6-3. The processing algorithm consists of five steps; a DC shift, a time-zero correction, two background subtractions, and a horizontal smoothing. The GPR data processing algorithm is purposefully kept very simple in order to minimize data processing artefacts and alterations to the Fourier frequency spectrum (from which ballast degradation will be estimated). Each data processing step in the algorithm is a conventional technique applied to GPR measurements (Jol 2009).

The DC shift and time-zero corrections are applied to each GPR trace individually. DC shifting subtracts the average trace amplitude from each temporal sample along a trace to ensure that the

average track amplitude after correction is zero, while the time-zero correction aligns the first recorded signal to zero nanoseconds. The two background subtraction steps remove the direct rail reflection as well as subsequent reverberations (Figure 6-2a). This is accomplished by averaging all traces within a defined window around a particular trace of interest and then subtracting that average trace from the trace of interest; thereby, removing any common signal. The first background removal operates using a 6000 trace (1.2 km) averaging window (3000 traces on either side of the trace of interest). A long background window preserves the subsurface reflections of interest and it is assumed that the GPR equipment functioned consistently (transmission power, pulse shape etc.) for the entire duration of data collection. The second background removal incorporates a more aggressive window (300 traces – 60 m) but operates solely on the bottom half of the GPR dataset (30 to 60 ns) where long period reverberations continue to persist across the GPR profiles (similar to Figure 6-2a). This second background subtraction has the potential to introduce artefacts into the processed GPR data at 30 ns; however no significant artefacts were observed in the data while deep reflector clarity was enhanced (Figure 6-2b). Furthermore, the portion of the GPR signal related to propagation within the ballast (the portion of interest when estimating ballast degradation) consistently occurs prior to 30 ns. The final horizontal smoothing step removes high-frequency trace-to-trace variability in order to improve the horizontal continuity of the reflectors.

Figure 6-2b presents the raw GPR data from Figure 6-2a preliminary processing. The simple processing algorithm is successful at removing the rail reverberations and highlighting the subsurface reflections. The main reflection of interest is the base-of-ballast interface (highlighted in Figure 6-2b at ~10 ns) and it is the only major reflection traceable along the entire 335 km of track in all three GPR datasets (centreline and both shoulders).

6.4.4. Estimation of Ballast Degradation from the GPR Measurements

After the preliminary data processing just described, a GPR profile (such as that presented in Figure 6-2b) can be used to provide useful information on the track foundation (Hugenschmidt 2000, Sussmann et al. 2003, Fernandes et al. 2008) but detailed interpretations of long track sections remains impractical. A common approach to interpreting geophysical data containing complex waveform information is to reduce the waveform to a single proxy value, an attribute, which correlates with a specific aspect of interest. Variations in these attributes can then be more rapidly assessed by investigators. The specific GPR attribute used in this analysis was developed by Silvast et al. (2006) and Silvast et al. (2010). This attribute is referred to as the windowed Fourier amplitude spectral integral (WFASI) for the remainder of this analysis. The WFASI attribute is not the only attribute that has been used to infer the presence of fines within the ballast from low-frequency GPR data (Clark et al. 2001, Carpenter et al. 2004, Khakiev et al. 2014) but it has the advantage that it can be calculated without requiring the ballast thickness to be known.

The WFASI attribute is based on integrating the normalized Fourier amplitude spectrum derived from GPR data truncated by the picked base-of-ballast reflection (Figure 6-2b). As such, the base-of-ballast was semi-automatically picked at the first negative lobe of the associated reflection across the entire subdivision for each GPR dataset. The Fourier transform, *X(f)*, of the time domain signal truncated by the picked lobe of the base-of-ballast reflection, *x(t),* is defined as

$$X(f) = \int_{-\infty}^{\infty} x(t) \cdot e^{-i2\pi ft} \cdot dt \ , \qquad \text{[Equation 6-2]}$$

where *f* represents linear frequency and *i* represents the imaginary unit ($i=\sqrt{-1}$). The integral of the normalized Fourier amplitude spectra (*WFASI*) can then be defined as

$$WFASI = \int_0^{\infty} \frac{|X(f)|}{max\{|X(f)|\}} \cdot df \ . \qquad \text{[Equation 6-3]}$$

The accumulation of fines raises the dielectric permittivity of the ballast layer (Clark et al. 2001, De Chiara et al. 2014, Scanlan et al. 2017b) and increases GPR signal attenuation. Higher frequency (i.e. shorter wavelength) components of the GPR signal will then attenuate more rapidly and the Fourier amplitude spectrum will decrease in amplitude. As a result, in absence of significant ballast saturation, more degraded ballast will be associated with smaller WFASI amplitudes (Silvast et al. 2006, Silvast et al. 2010, Scanlan et al. 2017b).

With the base-of-ballast interface defined, calculating the WFASI attribute is straightforward (Equations 6-2 and 6-3). Figure 6-2c presents the WFASI data calculated from the processed centreline GPR data presented in Figure 6-2b as well as the WFASI profiles derived from both shoulder GPR datasets. All WFASI data (Figure 6-2c) are smoothed with a running average filter. The mathematical form of the running average is very similar to the derivation of the running roughness (Equation 6-1). The sole difference being that, in place of the squared track geometry deviations (d_i^2), the calculated WFASI amplitudes are included in the summation. As with the running roughness, a 20 m window is used during WFASI smoothing. The WFASI amplitudes for each shoulder dataset in Figure 6-2c are significantly larger than those for the centreline antenna. Due to expected variations in the track foundation (Scanlan et al. 2017b) and without samples for calibration, the amount of ballast degradation associated with a specific WFASI amplitude cannot quantitatively be determined. In this study, each WFASI dataset is analyzed individually and only the *relative* changes in WFASI amplitude are considered.

The ability of GPR measurements and the WFASI attribute to detect zones of relative ballast degradation ballast appears spatially variable. This is likely an effect of other factors in the track foundation (variations in ballast thickness, conductivity, clean ballast void ratio etc.) influencing

GPR signal attenuation in addition to the effects of ballast degradation (Scanlan et al. 2017b). Figure 6-4 illustrates this spatial variability for a section of track that had recently undergone ballast renewal (undercutting). In this section, ballast prior to 6.44 km had undergone renewal (cleaning) in May 2011 while ballast beyond 6.6 km was maintained in September 2010 (15 and 22 months prior to GPR data collection respectively). There is a clear step decrease in the centreline WFASI profile at 6.44 km as would be expected at an increase in relative ballast degradation. Beyond 6.6 km the centreline profile does not exhibit an increase in WFASI amplitudes. The darker shoulder WFASI profile presents the opposite scenario to the centreline WFASI profile. No change in WFASI is observed in response to the 2011 undercutting, while a slight increase is observed at the boundary between the non-maintained ballast and the 2010 undercutting. The lighter shoulder profile is unaffected by either ballast renewal. As it is not possible to isolate only those locations where the WFASI profiles accurately reflect changes in relative ballast degradation without calibration, the entire WFASI dataset is carried forward for comparison with track roughness.

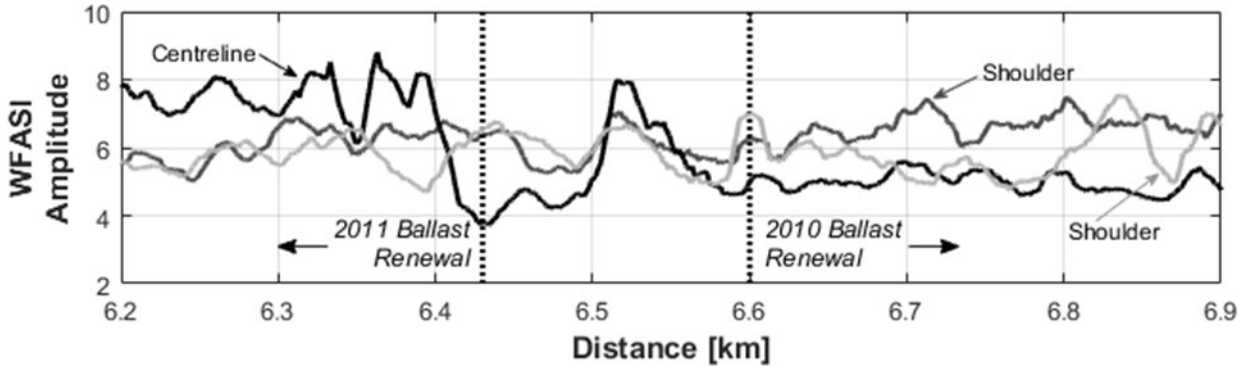

Figure 6-4. Comparison of the three WFASI profiles in the region of two recent ballast renewals (undercutting) performed in September 2010 and May 2011. The centreline WFASI profile demonstrates the expected increase in WFASI amplitudes in the region of relatively less degraded ballast corresponding to the 2011 renewal but no associated increase is observed for the 2010 ballast renewal. The darker shoulder WFASI profile exhibits a slight increase in WFASI amplitude for the 2010 ballast renewal but not for the 2011 renewal, while the remaining shoulder profile exhibits no significant effects related to ballast renewal.

6.5. Combining the Track Geometry and GPR Datasets and Infrastructure Removal

In order to assess the correlation between the running roughness and WFASI measurements, the two datasets must be defined at the same spatial position. Combining the datasets onto the same spatial axis is facilitated through the GPS location data that are collected with each track geometry measurement and at five meter increments during GPR data collection. Comparison GPS locations are derived from the GPR GPS measurements at 0.5 m increments. The 0.5 m increment is chosen as it is a simple fraction of the GPR GPS recoding interval. WFASI values at the comparison locations are interpolated from the individual full-resolution (0.2 m increment) WFASI datasets. Running roughness values (left and right rail measurements for both surface and alignment) within a 0.5 m radius surrounding each comparison location are averaged together to define the running roughness value at that comparison location. If no running

roughness measurements are found within the 0.5 m radius, the closest roughness measurement within five meters is assigned to the comparison point. A comparison location is removed from the combined dataset if no track roughness measurement occurs within five meters of the defined GPS position. Interpolating the WFASI data and assigning the running roughness data to each common comparison location does not result in a significant loss of resolution as all datasets have previously been smoothed with a 20 m moving average filter.

A final consideration that must be made prior to correlating the running roughness and WFASI datasets is related to the effects of track infrastructure (switches, crossings, culverts, and bridges). As presented in Figure 6-5a, GPR measurements in the presence track infrastructure are substantially different than those in a typical track foundation (Figure 6-2b). At these locations, the calculated WFASI amplitudes are no longer representative of conditions within the ballast but are strongly influenced by reflections off of the track infrastructure. Locations of track infrastructure also correspond to increases in track roughness (Figure 6-5b). Slight spatial positioning offsets in the track infrastructure effects between the GPR and track geometry datasets (Figure 6-5) are the result of GPS inaccuracies between in the two sets of GPS locations. To ensure that track infrastructure effects are not influencing the correlation results, each section of track affected by track infrastructure is identified in the GPR profiles, and all data in these areas, as well as those within a 30 m extension on each side, are removed from the combined dataset. The 30 m extension on each side of the identified track infrastructure accounts for the smoothing applied during running roughness and WFASI data calculation as well as any GPS accuracy issues.

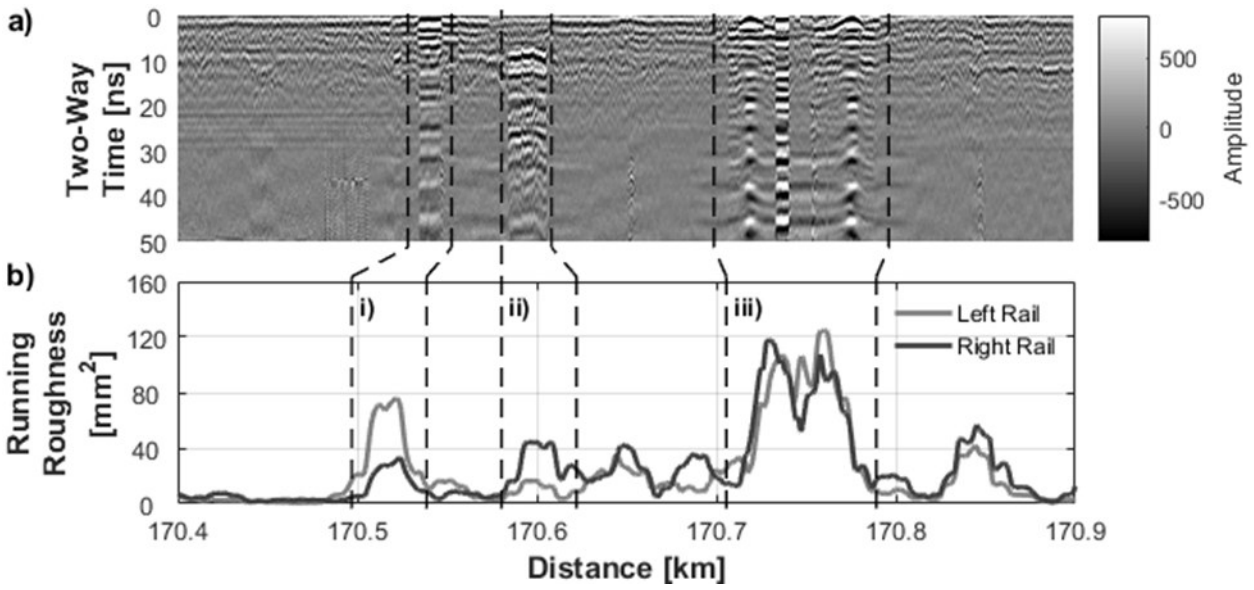

Figure 6-5. Processed centreline GPR [a)] and surface running roughness [b)] data demonstrating the impact of track infrastructure; specifically, i) a crossing, ii) a culvert, and iii) a turnout. Locations of track infrastructure are removed prior to contrasting the WFASI and running roughness datasets.

6.6. Full Subdivision Comparison of Track Roughness and Ballast Degradation Estimate

The first attempt at cross-correlating the running roughness and WFASI datasets is performed using all available measurements (i.e. at the subdivision scale). The relative strength of the linear correlation of two datasets (A and B) is captured by Pearson's correlation coefficient (R):

$$R(A,B) = \frac{1}{N-1}\sum_{i=1}^{N}\left(\frac{A_i-\mu_A}{\sigma_A}\right)\left(\frac{B_i-\mu_B}{\sigma_B}\right). \quad \text{[Equation 6-4]}$$

R varies over the range [-1 1]; where values of -1 and 1 imply perfect negative and positive correlations, respectively. N represents the number of data points in the two datasets being compared, while $\mu_{A,B}$ and $\sigma_{A,B}$ are the mean and standard deviations of the data in A and B, respectively. If a spatial correlation between rough track and increased ballast degradation does exist, the resulting R value will be negative. This is a result of the WFASI amplitudes decreasing

as fines accumulate within the ballast (Silvast et al. 2006, Silvast et al. 2010, Scanlan et al. 2017b).

Figure 6-6 presents the results when the left rail surface running roughness is cross-plotted against the WFASI derived from the centreline GPR antenna at each comparison point. The running roughness dataset compared with the WFASI in Figure 6-6 is derived from the track geometry survey performed in August 2012. The R value for the two datasets presented is 0.01; indicating no significant correlation between track roughness and GPR-inferred ballast degradation. Similar R values are calculated for each combination of running roughness (left or right rail, surface or alignment) and each WFASI dataset (centreline and two ballast shoulders).

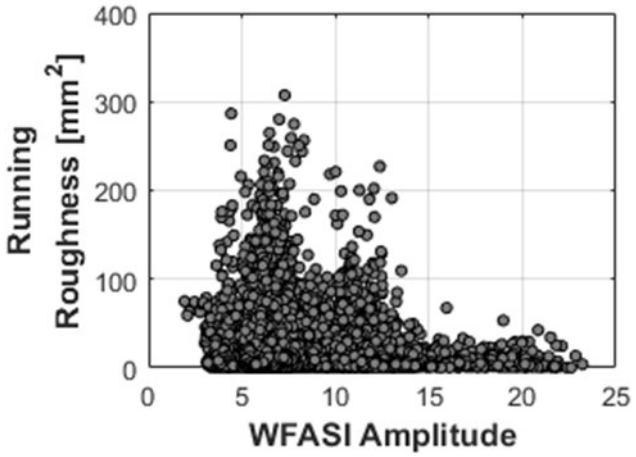

Figure 6-6. Full-subdivision comparison of the centreline WFASI and the left rail surface running roughness. No universal association is observed between the estimates of ballast degradation and track roughness. A similar result is observed for all possible combinations of a WFASI dataset (ballast shoulder or track centreline) and a running roughness dataset (left and right rail alignment and surface).

An alternative approach to investigate the existence of a subdivision scale association between degraded ballast and track roughness is through their respective amplitude distributions. If a subdivision scale association exists between the two data types, a noticeable shift towards higher

roughness values in the running roughness amplitude distribution would be expected when considering only those track positions where the WFASI amplitude is assumed to be indicative of relatively more degraded ballast. Similarly, a shift towards lower WFASI amplitudes would be expected when the amplitude distribution is restricted to those track positions exhibiting increased track roughness.

Figures 6-7a presents the distribution of left rail surface running roughness amplitudes for all track positions, while Figures 6-7b and 6-7c present the running roughness amplitude distributions for track positions where the centreline WFASI amplitude is either less than or equal to five (Figure 6-7b) or exceeds five (Figure 6-7c). There is no change in the shape of the running roughness amplitude distribution when considering only those positions where the centreline WFASI amplitude exhibits its smallest values (indicative of relatively more degraded ballast – Figure 6-7b). An analysis performed on the centreline WFASI amplitude distributions [Figures 6-7(d-f)] yields a similar result, as there is no noticeable shift in the WFASI amplitude distribution when considering the roughest track positions (>30 mm^2 – Figure 6-7f). The absence of changes to the amplitude distributions imply that a subdivision scale association between track roughness and GPR-inferred ballast degradation does not exist. All combinations of track geometry variables and WFASI antennas yield the same result.

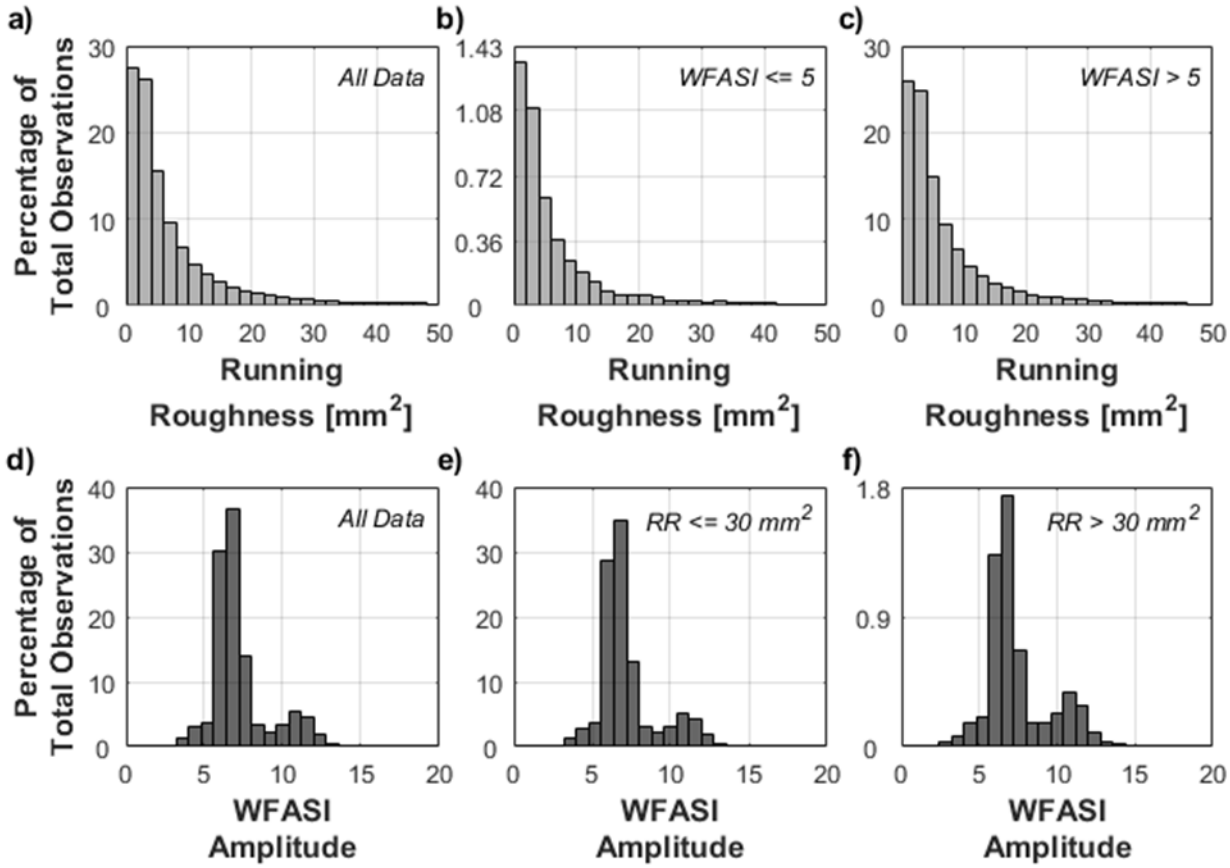

Figure 6-7. Distribution of left rail surface running roughness and centreline WFASI amplitudes across the full subdivision [a) and d)], when restricted to locations where the WFASI and running roughness amplitudes are less than or equal to b) 5 or e) 30 mm^2 respectively, and when restricted to locations where the WFASI and running roughness amplitudes exceed c) 5 or f) 30 mm^2. There is no significant change in either the running roughness or WFASI distribution when the other variable is considered to be indicative of solely degraded ballast [b) - WFASI <= 5] or rough track [f) - running roughness > 30 mm^2].

The running roughness of 30 mm^2 and the WFASI amplitude of five were used to restrict the individual datasets based on the full amplitude distributions (Figure 6-7a and 6-7d). The 30 mm^2 threshold isolates the roughest sections of track, while a WFASI amplitude of five isolates the sections of track exhibiting the smallest WFASI values. Based on Sadeghi (2010), a 30 mm^2 running roughness is indicative of the track being in an "average" condition and is well below

the maintenance and safety thresholds for the different classes of track encountered along the subdivision (Transport Canada 2012); however, only a small proportion of roughness values exceed this 30 mm^2 threshold. A WFASI amplitude of five cannot be associated with a specific amount of fines; however, based on theoretical expectations, the smallest WFASI amplitudes are the most likely to be associated with degraded ballast (Silvast et al. 2006, Silvast et al. 2010).

Little to no spatial correlation between track roughness and degraded ballast at the subdivision scale is not unexpected due to a number of factors. Sadeghi and Askarinejad (2009) demonstrate that variable track surface and alignment measurements are not uniquely associated with the condition of the ballast and may also be influenced by the condition of the ties, fasteners, and rail. In addition, Scanlan et al. (2017b) highlight that variation in ballast thicknesses, saturations, conductivities, pre-degradation void ratios and subballast materials lead to variations in WFASI amplitudes for 400 MHz GPR measurements even while the level of ballast degradation is constant. At the time of GPR data acquisition, it was unlikely that the clean ballast void ratio and ballast thickness were constant across the 335 km-long subdivision and as demonstrated by the historical precipitation records as well as the surficial soil maps, variable ballast saturations and subballast materials were also present. Finally, the running roughness measurements presented in Figures 6-6 and 6-7 are the result of a single track geometry survey performed approximately two weeks before GPR data collection. Scanlan et al. (2017a) demonstrate that long-term trends in track roughness are influenced by the amount of fines within the ballast. The individual track geometry survey measurements incorporated in Figures 6-6 and 6-7 provide no information on the long-term trends in track roughness and are strongly affected by recent track maintenance. In light of these issues, a local-scale cross-correlation of the trends in track roughness and WFASI is required.

6.7. Identifying Local Sections for Cross Correlation

A three step process is used to identify the sections of track exhibiting sustained or increasing running roughness (local sections of interest) in each of the four track geometry datasets (left and right rail surface and alignment). The process is as follows;

I. Running roughness amplitudes above a certain threshold limit must occur in more than half the track geometry surveys considered,

II. Running roughness amplitudes above a certain threshold limit must occur in the three most recent track geometry surveys, and

III. The trend in running roughness across all track geometry surveys considered must be either flat (sustained rough track – slope of zero) or increasing (positive slope).

A minimum running roughness threshold is used in Steps I and II to avoid extracting track positions where the trend in running roughness is sustained or increasing but the actual running roughness amplitudes are small. Steps I and II also ensure that large amplitude running roughness values in the earliest track geometry surveys or recent corrective maintenance (tamping) do not influence the trend in running roughness calculated in step three. If the above three conditions are satisfied, the track location is identified as a section of further interest and extracted for cross correlation with the WFASI datasets.

Figure 6-8 presents an example of the identification process. All track geometry surveys performed in the 15 months prior to GPR data collection (May 2011 through August 2012) are used to locate the sections of interest (Figure 6-8a). The increasing trend in the left rail running roughness in the middle of the section is clearly visible and is not affected by any early onset roughness or recent track maintenance. Adjacent or slightly adjacent (within 15 m) individual locations satisfying above conditions are combined into a single section of interest (Figure 6-8b).

Similar to Figure 6-7, a running roughness threshold of 30 mm^2 is used to identify the roughest track sections for both surface and alignment. The same running roughness threshold is applied to both track geometry variables in order to maintain uniformity in the running roughness amplitudes within each local section of interest. Manual inspection revealed that the 30 mm^2 threshold consistently identified the main local scale track sections of interest. In total, 51, 41, 369, and 369 local sections of interest are identified in the left and right rail alignment and the left and right rail surface datasets. The 51 local sections of interest identified from the repeated left rail alignment measurements cover a total combined track length of 12.3 km, while the local sections of interest identified from the repeated right rail alignment as well as left and right rail surface measurements contain 10.0, 91.2, and 90.8 km of track, respectively.

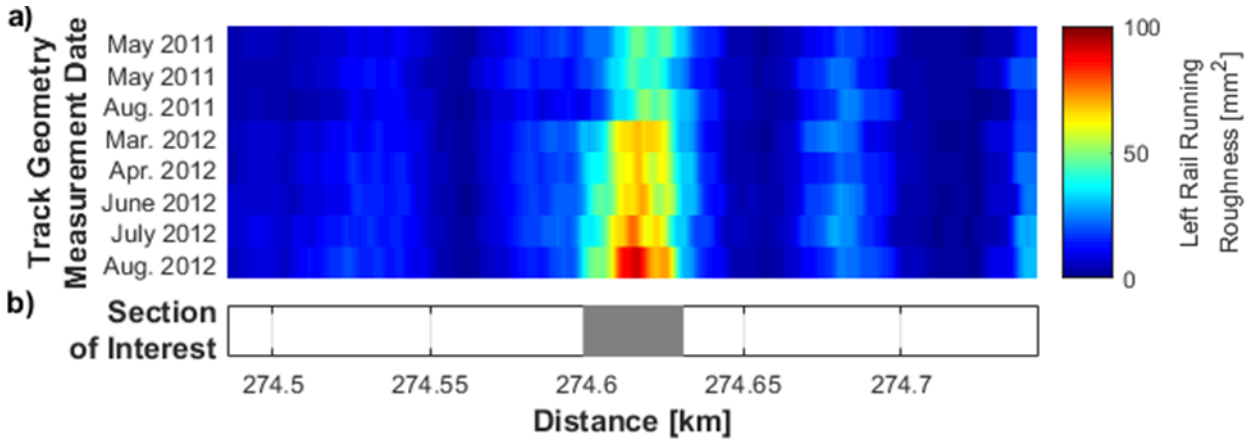

Figure 6-8. Repeated track geometry survey results demonstrating increasing running roughness [a)] and b) the local section of interest identified for further analysis.

6.8. Local Comparison of Running Roughness and WFASI

The number of local sections of interest exhibiting an R-value less than -0.5 are summarized in Tables 6-1 and 6-2 for the alignment and surface track geometry variables, respectively. For the purpose of this analysis, an R-value less than -0.5 is considered to indicate a significant spatial

association between track roughness and the WFASI representation of ballast degradation. The -0.5 significance threshold is **arbitrary** but captures the anticipated relationship. As mentioned, the WFASI amplitude will decrease in the presence of degraded ballast (Silvast et al. 2006, Silvast et al. 2010) and the expected R-value when cross correlated with increasing running roughness will be negative. Also, as surface and alignment roughness are most strongly, but not solely, related to conditions in the ballast (Sadeghi and Askarinejad 2009, Scanlan et al. 2017a), the absolute value of the resulting R-value is expected to be large but not necessarily one. Similar to the full subdivision investigation (Figure 6-6), local-scale R-values are derived from a cross correlation (Equation 6-4) of the WFASI datasets with the August 2012 running roughness results (the track geometry survey the most contemporaneous with GPR data collection). An additional 100 m of data on either side of the section of interest is included during cross correlation to provide context for what is observed at the section of interest.

Table 6-1. The number of local track alignment sections of interest detected within the subdivision and amount of those that demonstrate significant R values when cross-correlated with a specific WFASI profile.

	Left Rail Alignment			**Right Rail Alignment**		
	WFASI Dataset			**WFASI Dataset**		
	Shoulder	*Centreline*	*Shoulder*	*Shoulder*	*Centreline*	*Shoulder*
Number of Local Sections of Interest	51			41		
Number (Percentage) of Local Sections Yielding Significant R-values	3 (5.88%)	1 (1.96%)	1 (1.96%)	2 (4.88%)	0 (0.00%)	1 (2.44%)

Table 6-2. The number of local track surface sections of interest detected within the subdivision and amount of those that demonstrate significant R values when cross-correlated with a specific WFASI profile.

	Left Rail Surface			**Right Rail Surface**		
	WFASI Dataset			**WFASI Dataset**		
	Shoulder	*Centreline*	*Shoulder*	*Shoulder*	*Centreline*	*Shoulder*
Number of Local Sections of Interest	369			369		
Number (Percentage) of Local Sections Yielding Significant R Values	19 (5.15%)	20 (5.42%)	16 (4.34%)	20 (5.42%)	30 (8.13%)	12 (3.25%)

For both track alignment (Table 6-1) and track surface (Table 6-2), the proportion of local sections of interest where increasing track roughness successfully correlates with increases in relative ballast degradation is small (< 10%). Contrasting Tables 6-1 and 6-2 highlights that a slightly greater proportion of the local rough track surface sections (Table 6-2) correlate significantly with the WFASI than what is observed considering track alignment (Table 6-1). The slight discrepancy is not unexpected as variability in track alignment is also heavily influenced by tie conditions (Sadeghi and Askarinejad 2009). As a result, the proportion of significant correlations between the track surface running roughness and the WFASI would be expected to be greater as track surface is more directly related to ballast conditions.

With the exception of the right rail surface (Table 6-2), there is no strong systematic difference in the proportion of significant R-values calculated for the three WFASI datasets and each track geometry variable considered. However, significant R-values are rarely calculated for each of the WFASI datasets within the same local section of interest. For the majority local sections exhibiting significant R-values, these R-value are isolated to a single WFASI dataset. Figures 6-9, 6-10, and 6-11 present example local sections of interest where the historical surface running roughness profiles (left and right rail) are plotted with the WFASI profiles calculated from each

GPR antenna. In each of Figures 6-9, 6-10, and 6-11, the running roughness profiles are represented by the solid lines and the thick solid lines reflect the running roughness derived from the August 2012 track geometry survey.

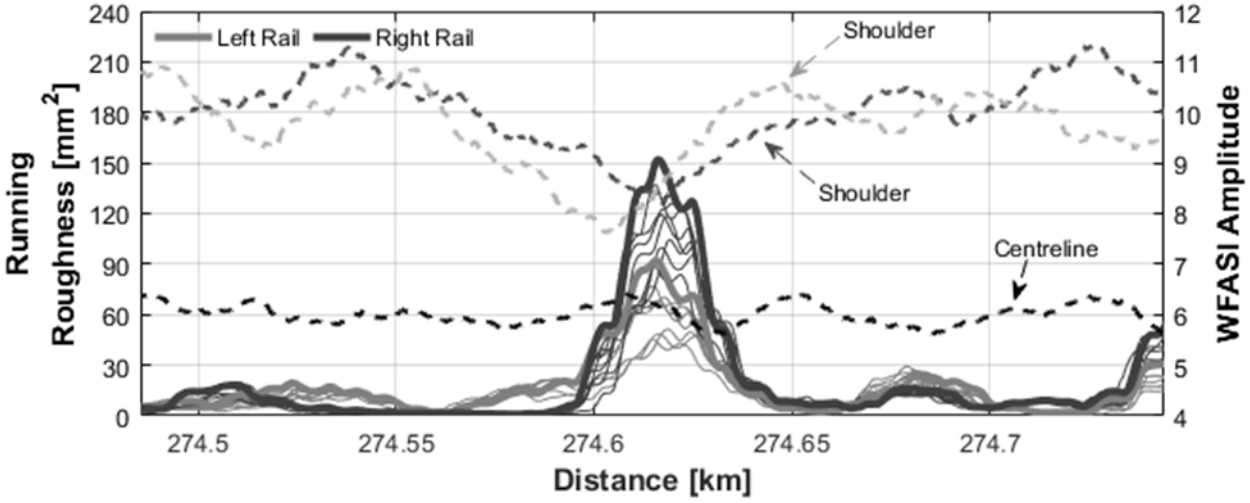

Figure 6-9. A local comparison of the two surface running roughness (solid) profiles and the three WFASI (dashed) profiles. The thicker solid lines highlight the most recent running roughness profiles (August 2012) that are cross-correlated with the WFASI profiles. Significant R values of -0.72 and -0.60 are derived for the left rail surface running roughness and the two shoulder WFASI datasets. A significant R value (-0.69) is also derived from the cross-correlation of the most recent right rail surface running roughness profile and the darker shoulder WFASI dataset. In this local section, no significant R values are calculated when considering the centreline WFASI data.

Figure 6-9 presents an example section of interest where the increase in track roughness successfully correlates with a local decrease in both shoulder WFASI profiles. Significant R-values are calculated from a cross correlation of the left rail running roughness and both shoulder WFASI datasets (-0.72 and -0.60), while only the right rail running roughness and the darker shoulder WFASI dataset yield a significant R-value (-0.69). No local decrease in the centreline WFASI profile is observed within the section of increased running roughness. In addition, Figure

6-10 presents a section of track where significant R-values are calculated for both surface running roughness profiles and the centreline WFASI dataset (-0.75 for the left rail and -0.72 for the right rail). In this section of interest, the cross correlation of either shoulder WFASI profile with either surface running roughness dataset does not yield a significant R-value. In contrast, Figure 6-11 presents a third example, representative of the majority of the sections of interest, where no combination of surface running roughness and WFASI dataset yields a significant R-value.

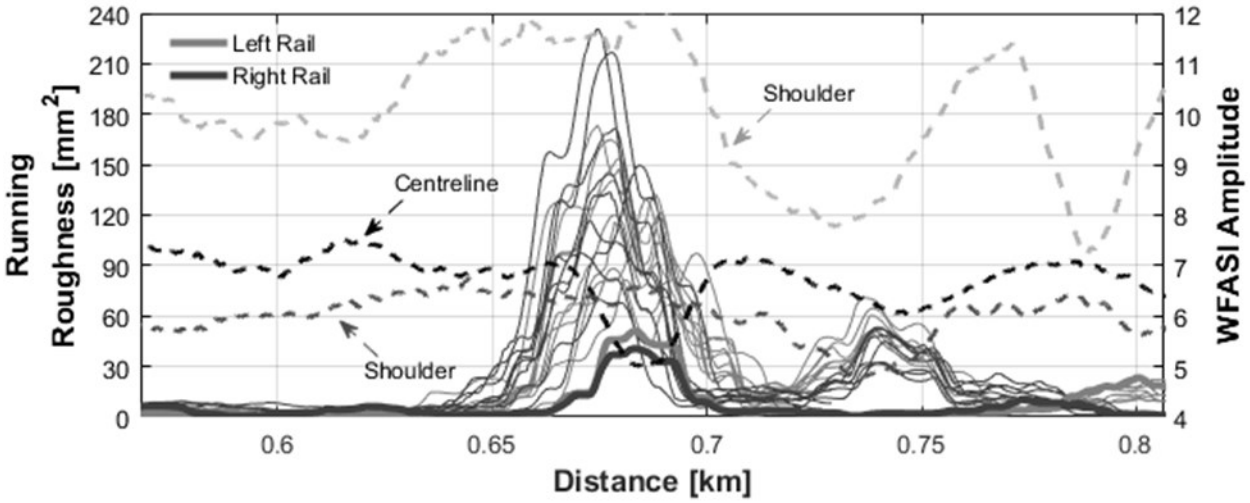

Figure 6-10. A second local comparison of the two surface running roughness (solid) profiles and the three WFASI (dashed) profiles. Significant R values (-0.75 and -0.72) are derived from the cross-correlation of the most recent left and right rail running roughness profiles with the centreline WFASI dataset. In this local section, no significant R values are calculated when considering either shoulder WFASI dataset.

A number of important observations can be drawn from Tables 6-1 and 6-2 as well as Figures 6-9, 6-10, and 6-11. First, significant R-values are not always associated with the ballast degradation estimates derived from a specific GPR antenna. In a small number sections, significant R-values are associated with a combination of WFASI datasets (shoulder and shoulder or shoulder and centreline etc.). For the majority of track sections yielding significant

R-values, these R-values are associated with a single GPR dataset only. There is no systematic pattern to which GPR antenna yields ballast degradation estimates that successfully correlate with the observed track geometry.

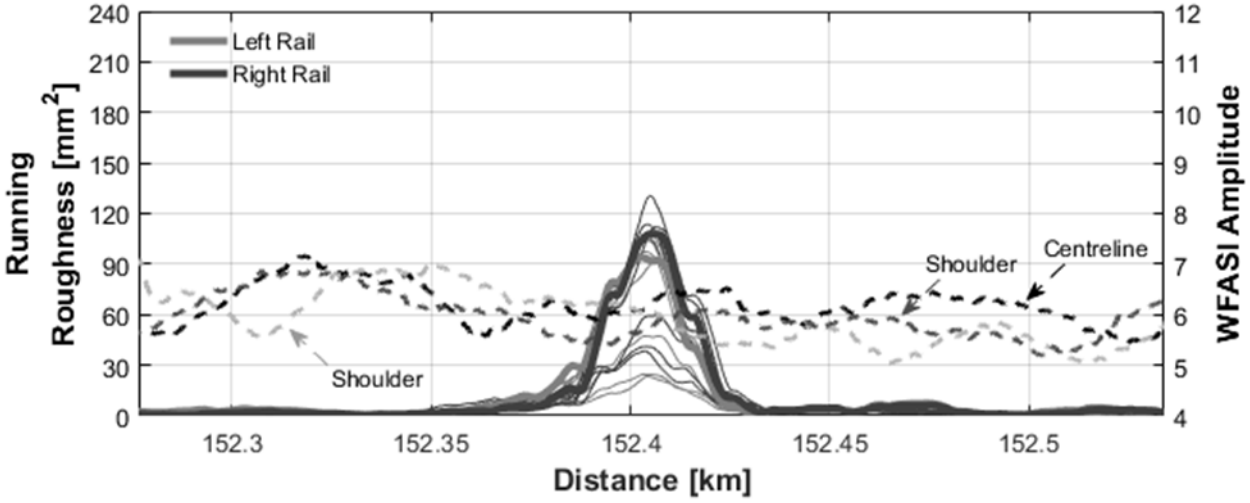

Figure 6-11. A third local comparison of the two surface running roughness (solid) profiles and the three WFASI (dashed) profiles. In this local section, no significant correlation coefficients are observed for any combination of running roughness and WFASI datasets.

Secondly, individual WFASI amplitudes cannot be related to specific amounts of fines within the ballast void space. In Figure 6-9, the local decrease in shoulder WFASI amplitude from 11 to 8 is interpreted as being indicative of degraded ballast in the middle of the section. Concurrently, the decrease in centreline WFASI amplitude in Figure 6-10 from 7 to 5 is also interpreted as being indicative of degraded ballast. Depending on the individual section of interest under analysis, the WFASI amplitudes that are indicative of degraded ballast are different. This difference in WFASI amplitudes is likely the result of other variable track foundation conditions between the track sections (Scanlan et al. 2017b). Ballast samples or test-pits would be required in each local section of interest in order to calibrate and standardize the WFASI amplitudes. However, invasive ground-truthing programs are not part of the standard industry approach when analyzing

low-frequency GPR datasets. In absence of ballast samples available for calibration, only the relative changes in WFASI amplitudes in each local section can be used to infer the presence of degraded ballast.

Finally, a large majority of the identified local sections of interest do not yield significant R-values (Tables 6-1 and 6-2, Figure 6-11). While it may be that possible that a significant spatial associations between ballast degradation and track alignment and surface roughness are rare, such a result would be significantly contrary to expectations (Selig and Waters 1994, Sadeghi and Askarinejad 2009, Sussmann et al. 2012, Li et al. 2016, Scanlan et al. 2017a). As such, mitigating factors must be influencing the correlation results.

Scanlan et al. (2017a) observed that the relationship between relatively degraded ballast and increased track geometry variability is less prominent in areas of soft, organic subgrades. While, organic subgrades underlie portions of the subdivision analyzed, they are not distributed widely enough to account for the approximately 92% of alignment sections of interest and 86% of surface sections of interest that yield no significant correlation coefficients (Alberta Agriculture and Forestry 2012).

The small proportion of local-scale sections of interest exhibiting significant R-values is likely related to ambiguous WFASI amplitudes (Figure 6-4). Without representative ballast samples for calibration, every variation in the windowed Fourier amplitude spectral integral is assumed to be the result of ballast degradation. This analysis attempts to compensate for a portion of these effects through small-scale, local analyses and the assumption that the local variability in the track foundation will be less than what is observed across the full subdivision. While there are instances of successful local-scale correlation between increasing track roughness and GPR-inferred ballast degradation (Tables 6-1 and 6-2 as well as Figures 6-9 and 6-10), it is likely that

variations in the track foundation conditions are still not being fully constrained in each local section of interest. To improve the correlation results, standard GPR data interpretations could be supplemented with additional subsurface investigations to ensure that ballast degradation is the main factor affecting the backscattered GPR signal.

Another potential improvement is the consideration of additional GPR datasets. At higher signal frequencies (>1 GHz), ballast degradation can be estimated from GPR measurements based on changes in scattering behaviour as individual air voids fill with fines (Al-Qadi et al. 2008, Al-Qadi et al. 2010, Shangguan and Al-Qadi 2014). Combined with the change to signal attenuation, a combination of low- and high-frequency GPR measurements may provide a more reliable estimate for the distribution of fines within the ballast. A more reliable GPR interpretation may then result in a stronger spatial correlation between ballast degradation and the observed trends in track geometry then what is observed based on an interpretation of 400 MHz GPR measurements only. Additionally, repeating the GPR measurements at various points throughout the year may aid in highlighting common features in the results and further reducing ambiguity in the ballast degradation estimates. Time-lapse GPR measurements have been previously used to identify sections of Finish railways thought to be susceptible to frost action (Silvast et al. 2013).

The results of this analysis demonstrate that, based on current industry practices, GPR-derived estimates of ballast degradation may be insightful in local sections of track exhibiting *both* low relative WFASI amplitudes and increased track roughness. The potential to perform low-frequency GPR measurements and have them accurately and reliably characterize the current ballast degradation conditions without any additional constraints though, has yet to be fully realized. However, low-frequency GPR remains a useful tool in railway foundation studies. For

example, the structural information derived from GPR measurements can be used to provide critical insight into the conditions within railway embankments including layer thicknesses and uniformity (Hugenschmidt 2000, Fernandes et al. 2008) as well as the identification ballast pockets and entrapped moisture (Sussmann et al. 2003). Continued research is suggested to improve the reliability of GPR-based ballast degradation estimates.

6.9. Conclusions

Repeated track geometry surveys collected over a span of 15 months between May 2011 and August 2012 for a 335 km-long heavy-haul subdivision in Western Canada have been used to evaluate the spatial association between ballast degradation, as estimated from 400 MHz GPR measurements, and track geometry variability. Variability in both the left and right rail track alignment and surface variables was represented as a running roughness using a 20 m averaging length. An established attribute is used to estimate the relative amount of fines within the ballast void space for three sets of GPR measurements collected in August 2012. As is the standard industry practice, no ballast samples were collected during GPR data acquisition. Individual GPR measurements were made at 0.2 m increments over both ballast shoulders as well as the track centreline. A 20 m-long running average filter was also used to smooth the GPR-based ballast degradation estimates.

The strength of the spatial association between the running roughness and the GPR-based estimates of ballast degradation was quantified using Pearson's correlation coefficient and the spatial correlation was investigated at both the subdivision and local scales. The results of this analysis revealed that, considering the full dataset, there was no subdivision-scale spatial association between locations of rougher track and increased degradation of the ballast. However, this result did not preclude the possibility of local-scale spatial associations.

The need to perform local scale analyses was in recognition of the GPR-based estimates of ballast degradation being highly sensitive to local conditions in the track foundation unrelated to ballast degradation (ballast thickness, subballast material, etc.). Reducing the spatial scale of the analysis, constrained a portion of the variability in these additional factors. Local sections of interest were defined to be those containing either sustained or increasing track roughness in the 15 months prior to GPR data collection (May 2011 - August 2012). In total 51, 41, 369, and 369 local sections of interest were identified from the repeated left and right rail alignment and surface measurements and encompassed a combined 12.3, 10.0, 91.2, and 90.8 km of track, respectively. More local sections of interest were identified from the track surface measurements than for the track alignment as the track surface running roughness amplitudes were generally larger.

A cross correlation of track roughness and the GPR-based estimate of ballast degradation yielded significant correlation coefficients ($\leq$ -0.5) for only 8 and 14% of the local sections of interest for track alignment and surface, respectively. The increased proportion of significant correlations ($\leq$ -0.5) when considering track surface was attributed to degraded ballast conditions being the dominant factor in the development of track roughness; whereas the variability in track alignment measurements is also strongly dependent on tie conditions. The overall absence of significant spatial correlations between track roughness and the GPR-based estimates of ballast degradation was interpreted as the result of continued local-scale variability in the non-degradation related track foundation conditions. This continued variability leads to GPR-based ballast degradation estimates that do not correspond to actual conditions.

Improved approaches to the correlation of ballast degradation and observed track roughness may involve either the collection of ground-truth samples to calibrate the GPR measurements or the

use of multiple GPR measurements. Joint low- and high-frequency GPR interpretations may yield a more reliable ballast degradation estimate due to differences in how ballast degradation affects GPR measurements at different signal frequencies, while repeated GPR measurements at the same signal frequency may aid in identifying consistent features across multiple seasons. Even with the identified difficulties in inferring ballast degradation from low-frequency measurements, GPR remains a useful tool in the non-destructive study of railway foundations.

6.10. Acknowledgments

The authors thank both Canadian National Railway and Canadian Pacific Railway for their support and facilitation of this project. This research was made possible through the Canadian Rail Research Laboratory (CaRRL) (www.carrl.ca), which is funded by the Natural Sciences and Engineering Research Council of Canada, Canadian Pacific Railway, Canadian National Railway, the Association of American Railroads – Transportation Technology Centre Inc., the National Research Council of Canada, Transport Canada, and Alberta Innovates – Technology Futures.

6.11. References

Alberta Agriculture and Forestry. 2012. Alberta soil information viewer [online]. Available from http://www4.agric.gov.ab.ca/agrasidviewer/ [cited 03/16 2016].

Al-Qadi, I.L., Xie, W., and Roberts, R. 2008. Scattering analysis of ground-penetrating radar data to quantify railroad ballast contamination, NDT&E International, **41**(6): 441-447.

Al-Qadi, I.L., Xie, W., Jones, D.L., and Roberts, R. 2010. Development of a time-frequency approach to quantify railroad ballast fouling condition using ultra-wide band ground-penetrating radar data, International Journal of Pavement Engineering, **11**(4): 269-279.

Andrews, J. 2012. A modelling approach to railway track asset management, Proceedings of the Institution of Mechanical Engineers, Part F: Journal of Rail and Rapid Transit, **227**(1): 56-73.

Audley, M. and Andrews, J.D. 2013. The effects of tamping on railway track geometry degradation, Proceedings of the Institution of Mechanical Engineers, Part F: Journal of Rail and Rapid Transit, **227**(4): 376-391.

Berawi, A.R.B., Delgado, R., Calçada, R., and Vale, C. 2010. Evaluating track geometrical quality through different methodologies, International Journal of Technology, **1**: 38-47.

Carpenter, D., Jackson, P.W., and Jay, A. 2004. Enhancement of the GPR method of railway trackbed investigation by the installation of radar detectable geosynthetics, NDT&E International, **37**(2): 95-103.

Clark, M.R., Gordon, R., Kemp, T., and Forde, M.C. 2001. Electromagnetic properties of railway ballast, NDT&E International, **34**(5): 305-311.

De Chiara, F., Fontul, S., and Fortunato, E. 2014. GPR laboratory tests for railway materials dielectric properties assessment, Remote Sensing, **2014**(6): 9712-9728.

Ebersöhn, W. and Selig, E.T. 1994. Use of track geometry measurements for maintenance planning, Transportation Research Record, **1470**.

El-Sibaie, M. and Zhang, Y. 2004. Objective track quality indices, Transportation Research Record, **1863**: 81-87.

Federal Railroad Administration. 2014. Track and rail and infrastructure integrity compliance manual. Federal Railroad Administration, Washington DC, USA.

Fernandes, F.M., Pereira, M., Gomes Correia, A., Lourenco, P.B., and Caldeira, L. 2008. Assessment of layer thickness and uniformity in railway embankments with ground

penetrating radar. In Advances in Transportation Geotechnics Edited by E. Ellis, H. Yu, G. McDowell, A.R. Dawson and N. Thom. Taylor and Francis Group, London, United Kingdom, pp. 571-575.

Gallagher, G.P., Leiper, Q., Williamson, R., Clark, M.R., and Forde, M.C. 1999. The application of time domain ground penetrating radar to evaluate railway track ballast, NDT&E International, **32**(8): 463-468.

Government of Canada. November 18 2015. Historical climate data [online]. Available from http://climate.weather.gc.ca/ [cited 05/05 2015].

Huang, H., Tutumluer, E., and Dombrow, W. 2009. Laboratory characterization of fouled railroad ballast behavior, Transportation Research Record, **2117**: 93-101.

Hugenschmidt, J. 2000. Railway track inspection using GPR, Journal of Applied Geophysics, **43**(2): 147-155.

Indraratna, B., Tennakoon, N., Nimbalkar, S., and Rujikiatkamjorn, C. 2013. Behaviour of clay-fouled ballast under drained triaxial testing, Géotechnique, **63**(5): 410-419.

Jol, H. 2009. Ground penetrating radar theory and applications. Elsevier Science, Oxford, United Kingdom.

Khakiev, Z., Shapovalov, V., Kruglikov, A., Morozov, A., and Yavna, V. 2014. Investigation of long term moisture changes in trackbeds using GPR, Journal of Applied Geophysics, **110**: 1-4.

Li, D., Hyslip, J.P., Sussmann, T.R., and Chrismer, S.M. 2016. Railway geotechnics. Taylor & Francis Group LLC, Boca Raton, FL, USA.

Olhoeft, G.R. 2005. Working in a difficult environment: GPR sensing on the railroads. In IEEE Antennas and Propagation Society International Symposium, Washington DC, USA, Vol. 3B, pp. 108-111.

Parsons, R.L., Rahman, A.J., Han, J., and Glavinivh, T.E. 2014. Track ballast fouling and permeability characterization by using resistivity, Transportation Research Record, **2448**: 133-141.

Sadeghi, J. 2010. Development of railway track geometry indexes based on statistical distribution of geometry data, Journal of Transportation Engineering, **136**(8): 693-700.

Sadeghi, J. and Askarinejad, H. 2011. Development of track condition assessment model based on visual inspection, Structure and Infrastructure Engineering: Maintenance, Management, Life-Cycle Design and Performance, **7**: 895-905.

Sadeghi, J. and Askarinejad, H. 2010. Development of improved railway track degradation models, Structure and Infrastructure Engineering: Maintenance, Management, Life-Cycle Design and Performance, **6**: 675-688.

Sadeghi, J. and Askarinejad, H. 2009. An investigation into the effects of track structural conditions on railway track geometry deviations, Proceedings of the Institution of Mechanical Engineers, Part F: Journal of Rail and Rapid Transit, **233**: 415-425.

Scanlan, K.M., Hendry, M.T., and Martin, C.D. 2017a. Evaluating the impact of ballast undercutting on the roughness of rack geometry over different subgrade conditions, Proceedings of the Institution of Mechanical Engineers, Part F: Journal of Rail and Rapid Transit, 1-11: DOI: 10.1177/0954409717720347.

Scanlan, K.M., Hendry, M.T., Martin, C.D., and Schmitt, D.R. 2017b. Evaluating the sensitivity of low-frequency ground-penetrating radar attributes to estimate ballast fines in the

presence of variable track foundations through simulation, Proceedings of the Institution of Mechanical Engineers, Part F: Journal of Rail and Rapid Transit, 1-14: DOI: 10.1177-0954409717710408.

Selig, E.T. and Waters, J.M. 1994. Track geotechnology and substructure management. Thomas Telford Ltd., London.

Shangguan, P. and Al-Qadi, I.L. 2014. Content-based image retrieval approaches to interpret ground penetrating radar data, Construction and Building Materials, **69**: 10-17.

Silvast, M., Nurmikolu, A., Wiljanen, B., and Levomaki, M. 2013. Identifying frost-susceptible areas on Finnish railways using the ground penetrating radar technique, Proceedings of the Institution of Mechanical Engineers, Part F: Journal of Rail and Rapid Transit, **227**(1): 3-9.

Silvast, M., Nurmikolu, A., Wiljanen, B., and Levomaki, M. 2010. An inspection of railway ballast quality using ground penetrating radar in finland, Proceedings of the Institution of Mechanical Engineers, Part F: Journal of Rail and Rapid Transit, **224**: 345-351.

Silvast, M., Levomaki, M., Nurmikolu, A., and Noukka, J. 2006. NDT techniques in railway structure analysis. In Proceedings of the 7th World Congress on Railway Research, Montreal, Canada, pp. 1-12.

Sussmann, T.R., Ruel, M., and Chrismer, S.M. 2012. Source of ballast fouling and influence considerations for condition assessment criteria, Transportation Research Record, **2289**: 87-94.

Sussmann, T.R., Selig, E.T., and Hyslip, J.P. 2003. Railway track condition indicators from ground penetrating radar, NDT&E International, **36**(3): 157-167.

Tennakoon, N. and Indraratna, B. 2014. Behaviour of clay-fouled ballast under cyclic loading, Géotechnique, **64**(6): 502-506.

Transport Canada. 2012. Rules respecting track safety. Canada, Ottawa.

Chapter 7: Conclusions & Recommendations

The purpose of this research was twofold; first, to continue the development of ground-penetrating radar (GPR) as a large-scale, non-destructive ballast degradation detection tool and second, to provide greater quantitative insight into the effects of ballast degradation on observed trends in track geometry for an operational heavy-haul railway. The correlation between ballast degradation and trends in track geometry was investigated through the analysis of both historical ballast maintenance records and GPR measurements. Motivation for this research comes from the need for the railway industry to develop an efficient degraded ballast detection tool that can be applied over extensive lengths of track and to demonstrate, through field observations, that degraded ballast does exert a significant effect on long-term trends in track geometry.

The following four sections summarize the conclusions corresponding to each of the research objectives stated in Chapter 1.

7.1. Review and Synthesis of the Relevant Literature regarding GPR as Applied to Ballast Degradation Studies

Chapter 3 presented a detailed review of how GPR has been developed as an efficient ballast degradation detection tool beginning from the fundamental physical phenomena. A theoretical basis for ballast degradation manifesting changes in backscattered low- and high-frequency GPR signals was demonstrated and existing methods to either qualitatively or quantitatively describe these changes were presented. Low-frequency (<1 GHz) GPR attributes were related to ballast degradation through the GPR propagation velocity, signal attenuation, and ballast-subballast reflection strengths. These attributes were straightforward to calculate but potentially susceptible to errors should other conditions in the track foundation (which are not ballast degradation

related) alter the measured GPR signal in a similar manner. For high-frequency (>1 GHz) GPR measurements, the accumulation of fines reduced the normalized dimension of the air void scatterers within the ballast. This resulted in clear, visible changes in both the high-frequency GPR signal scattering behaviour and instantaneous signal attenuation. Methods established to describe these changes were also presented. A potential drawback of high-frequency methods was limited signal penetration into the ballast due to frequency-dependent attenuation rates and therefore little additional information on the deeper layers of track foundation. Ultimately, it was proposed that the most reliable GPR-based approach to the quantification of ballast degradation may be a combination of low- and high-frequency methods; thereby combining the advantages each individual data type.

7.2. Validating Ballast Degradation as a Dominant Factor Affecting Trends in Track Geometry

Chapter 4 presented a quantification of the observed trends in track geometry after ballast degradation conditions had known to have been improved by ballast renewal (undercutting). The data used in this analysis came from 6.90 km of undercut track (undercuttings performed in 2010 and 2011) and five years of track geometry records (2010 through 2015). The undercut track was first subdivided into 115 60 m-long segments in order to standardize the analysis. Within each segment, the standard deviation of the track crosslevel, alignment, and surface were derived from each track geometry survey in order to visualize the long term trends in variability (roughness). Each trend in track geometry (345 in total) was then assigned one of four classifications based on the relative change in track roughness before and after ballast renewal.

The distribution of trend classification types considering all 115 segments revealed that upwards of 60% of the track (4.14 km) exhibited sustained (lasting through the three-to-four year

observation period) improvements in track roughness after ballast renewal. This result was consistent between the three track geometry variables investigated and field demonstration of ballast degradation being an important factor contributing to increased track geometry variability but not uniquely dominant. For the remaining 40% of the track (2.76 km) sustained, long-term improvements in track roughness after ballast renewal were not observed. In these segments, the track geometry exhibited either only a temporary reduction in roughness, no effect of ballast renewal, or long-term increases in roughness after ballast renewal. In this 2.76 km of track, other factors besides ballast degradation were exerting significant influence on track geometry and were not being effectively addressed by ballast renewal.

To demonstrate the role of subgrade type on the effects a change in ballast degradation conditions has on long-term trends in track roughness, the subgrade material underlying each segment was determined from a soil map. Subgrades were classified as either a stiff, mineral-based subgrade (sand, silt, clay, or till) or as a soft, organic subgrade (peat) based on the most prominent soil type in the area. Three segments (0.18 km) exceeded the coverage of the soil map and subgrade conditions could not be accurately determined. For track constructed on mineral-based subgrades (5.22 km of track), long-term improvements were observed in 69% of the track segments. For organic subgrades (1.50 km of track), only 36% of the segments exhibited long-term improvements in roughness. These results were indicative of ballast degradation exerting a greater influence on the long-term trends in track geometry for track constructed on mineral-based subgrades. For sections of track constructed on soft organic subgrades, the contribution from ballast degradation on the trends in track roughness was reduced, with 64% of the segments showing no long-term improvements in track geometry variability after ballast renewal.

7.3. The Sensitivity of Ballast Degradation Estimates in the Presence of Variable Track Foundations

Chapter 5 presented a detailed analysis of the effects unknown ballast thicknesses, saturations, conductivities, and subballast materials had on the ability to reliably infer the amount of fines within ballast using 400 MHz GPR measurements. The synthetic data used in this analysis were generated from 819 simulated GPR measurements of a two-layer (ballast overlying subballast) track foundation. Various proportions of aggregate, air, moisture, and fines volume fractions were combined through the Bruggemann-Hanai-Sen mixing model to derive the ballast's bulk relative dielectric permittivity. Changes in the ballast thickness were implemented by changing the size of the ballast layer within the modelled track foundation. The relative dielectric permittivities and electrical conductivities of the subballast were determined from existing literature values for three granular materials (sand, soil, and clay).

Three different GPR attributes that had been demonstrated in the literature as being representative of ballast degradation were calculated from the synthetic GPR measurements generated by each simulation. Each attribute returned ambiguous estimates for the volumetric amount of fines within the ballast as the ballast saturation was varied. This was a direct consequence of a non-unique bulk ballast relative dielectric permittivity (for a specific amount of fines) when moisture levels were allowed to fluctuate. The GPR propagation velocity-based attribute was not affected by changes in ballast thickness or subballast material type. Under the same conditions the attenuation-based and the ballast-subballast refection strength-based attributes were both unable to relate specific attribute amplitudes to a volumetric amount of fines. The ambiguity in these two attributes was the result of variations in ballast thickness and

subballast material type manifesting the same changes on the simulated GPR measurements as ballast degradation.

In terms of their use with real GPR measurements of an operational railway foundation, the attenuation- and reflection strength-based attributes were determined to be more easily applicable as they did not require additional information to be calculated. The propagation velocity attribute required that the ballast thickness already be known in order to be calculated. However, the results of this analysis clearly demonstrated that in order to derive reliable estimates for the amount of fines within ballast from any 400 MHz GPR measurements, variations in ballast thickness, saturation, conductivity, and subballast material type must be somehow constrained.

7.4. The Spatial Association between Rough Track and GPR-Inferred Ballast Degradation

Chapter 6 presented an investigation into quantifying the spatial association between sections of rough track and the presence of degraded ballast as inferred from 400 MHz GPR measurements. Repeated track geometry survey data for a 335 km-long mainline subdivision was used in this analysis and the datasets were collected over the course of 15 months (May 2011 - August 2012). The variability in the alignment and surface track geometry was quantified as a running roughness. Three 400 MHz GPR datasets were collected using a high-rail in August 2012; one along the track centreline and two over the ballast shoulders. Relative ballast degradation was inferred from the GPR datasets using the signal attenuation-based attribute investigated in Chapter 5.

No universal, subdivision-scale spatial association between inferred ballast degradation and the most contemporaneous track roughness measurements was observed when cross correlating any

combination of the two data types (shoulder or centreline GPR attribute profiles and left or right rail alignment or surface running roughness). Restricting the full datasets to the track positions that either exhibited the smallest GPR attribute amplitudes (indicative of more relatively degraded ballast) or the roughest track also had no effect on the distribution of the complementary variable. For example, the distribution of track roughness amplitudes did not shift to higher values when the dataset was restricted to only those track positions that exhibited the smallest GPR attribute amplitudes as would have been expected if a large-scale spatial association existed.

A three-step process was developed to identify local sections of track that exhibited sustained or increased trends in track roughness over the 15 months prior to GPR data collection. Local-scale spatial correlations were investigated in an attempt to constrain a portion of the variability in the track foundation identified in Chapter 5 as leading to ambiguities in the GPR-inferred ballast degradation estimates. Correlation coefficients less than or equal to -0.5 were observed in only 8 and 14% of the local alignment and surface sections, respectively. Negative correlation coefficients were expected based on the hypothesis of increasing track roughness being associated with decreasing GPR attribute amplitudes in the presence of degraded ballast. Significant correlations commonly occurred between a single GPR antenna and track roughness and systematic pattern to which dataset the track roughness correlated with was not observed. The scarcity of significant local-scale correlations was attributed to continued ambiguity in the GPR attribute amplitudes.

7.5. Implications of this Study

A main contribution of this research to the railway engineering industry is the observation that a change ballast degradation conditions is an important, but not uniquely dominant, factor

contributing to long-term trends in track geometry on a subdivision scale. The procedures Canadian railway operators currently have in place to identify sections of track that, from a track geometry perspective, would benefit from ballast renewal are only successful in approximately 60% of cases. For the remaining 40%, long-term improvements in track geometry variability following ballast maintenance are not observed. However, supplementing the current ballast maintenance decision-making process with additional datasets, such as soil maps, may help to reduce the proportion of ballast renewal maintenance operations that do not achieve the desired goal of long-term improvements in track geometry.

A second major contribution of this research is the illustration that based on current standard industry practices; ballast degradation estimates from 400 MHz GPR measurements are not yet reliable enough to be used as the sole indicator for the need to perform ballast maintenance. Quantitative interpretation of 400 MHz GPR datasets is not straightforward as other conditions in the track foundation can mimic the effects of degraded ballast. Ambiguity in GPR data, or non-uniqueness, is a well understood phenomenon in geophysics and this work demonstrates that it is also an important factor to consider when inferring ballast degradation from rail-borne GPR measurements. While low-frequency GPR measurements have been shown to provide useful insights into processes at work within track foundations through structural analyses and should therefore not be immediately disregarded; additional research would be required to fully develop its robustness as a degraded ballast detection tool.

7.6. Recommendations

The research presented in this thesis enhances the understanding of the role ballast has in the long-term development of track roughness and the ability to detect degraded ballast using GPR.

The following tasks are recommended to further develop GPR as a reliable ballast degradation tool:

- Improving GPR-based ballast degradation estimates by combining low- and high-frequency measurements. This research focused primarily on inferring ballast degradation from 400 MHz GPR measurements, as this was the desired field dataset to be analyzed, and the results showed that standard interpretation strategies can yield highly ambiguous results. Ballast degradation manifests differently depending on GPR signal frequency and a joint interpretation of a low- and high-frequency dataset may yield an improved ballast degradation estimate. A more reliable ballast degradation estimate may then also lead to a more consistent spatial correlation with track roughness.

  To this end, new joint low- and high-frequency GPR interpretation methodologies could be developed based on detailed laboratory testing of full-scale ballast models. These interpretation techniques could then be deployed as part of limited-scale field trials to investigate their robustness in real and variable track foundations before attempting a full subdivision scale deployment.
- Improving the reliability of ballast degradation estimates derived from low-frequency GPR measurements through repeated measurements. This research is based on a single set of GPR measurements for the railway subdivision being investigated. Repeated GPR measurements of the same railway at various times through the year will produce data collected under various moisture conditions while ballast thickness, degradation, and subballast material type can be expected to remain relatively consistent over short timespans. Repeated measurements may help characterize the influence of variable ballast saturations and seasonal effects on the ballast degradation estimates derived from

GPR measurements. This work could also be combined with sampling to develop attribute calibration curves for various track foundation conditions. The assumption of a consistent ballast thickness and degradation level will have to be validated against track maintenance records and samples.

- Developing an additional quantitative high-frequency attribute related to the presence of degraded ballast. Based on the review of existing high-frequency GPR data interpretation methods, an approach to estimating ballast degradation based on quantifying the resulting increase in signal attenuation has yet to be developed. Strategies to estimate GPR signal attenuation from a single trace containing multiple reflections have been developed in other GPR applications (for example, inverse Q filtering). A similar approach may be applicable to high-frequency ballast measurements and yield a quantitative attenuation estimate that can be calibrated to a specific amount of fines within the ballast. Such an interpretation strategy would only be applicable to high-frequency GPR measurements as it requires high reflection densities along an individual trace; a condition that is not met in low-frequency GPR datasets.

References

Al-Qadi, I.L., Xie, W., and Roberts, R. 2010a. Optimization of antenna configuration in multiple-frequency ground penetrating radar system for railroad substructure assessment, NDT&E International, **43**(1): 20-28.

Al-Qadi, I.L., Xie, W., and Roberts, R. 2008a. Scattering analysis of ground-penetrating radar data to quantify railroad ballast contamination, NDT&E International, **41**(6): 441-447.

Al-Qadi, I.L., Xie, W., and Roberts, R. 2008b. Time-frequency approach for ground penetrating radar data analysis to assess railroad ballast condition, Research in Nondestructive Evaluation, **19**: 219-237.

Al-Qadi, I.L., Xie, W., Jones, D.L., and Roberts, R. 2010b. Development of a time-frequency approach to quantify railroad ballast fouling condition using ultra-wide band ground-penetrating radar data, International Journal of Pavement Engineering, **11**(4): 269-279.

Al-Qadi, I.L., Xie, W., Roberts, R., and Leng, Z. 2010c. Data analysis techniques for GPR used for assessing railroad ballast in high radio-frequency environment, Journal of Transportation Engineering, **136**(4): 392-399.

Alberta Agriculture and Forestry. 2012. Alberta soil information viewer [online]. Available from http://www4.agric.gov.ab.ca/agrasidviewer/ [cited 03/16 2016].

Anbazhagan, P., Su, L., Buddhima, I., and Cholachat, R. 2011. Model track studies on fouled ballast using ground penetrating radar and multichannel analysis of surface wave, Journal of Applied Geophysics, **74**: 175-184.

Annan, A.P. 2008. Ground penetrating radar principles, procedures & applications. Sensors & Software Inc., Mississauga, Ontario, Canada.

Andrews, J. 2012. A modelling approach to railway track asset management, Proceedings of the Institution of Mechanical Engineers, Part F: Journal of Rail and Rapid Transit, **227**(1): 56-73.

Andrews, J., Prescott, D., and De Rozières, F. 2014. A stochastic model for railway track asset management, Reliability Engineering and System Safety, **130**: 76-84.

AREMA. 2012. Manual for railway engineering. American Railway Engineering and Maintenance of Way Association, Lanham, MD, USA.

Audley, M. and Andrews, J.D. 2013. The effects of tamping on railway track geometry degradation, Proceedings of the Institution of Mechanical Engineers, Part F: Journal of Rail and Rapid Transit, **227**(4): 376-391.

Bano, M. 2004. Modelling of GPR waves for lossy media obeying a complex power law of frequency for dielectric permittivity, Geophysical Prospecting, **52**: 11-26.

Benedetto, A. and Pajewski, L. 2015. Civil engineering applications of ground penetrating radar. Springer International Publishing, Switzerland.

Benedetto, A. and Pensa, S. 2007. Indirect diagnosis of pavement structural damages using surface GPR reflection techniques, Journal of Applied Geophysics, **62**: 107-123.

Benedetto, A., Tosti, F., Bianchini Ciampoli, L., Pajewski, L., Pirrone, D., Umiliaco, A., and Brancadoro, M.G. 2016. A simulation-based approach for railway applications using GPR. In The Proceedings of the 2016 16th International Conference of Ground Penetrating Radar (GPR), Hong Kong, pp. 1-6.

Berawi, A.R.B., Delgado, R., Calçada, R., and Vale, C. 2010. Evaluating track geometrical quality through different methodologies, International Journal of Technology, **1**: 38-47.

Bradford, J.H. and Deeds, J.C. 2006. Ground-penetrating radar theory and application of thin-bed offset-dependent reflectivity, Geophysics, **71**(3): K47-K57.

Brough, M., Stirling, A., Ghataora, G., and Madelin, K. 2003. Evaluation of railway trackbed and formation: A case study, NDT&E International, **36**: 145-156.

Cai, J.Q., Liu, S.X., Fu, L., and Feng, Y.Q. 2016. Detection of railway subgrade moisture content by GPR. In 16th International Conference on Ground Penetrating Radar (GPR), pp. 1-5.

Canadian National. 2014. 2013 annual report. Canadian National Railway Company, Montreal QC.

Carpenter, D., Jackson, P.W., and Jay, A. 2004. Enhancement of the GPR method of railway trackbed investigation by the installation of radar detectable geosynthetics, NDT&E International, **37**(2): 95-103.

Chopra, S. and Marfurt, K.J. 2005. Seismic attributes - A historical perspective, Geophysics, **70**(5): 3SO-28SO.

Clark, M.R., Gordon, R., Kemp, T., and Forde, M.C. 2001. Electromagnetic properties of railway ballast, NDT&E International, **34**(5): 305-311.

Clark, R. 2004. Rail flaw detection: Overview and needs for future developments, NDT&E International, **37**: 111-118.

De Chiara, F., Fontul, S., and Fortunato, E. 2014. GPR laboratory tests for railway materials dielectric properties assessment, Remote Sensing, **2014**(6): 9712-9728.

De Bold, R., O'Connor, G., Morrissey, J.P., and Forde, M.C. 2015. Benchmarking large scale GPR experiments on railway ballast, Construction and Building Materials, 92: 31-42.

Ebersöhn, W. and Selig, E.T. 1994. Use of track geometry measurements for maintenance planning, Transportation Research Record, **1470**.

El-Sibaie, M. and Zhang, Y. 2004. Objective track quality indices, Transportation Research Record, **1863**: 81-87.

Federal Railroad Administration. 2014. Track and rail and infrastructure integrity compliance manual. Federal Railroad Administration, Washington DC, USA.

Federal Railroad Administration. 2011. Heavy axle load revenue service mud-fouled ballast investigation. RR11-10, Federal Railroad Administration, Washington DC, USA.

Feldman, F. and Nissen, D. 2002. Alternative testing method for the measurement of ballast fouling: Percentage void contamination. In Proceedings of the Conference on Railway Engineering, Wollongong, Australia, pp. 101-109.

Fenton, M.M., Waters, E.J., Pawley, S.M., Atkinson, N., Utting, D.J., and Mckay, K. 2013. Surficial geology of Alberta. Alberta Energy Regulator, Edmonton, AB, Canada.

Fernandes, F.M., Pereira, M., Gomes Correia, A., Lourenco, P.B., and Caldeira, L. 2008. Assessment of layer thickness and uniformity in railway embankments with ground penetrating radar. In Advances in Transportation Geotechnics Edited by E. Ellis, H. Yu, G. McDowell, A.R. Dawson and N. Thom. Taylor and Francis Group, London, United Kingdom, pp. 571-575.

Gallagher, G.P., Leiper, Q., Williamson, R., Clark, M.R., and Forde, M.C. 1999. The application of time domain ground penetrating radar to evaluate railway track ballast, NDT&E International, **32**(8): 463-468.

Giannakis, I., Giannopoulos, A., and Warren, C. 2016. A realistic FDTD numerical modeling framework of ground penetrating radar for landmine detection, IEEE Journal of Selected Topics in Applied Earth Observations and Remote Sensing, **9**(1): 37-51.

Government of Canada. November 18 2015. Historical climate data [online]. Available from http://climate.weather.gc.ca/ [cited 05/05 2015].

Haji Adbulrazagh, P. and Hendry, M.T. 2016. Case study of use of falling weight deflectometer to investigate railway infrastructure constructed upon soft subgrades, Canadian Geotechnical Journal, **53**(12): 1991-2000.

Huang, H., Tutumluer, E., and Dombrow, W. 2009. Laboratory characterization of fouled railroad ballast behavior, Transportation Research Record, **2117**: 93-101.

Hubbard, S.S., Zhang, J., Monteiro, P.J.M., Peterson, J.E., and Rubin, Y. 2003. Experimental detection of reinforcing bar corrosion using nondestructive geophysical techniques, ACI Materials Journal, **6**: 501-510.

Hugenschmidt, J. 2000. Railway track inspection using GPR, Journal of Applied Geophysics, **43**(2): 147-155.

Hugenschmidt, J. and Kalogeropoulos, A. 2009. The inspection of retaining walls using GPR, Journal of Applied Geophysics, **67**: 335-344.

Hyslip, J.P. 2002. Fractal analysis of geometry data for railway track condition assessment. PhD, University of Massachusetts Amherst, ProQuest Dissertations and Theses.

Indraratna, B., Salim, W., and Rujikiatkamjorn, C. 2011a. Advanced rail geotechnology - ballasted track. Taylor and Francis Group LLC, London UK.

Indraratna, B., Su, L., and Rujikiatkamjorn, C. 2011b. A new parameter for classification and evaluation of railway ballast fouling, Canadian Geotechnical Journal, **48**: 322-326.

Indraratna, B., Vinod, J.S., and Lackenby, J. 2009. Influence of particle breakage on the resilient modulus of railway ballast, Géotechnique, **59**(7): 643-646.

Indraratna, B., Tennakoon, N., Nimbalkar, S., and Rujikiatkamjorn, C. 2013. Behaviour of clay-fouled ballast under drained triaxial testing, Géotechnique, **63**(5): 410-419.

Irving, J.D. and Knight, R. 2003. Removal of wavelet dispersion from ground-penetrating radar data, Geophysics, **68**(3): 960-970.

Jack, R. and Jackson, P. 1999. Imaging attributes of railway track formation and ballast using ground probing radar, NDT&E International, **32**(8): 457-462.

Jol, H. 2009. Ground penetrating radar theory and applications. Elsevier Science, Oxford, United Kingdom.

Kashani, H.F., Ho, C.L., Clement, W.P., and Oden, C.P. 2016. Evaluating the correlation between the geotechnical index and the electromagnetic properties of fouled ballasted track by a full-scale laboratory model, Transportation Research Record, **2545**: 66-78.

Khakiev, Z., Shapovalov, V., Kruglikov, A., and Yavna, V. 2014a. GPR determination of physical parameters of railway structural layers, Journal of Applied Geophysics, **106**: 139-145.

Khakiev, Z., Shapovalov, V., Kruglikov, A., Morozov, A., and Yavna, V. 2014b. Investigation of long term moisture changes in trackbeds using GPR, Journal of Applied Geophysics, **110**: 1-4.

Kind, T. 2011. GPR antenna array for the inspection of railway ballast. In National Seminar & Exhibition on Non-Destructive Evaluation, pp. 281-285.

Leng, Z. and Al-Qadi, I.L. 2010. Railroad ballast evaluation using ground-penetrating radar: Laboratory investigation and field vindication, Journal of the Transportation Research Board, **2159**: 110-117.

Lester, J. and Bernold, L.E. 2007. Innovative process to characterize buried utilities using ground penetrating radar, Automation in Construction, **16**: 546-555.

Li, D., Hyslip, J.P., Sussmann, T.R., and Chrismer, S.M. 2016. Railway geotechnics. Taylor & Francis Group LLC, Boca Raton, FL, USA.

Liu, L., Lane, J.W., and Quan, Y. 1998. Radar attenuation tomography using the centroid frequency downshift method, Journal of Applied Geophysics, **40**: 105-116.

Liu, X., Saat, M.R., and Barkan, C.P.L. 2012. Analysis of causes of major train derailment and their effect on accident rates, Transportation Research Record, **2289**: 154-163.

Mishra, D., Kazmee, H., Tutumluer, E., Pforr, J., Read, D., and Gehringer, E.:. 2013. Characterization of railroad ballast behavior under repeated loading: Results from new large triaxial setup, Transportation Research Record, **2374**: 169-179.

Nimbalkar, S., Indraratna, B., Rujikiatkamjorn, C., and Martin, M. 2012. Effect of coal fines on the shear strength and deformation characteristics of ballast. In 11th Australia - New Zealand Conference on Geomechanics: Ground Engeineering in a Changing World, Australia, pp. 451-456.

Olhoeft, G.R. 2005. Working in a difficult environment: GPR sensing on the railroads. In IEEE Antennas and Propagation Society International Symposium, Washington DC, USA, Vol. 3B, pp. 108-111.

Parsons, R.L., Rahman, A.J., Han, J., and Glavinivh, T.E. 2014. Track ballast fouling and permeability characterization by using resistivity, Transportation Research Record, **2448**: 133-141.

Plati, C., Loizos, A., and Papavasiliou, V. 2010. Inspection of railroad ballast using geophysical method, International Journal of Pavement Engineering, **11**(4): 309-317.

Prescott, D. and Andrews, J. 2015. Investigating railway track asset management using a markov analysis, Proceedings of the Institution of Mechanical Engineers, Part F: Journal of Rail and Rapid Transit, **229**(4): 402-416.

Prescott, D. and Andrews, J. 2013. A track ballast maintenance and inspection model for a rail network, Proceedings of the Institution of Mechanical Engineers, Part O: Journal of Risk and Reliability, **227**(3): 251-266.

Rail Safety and Standard Board Limited. 2011. Track system requirements. United Kingdom, London.

Roberts, R., Rudy, J., Al-Qadi, I.L., Tutumluer, E., and Boyle, J. 2006. Railroad ballast fouling detection using ground penetrating radar - A new approach based on scattering from voids. In Proceedings of the 9th European Conference on Non-Destructive Testing , Berlin, Germany, pp. 1-8.

Roghani, A. and Hendry, M.T. 2016. Continuous vertical track deflection measurements to map subgrade condition along a railway line: Methodology and case studies, Journal of Transportation Engineering, **142**(12): 04016059-1-04016059-8.

Sadeghi, J. 2010. Development of railway track geometry indexes based on statistical distribution of geometry data, Journal of Transportation Engineering, **136**(8): 693-700.

Sadeghi, J. and Askarinejad, H. 2011. Development of track condition assessment model based on visual inspection, Structure and Infrastructure Engineering: Maintenance, Management, Life-Cycle Design and Performance, **7**: 895-905.

Sadeghi, J. and Askarinejad, H. 2010. Development of improved railway track degradation models, Structure and Infrastructure Engineering: Maintenance, Management, Life-Cycle Design and Performance, **6**: 675-688.

Sadeghi, J. and Askarinejad, H. 2009. An investigation into the effects of track structural conditions on railway track geometry deviations, Proceedings of the Institution of Mechanical Engineers, Part F: Journal of Rail and Rapid Transit, **233**: 415-425.

Scanlan, K.M., Hendry, M.T., and Martin, C.D. 2017a. Evaluating the impact of ballast undercutting on the roughness of rack geometry over different subgrade conditions, Proceedings of the Institution of Mechanical Engineers, Part F: Journal of Rail and Rapid Transit, 1-11: DOI: 10.1177/0954409717720347.

Scanlan, K.M., Hendry, M.T., and Martin, C.D. 2016. Evaluating the equivalency between track quality indices and minimum track geometry threshold exceedances along a Canadian freight railway. Proceedings of the 2016 ASME Joint Rail Conference, April 12-15, Columbia SC, USA. DOI: 10.1115/JRC2016-5748.

Scanlan, K.M., Hendry, M.T., Martin, C.D., and Schmitt, D.R. 2017b. Evaluating the sensitivity of low-frequency ground-penetrating radar attributes to estimate ballast fines in the presence of variable track foundations through simulation, Proceedings of the Institution of Mechanical Engineers, Part F: Journal of Rail and Rapid Transit, 1-14: DOI: 10.1177-0954409717710408.

Selig, E.T. and Waters, J.M. 1994. Track geotechnology and substructure management. Thomas Telford Ltd., London.

Selig, E.T. and Li, D. 1994. Track modulus: Its meaning and factors influencing it, Transportation Research Record, **1470**: 47-54.

Shangguan, P. and Al-Qadi, I.L. 2014. Content-based image retrieval approaches to interpret ground penetrating radar data, Construction and Building Materials, **69**: 10-17.

Shangguan, P., Al-Qadi, I.L., and Leng, Z. 2012. Development of wavelet technique to interpret ground-penetrating radar data for quantifying railroad ballast conditions, Journal of the Transportation Research Board, **2289**: 95-102.

Shao, W., Bouzerdoum, A., and Phung, S.L. 2011a. Sparse signal decomposition for ground penetrating radar. In 2011 IEEE Radar Conference, Kansas City, MO, USA, pp. 453-457.

Shao, W., Bouzerdoum, A., Phung, S.L., Su, L., Indraratna, B., and Rujikiatkamjorn, C. 2011b. Automatic classification of ground-penetrating-radar signals for railway-ballast assessment, IEEE Transactions on Geoscience and Remote Sensing, **49**(10): 3961-3972.

Silvast, M., Nurmikolu, A., Wiljanen, B., and Levomaki, M. 2013. Identifying frost-susceptible areas on Finnish railways using the ground penetrating radar technique, Proceedings of the Institution of Mechanical Engineers, Part F: Journal of Rail and Rapid Transit, **227**(1): 3-9.

Silvast, M., Nurmikolu, A., Wiljanen, B., and Levomaki, M. 2010. An inspection of railway ballast quality using ground penetrating radar in finland, Proceedings of the Institution of Mechanical Engineers, Part F: Journal of Rail and Rapid Transit, **224**: 345-351.

Silvast, M., Levomaki, M., Nurmikolu, A., and Noukka, J. 2006. NDT techniques in railway structure analysis. In Proceedings of the 7th World Congress on Railway Research, Montreal, Canada, pp. 1-12.

Stockwell, R.G., Mansinha, L., and Lowe, R.P. 1996. Localization of the complex spectrum: The S transformation, IEEE Transactions on Signal Processing, **44**(4): 998-1001.

Su, L., Rujikiatkamjorn, C., and Indraratna, B. 2010. An evaluation of fouled ballast in a laboratory model track using ground penetrating radar, Geotechnical Testing Journal, **33**(5): 1-8.

Sussmann, T.R., Ruel, M., and Chrismer, S.M. 2012. Source of ballast fouling and influence considerations for condition assessment criteria, Transportation Research Record, **2289**: 87-94.

Sussmann, T.R., Selig, E.T., and Hyslip, J.P. 2003. Railway track condition indicators from ground penetrating radar, NDT&E International, **36**(3): 157-167.

Tennakoon, N. and Indraratna, B. 2014. Behaviour of clay-fouled ballast under cyclic loading, Géotechnique, **64**(6): 502-506.

Theune, U., Rokosh, C.D., Sacchi, M., and Schmitt, D.R. 2006. Mapping fractures with GPR: A case study from turtle mountain, Geophysics, **71**: B139-B150.

Tosti, F., Benedetto, A., Calvi, A., and Bianchini Ciampoli, L. 2016. Laboratory investigations for the electromagnetic characterization of railway ballast through GPR. In 16th International Conference of Ground Penetrating Radar (GPR), pp. 1-6.

Transport Canada. 2012. Rules respecting track safety. Canada, Ottawa.

Transportation Safety Board of Canada. 2016. Statistical summary - railway occurrences 2015 - data tables [online]. Available from http://www.bst-tsb.gc.ca/eng/stats/rail/2015/sser-ssro-2015-tbls.asp [cited 05/12 2017].

Turner, G. and Siggins, A.F. 1994. Constant Q attenuation of subsurface radar pulses, Geophysics, **59**(8): 1192-1200.

Warren, C., Giannopoulos, A., and Giannakis, I. 2016. gprMax: Open source software to simulate electromagnetic wave propagation for ground penetrating radar, Computer Physics Communications, **209**: 163-170.

Zong, N., Askarinejad, H., Heva, T.B., and Dhanasekar, M. 2013. Service condition of railroad corridors around the insulated rail joints, Journal of Transportation Engineering, **139**(6): 643-650.

Appendix A: Evaluating the Equivalency between Track Quality Indices and Minimum Track Geometry Threshold Exceedances along a Canadian Freight Railway

A.1. Contribution of the Ph.D. Candidate

All of the work presented in this appendix was performed by the Ph.D. candidate, including literature review, data processing, analysis, and interpretation as well as manuscript preparation. This chapter details a comparison between variable track geometry as inferred from regulated minimum safety threshold exceedances and from three track quality indices. As supervisors, Dr. M.T. Hendry and Dr. C.D. Martin reviewed all parts of the work. This chapter has been published with the following citation;

Scanlan, K.M., Hendry, M.T., and Martin, C.D. 2016. Evaluating the equivalency between track quality indices and minimum track geometry threshold exceedances along a Canadian freight railway. Proceedings of the 2016 ASME Joint Rail Conference, DOI: 10.1115/JRC2016-5748.

A.2. Abstract

Railway regulators require that track geometry measurements meet a specific set of minimum safety thresholds. A proper interpretation of track geometry survey data is fundamental for the detection of track exceeding these thresholds and in need of corrective maintenance. Irregular track geometry independent of the minimum safety thresholds can also be used as evidence of degradation in the railway foundation. Therefore, multiple evaluation methods must be applied to the track geometry survey data when assessing foundation degradation. In this study, we compare multiple track geometry evaluation methods in order to assess if they equally identify

sections of irregular track geometry along a 335 kilometer section of a Canadian freight railway. The track geometry evaluation methods investigated are the Transport Canada Class 5 minimum safety threshold exceedances and three literature-suggested track quality indices; the Overall Track Geometry Index, the Polish J Index and the Swedish Q Index. Furthermore, this study also investigates the ability of the track quality indices to provide additional insight into track geometry variability in sections without a minimum safety threshold exceedance. The track under investigation is not a Class 5, however, Class 5 minimum safety thresholds were used to produce enough threshold exceedances to allow for the comparison to the track quality indices. The results of the analysis reveal that while the large-scale variability in the three track quality indices is similar, the individual equivalency with the occurrence of Class 5 threshold exceedances is highly variable. Furthermore, only the Overall Track Geometry Index demonstrates the potential to provide consistent additional track geometry variability information.

A.3. Introduction

The continual maintenance of rail lines represents a significant capital investment for railway operators. In 2013 basic track renewal (maintenance) expenditures totaled $2.74 billion for the Canadian National (CN) Railway Company (Canadian National 2014). An efficient use of these capital resources is predicated on the ability to properly identify sections of track in need of maintenance. Basic track maintenance targets two dominant types of operational concerns; structural and geometrical track issues. Structural issues are those related to the conditions of the individual track components including rails, fasteners, ties and foundation materials (ballast, subballast and subgrade), which are not impacting track geometry (Sadeghi 2010). These types of issues are often identified through careful visual inspections (Sadeghi and Askarinejad 2010)

but may also be identified from the results of automated surveys (Clark 2004). Track geometry issues are those identified from the results of automated inspections of track orientations (Sadeghi 2010) that may be related to the degradation of components of the railway foundation such as crossties and ballast (Transport Canada 2012, Federal Railroad Administration 2014).

Track geometry must be controlled in order to limit both rail car accelerations and the risk of train derailments. In Canada, Transport Canada prescribes the minimum track geometry thresholds railway operators must satisfy for different classes of track (Transport Canada 2012). However, it is common for railway operators to employ tighter restrictions on track geometry compared to those specified by Transport Canada for the same class of track. The Transport Canada minimum safety thresholds are defined in terms of the track gauge, crosslevel, curve, alignment and surface geometry variables. The Transport Canada thresholds are the same as those prescribed by the Federal Railroad Administration (FRA) (Federal Railroad Administration 2014). Track gauge describes the difference in the distance between rail heads relative to the nominal distance of 1465 mm (56½ inches), while crosslevel describes the difference in elevation between the two rails. The curve track geometry variable is used to quantify the degree of curvature in a spiral or curved section of track in units of radians per kilometer. Track alignment and surface describe the deviation of individual rails from a straight line profile at the mid-chord position once the rail has been projected onto the horizontal and vertical planes respectively. Multiple chord lengths are used to quantify different alignment and surface variables. The track geometry thresholds prescribed by Transport Canada must be satisfied at every isolated position along a rail line. When an exceedance is detected, train speeds must be reduced until track maintenance has been performed and the measured track geometry no longer exceeds the minimum safety thresholds for that class of track.

Under ideal circumstances, the continuous measurement of track geometry will identify those sections where exceedances will occur, before the thresholds are actually exceeded, and preventative maintenance can be performed. However, when citing degradation of the track foundation, such as fouled ballast, track inspectors may use the existence of a 'geometry condition' as corroborating evidence. The FRA defines a 'geometry condition' as "… a track surface, gage, or alinement irregularity that does not exceed the allowable threshold for the designated track class." [Federal Railroad Administration 2014 – pg. 2.1.52]. Therefore, in order to characterize these 'geometry conditions', alternative track geometry interpretation methodologies that do not rely on exceedances of the regulated track geometry thresholds are required.

A number of track quality indices (TQIs) have been proposed based on the measured deviations in track geometry variables, including the surface, gauge and alignment, which attempt to provide a comprehensive indicator for track geometry behaviour (El-Sibaie and Zhang 2004, Sadeghi 2010, Sadeghi and Askarinejad 2010, Berawi et al. 2010). These TQIs statistically combine the standard deviations of multiple track geometry variables, defined over some constant length of track, into a single index value. Many of the TQIs provide specific index amplitude thresholds that are used to differentiate between sections of track where irregular track geometry may be a concern (implying the need for corrective track geometry maintenance) and those where it is not.

This study compares the occurrence of minimum safety threshold exceedances with the track geometry irregularities defined by the spatial TQI representations (specifically when TQI amplitudes exceed the defined maintenance-intervention thresholds). In addition, this study investigates the influence of varying the length of track used to define the various TQIs on this

relationship. The purpose is to quantify the similarity between the different track geometry analysis methods and determine if additional information regarding track geometry variability can be garnered by representing track geometry data as TQIs. The track geometry data used in this analysis are the results of a 2013 survey across a 335 km long section of freight railway with an annual load in excess of 50 million gross tons (GTM). This section of railway is comprised of Class 2, 3 and 4 track. As exceedances of the Transport Canada minimum safety standards are rare, the analysis of the track geometry was conducted based on Class 5 standards so as to produce enough threshold exceedances to allow for the comparison to the track quality indices.

A.4. Track Quality Indices

The equivalency between detected track geometry irregularities was evaluated using three different TQIs; the Overall Track Geometry Index (OTGI), the Polish J Index and the Swedish Q Index. The choice of which TQIs are to be compared is based on the availability of specific track geometry variables. Some TQIs require track geometry variables that are not recorded by Canadian railway operators and therefore cannot be calculated.

Sadeghi (2010) developed the OTGI as a comprehensive measure for track geometry conditions based on the observed tendency for track gauge, track twist as well as the 18.9 m (62-foot) alignment and surface geometry variables to follow a normal distribution when defined over a 250 m long length of track. Track twist is the difference in crosslevel between any two points separated by a distance less than or equal to a defined chord length. The normal distribution defined by the track geometry variables can then be accurately described by the mean and standard deviation. The mean ($\bar{x}$) and standard deviations (SD) for each track geometry variable are subsequently used to define five intermediate indices:

$$GI^{+} = \left|\bar{x}_{Gauge} + 3 * SD_{Gauge}\right| \quad \text{[Equation A-1]}$$

$$GI^{-} = \left|\bar{x}_{Gauge} - 3 * SD_{Gauge}\right| \quad \text{[Equation A-2]}$$

$$AI = \frac{1}{2} * \left(\left|\bar{x}_{LeftAlignment} + 3 * SD_{LeftAlignment}\right| + \left|\bar{x}_{RightAlignment} + 3 * SD_{RightAlignment}\right|\right) \quad \text{[Equation A-3]}$$

$$SI = \frac{1}{2} * \left(\left|\bar{x}_{LeftSurface} + 3 * SD_{LeftSurface}\right| + \left|\bar{x}_{RightSurface} + 3 * SD_{RightSurface}\right|\right) \quad \text{[Equation A-4]}$$

$$TI = \left|\bar{x}_{Twist} - 3 * SD_{Twist}\right| \quad \text{[Equation A-5]}$$

GI^{+}, GI^{-}, AI, SI, and TI are the positive and negative gauge index, the alignment index, the surface index and the twist index respectively. The intermediate track gauge index is split into positive and negative components to account for different wide and tight gauge tolerance limits. There are left and right components to the alignment and surface intermediate indices as these variables can be defined for the left and right rails individually. Once the individual intermediate indices are defined, the composite OTGI can be calculated using the following:

$$OTGI = \frac{\frac{a}{2} * GI^{+} + \frac{a'}{2} * GI^{-} + b * AI + c * SI + d * TI}{\frac{a+a'}{2} + b + c + d} \quad \text{[Equation A-6]}$$

The a, a', b, c, and d coefficients in Equation A-6 are constants assigned to each intermediate index based on the class of track under analysis. These weighting constants are estimated from the minimum safety thresholds for the each track geometry variable (Sadeghi 2010). Weights for track geometry variables with more restrictive minimum safety thresholds (tight track gauge for example) are larger than those associated with track geometry variables that are allowed to vary over a greater range (such as the track surface). The specific magnitude of each weight is derived from the size of the minimum safety threshold relative to the smallest minimum safety threshold of all track geometry variables considered during the calculation of the OTGI. Since the minimum safety thresholds vary as a function of track class, the OTGI weighting constants vary with track class as well. OTGI amplitudes differentiating between regular and irregular track geometry conditions are also based on the class of track. A complete record of coefficients and irregular geometry defining OTGI amplitudes can be found in Sadeghi (2010).

The Polish J Index is based on the same four track geometry variables as the OTGI; track gauge, alignment, surface and twist (Sadeghi 2010). However, where the OTGI incorporated an 18.9 m chord length in the calculation of the alignment and surface, the Polish J Index considers a 10 m chord length. Based on the standard deviation of these track geometry variables, the Polish J Index is calculated as follows:

$$J = \frac{SD_{Gauge} + SD_{Alignment} + SD_{Twist} + 0.5 * SD_{Surface}}{3.5} \quad \text{[Equation A-7]}$$

Note the significant similarity in the form of this equation for calculating the Polish J Index (Equation A-7) and that for the OTGI (Equation A-6).

Whether the calculated Polish J Index amplitude is indicative of irregular track geometry is dependent on the maximum train speed for the particular track (Sadeghi 2010). The Polish J Index amplitudes above which signify irregular track geometry are presented in Table A-1.

Table A-1. Maximum allowable Polish J Indices before maintenance is required as a function of train speed.

Train Speed (km/h)	30	40	90	120	160	200
Polish J Index	12.0	11.0	6.2	4.0	2.0	1.4

The final TQI considered in this analysis is the Swedish Q Index. This index is calculated using the following:

$$Q = 150 - \frac{100}{3} * \left[\frac{SD_H}{SD_{H,lim}} + 2 * \frac{SD_S}{SD_{S,lim}}\right] \quad \text{[Equation A-8]}$$

where SD_H represents the average standard deviation of the right and left rail surface geometry variables and SD_S represents the average standard deviation of the track gauge, crosslevel and alignment (left and right rail) geometry variables (Sadeghi 2010). The specified chord length used in the calculation of the surface and alignment geometry variables is 12 m. The $SD_{H,lim}$ and

$SD_{s,lim}$ are allowable standard deviation limits used to scale the SD_H and SD_S parameters calculated from the geometry survey data (El-Sibaie and Zhang 2004). The allowable standard deviations are speed dependent and are summarized in Table A-2.

Table A-2. Allowable standard deviations as a function of train speed for use in Swedish Q Index calculations.

Train Speed (km/h)	105-120	125-140	145+
$SD_{H,lim}$ [mm]	5	3	1
$SD_{S,lim}$ [mm]	9	7	6

The form of the equation for the Swedish Q Index (Equation A-8) is significantly different than that for either the OTGI (Equation A-6) or the Polish J Index (Equation A-7). Of note is that the Swedish Q Index amplitudes cannot exceed a value of 150. The greater the deviation from an index amplitude of 150, the greater the deviation in the SD_H and SD_S variables; thereby implying more variability the base track geometry measurements. Swedish Q Index amplitudes that do not imply the existence of irregular track geometry are those between 70 and 90 (Sadeghi 2010). All other index amplitudes outside of this range are indicative of irregular track geometry.

A.5. Analysis of the Track Geometry Data

The threshold exceedance records are not a true record of threshold exceedances as the class of track has been artificially increased to Class 5. Furthermore, it is important to note that the specific track geometry survey data used for this analysis were acquired in 2013 and are not representative of the current geometry conditions along the rail line.

The analysis begins by identifying the isolated locations along the rail line where the track geometry data exceed the Class 5 Transport Canada minimum safety thresholds. As mentioned previously, this is accomplished through the analysis of the track gauge, crosslevel, curve,

alignment and surface geometry variables. Alignments must be defined using both an 18.9 m and 9.4 m (31-foot) chord length, while surfaces are defined using an 18.9 m chord length only. Track curvature is used to differentiate between tangent and curved sections of track (spirals and curves) as the minimum track geometry thresholds are different in curved sections of track as compared to tangent sections.

In parallel with the identification of (Class 5) threshold exceedances, the 335 km of track geometry data were subdivided into smaller analysis bins and the three TQIs calculated. Ten different bin sizes were used in the calculation of the various TQIs, ranging from 25 m to 800 m in length. As the rail line is being interpreted as a Class 5 track, it is being interpreted as if the maximum train speed is between 120 km/h and 160 km/h, and that the subdivision is subjected to annual traffic loads in excess of 15 GTM, the railway under consideration is assigned a B1 classification according to the OTGI (Sadeghi 2010). Therefore, the OTGI calculation weights (a, a', b, c, and d) are equal to 0.25, 1.00, 0.25, 0.13 and 0.33 respectively, while irregular track geometry is not implied until the OTGI amplitudes exceed a threshold of 3.02. For the Polish J Index, as the allowable train speed falls between the classifications specified in Table A-1, the maximum allowable amplitude before irregular track geometry is determined through interpolation. Based on interpolation, Polish J Index amplitudes do not imply the existence of irregular track geometry until they exceed a threshold of 3.34.

Figure A-1 presents an example of the OTGI, Polish J Index and Swedish Q Index profiles for a 40 km long section of the railway under analysis. All TQIs are calculated with bin size of 250 m. From Figure A-1, it is clear that all TQI profiles return similar large-scale representations of track geometry conditions. Local maxima in the OTGI profile are located at similar positions as maxima in the Polish J Index as well as minima in the Swedish Q Index. Figure A-1 also

highlights the locations along the TQI profiles exhibiting irregular track geometry (falling within the darker portion of the individual profiles) as determined by the TQI thresholds. It is immediately evident that the majority of the OTGI amplitudes indicate irregular track geometry while the majority of the Polish J Index amplitudes do not. Locations where the OTGI amplitudes are below the 3.02 threshold can be found near the distances of 16 km, 18 km, 22 km and 29 km respectively.

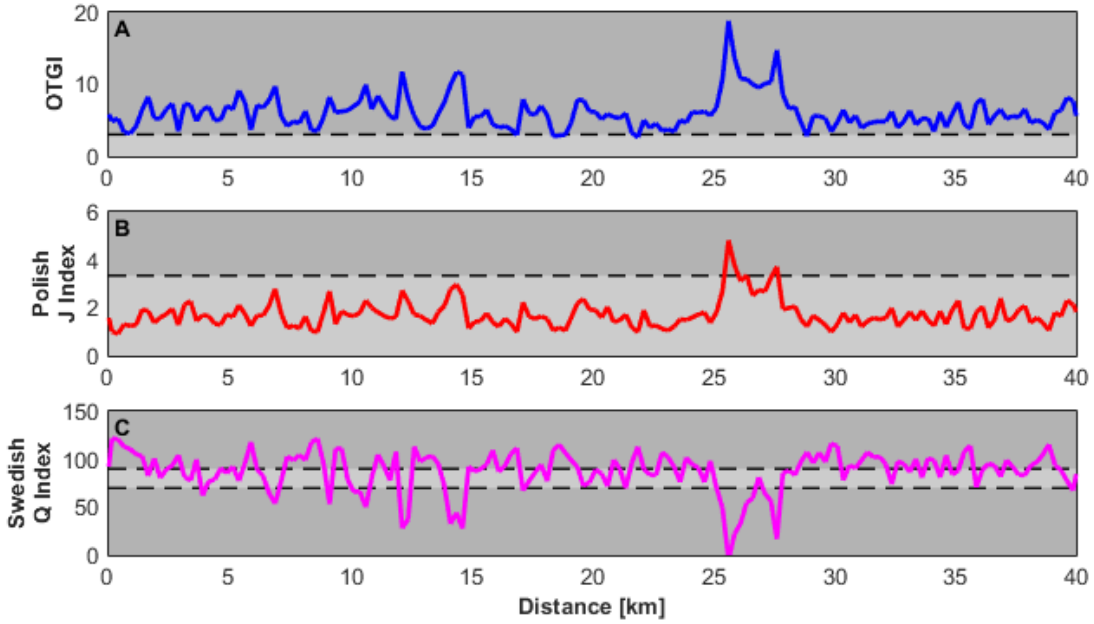

Figure A-1. Example TQI results for a 40 km section of the rail line under analysis; OTGI (a), Polish J Index (b) and Swedish Q Index (c). The darker shaded portions of each profile represent TQI amplitudes indicative of irregular track geometry.

Note that while all geometry variables required in order to calculate the OTGI are recorded during CN track geometry surveying, the specific Polish J Index and Swedish Q Index alignment and surface chord lengths are not. Recall, that the Polish J Index and the Swedish Q Index require the alignment and surface geometry variables be specified according to a 10 m and 12 m chord length respectively. During CN track geometry surveying, three chord lengths are used to

define the alignment and surface variables; 24.1 m (79-feet), 18.9 m (62-feet) and 9.4 m (31-feet). Due to the small difference in chord lengths, it is anticipated that the alignment and surface geometry variables acquired using a 9.4 m chord will not differ significantly from those that would be recorded with either a 10 m or 12 m chord. Therefore, the 9.4 m chord length alignment and surface geometry variables can be substituted during the calculation of the Polish J Indices and Swedish Q Indices without exhibiting a significant impact on the resulting index amplitudes.

A.6. Comparing Threshold Exceedances and TQI

Once the isolated threshold exceedances have been identified and the various TQIs calculated, using various lengths of track to define the standard deviations (bin lengths), the equivalency can be analyzed. As the threshold exceedances are based on Class 5 Transport Canada regulations, and where exceedances are identified corrective track geometry maintenance would be required if the railway was a Class 5 railway, this dataset provides an optimal comparative basis with which to assess equivalency. Therefore, the artificial minimum safety threshold exceedance dataset is treated as the base record of where track geometry irregularities exist. The degrees to which the various TQI representations conform to the base irregularity record are used to infer equivalency. An irregularity in the three TQI records is defined as an amplitude that exceeds the maintenance-implying threshold for that specific TQI.

An issue that must be considered is the spatial disparity between the threshold exceedances and the TQIs. Threshold exceedances are investigated at individual isolated positions, while the TQIs are the result of a spatial analysis of the track geometry data within each bin. As a result, the existence of a track geometry irregularity is judged at the bin size scale. If an isolated position within an individual TQI analysis bin does exceed the Class 5 Transport Canada minimum safety

thresholds, than that bin is labeled as containing a track geometry irregularity in terms of the Transport Canada regulations.

This mode of assessing equivalency results in four possible types of comparisons;

Type 1) (Class 5) Threshold exceedances and TQI amplitudes both imply the existence of a track geometry irregularity within the bin,

Type 2) (Class 5) Threshold exceedances and TQI amplitudes both do not imply the existence of a track geometry irregularity within the bin,

Type 3) No (Class 5) threshold exceedances exist within the bin while TQI amplitudes suggest the existence of irregular track geometry, and

Type 4) (Class 5) Threshold exceedances exist within the bin while TQI amplitudes suggest no track geometry irregularity.

For each of the Class 5 threshold exceedance-TQI comparisons, the analysis bin is categorized as belonging to one of these four types.

As the length of the individual bins varies between analyses, the total number of analysis bins varies as well. Therefore, in order to compare the relative proportion of bins belonging to each classification as a function of a changing bin length, the number of bins belonging to each type of comparison result is normalized. Normalization is accomplished by scaling the number of bins belonging to each type by the total number of bins that do contain a (Class 5) threshold exceedance (for Types 1 and 4) and those that do not (for Types 2 and 3). As a result, the pair of Type 1 and Type 4 percentages as well as the pair of Type 2 and Type 3 percentages sum to 100%.

It is important to note that, even when incorporating the more restrictive Class 5 minimum safety standards, bins within the subdivision that do contain a threshold exceedances are much less common than those that do not. Depending on the specific bin length, between 98.5% and 83.5% of the bins do not contain an (Class 5) threshold exceedance. The 98.5% is the percentage defined using a 25m-long bin length while the 83.5% is the percentage defined using an 800m-long bin length. Therefore, while the percentage of bins categorized as Types 1 and 4 and Types 2 and 3 both sum to 100%, in practice Type 2 and Type 3 bins are much more prevalent along the subdivision. Any perceived proportionality in the total length of track represented by the different percentages is then a function of the normalization and not directly indicative of the total length of track belonging to that classification type.

A.7. Results and Discussion

The percentages of bins belonging to the four category types previously described, as a function of bin size, are presented in Figures A-2, A-3 and A-4 for the OTGI, Polish J Index and Swedish Q Index respectively. The Type 1 and Type 3 curves are inverse mirror reflections of the Type 2 and Type 4 curves based on how the comparison results are classified and the process of normalization. As a result, trends in the Type 1 and Type 2 percentages are equal inverses of the trends in the Type 4 and Type 3 percentages. Otherwise stated, when a Type 1 percentage increases, it will do so at the expense of the Type 4 percentage and similar relationship exists between Type 2 and Type 3.

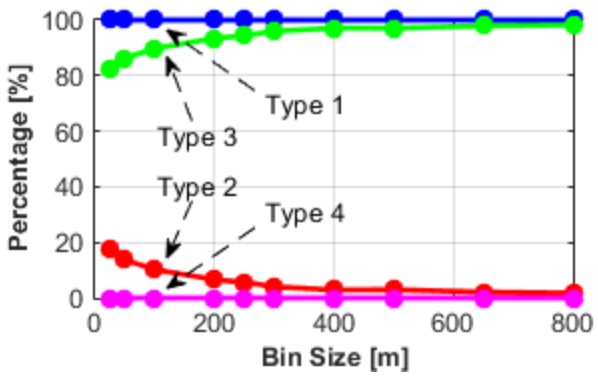

Figure A-2. Normalized percentages of OTGI bins belonging to each classification as a function of bin size.

From the OTGI results presented as Figure A-2, it is evident that there is only a minor influence of bin size on equivalency and the variability is limited to the smaller bin sizes only. The percentage of bins belonging to each of the four classifications does not strongly vary once the bin size reaches approximately 200 m in length. Recall that 250 m is the recommended length for defining standard deviations and means when calculating the OTGI (Sadeghi 2010). Figure A-2 also demonstrates that the OTGI perfectly replicates the profile of detected track geometry irregularities defined by the (Class 5) threshold exceedances, at all bin sizes. This is evidenced by the percentage of bins being classified as Type 1 and Type 4 being equal to 100% and 0% respectively. In addition, the OTGI also implies that track geometry irregularities can be found in more than 80% of the bins that do not contain an (Class 5) threshold exceedance (Type 3).

These results demonstrate that the OTGI is capable of detecting similar patterns of track geometry variability across bins, independent of whether an (Class 5) threshold exceedance exists or not. Therefore the OTGI provides additional insight into the track geometry conditions along the rail line when compared to the analysis of Transport Canada threshold exceedances only. However, as the majority of bins are implying the existence of irregular track geometry

when represented using the OTGI (Type 1 and Type 3), the ability to identify which individual sections may be influenced by the degradation of a particular component of the railway foundation (ballast, crossties etc.) is limited. A more focused discrimination, targeting the sections with the greatest track geometry variability, could possibly be achieved by increasing the OTGI threshold defining irregular track geometry.

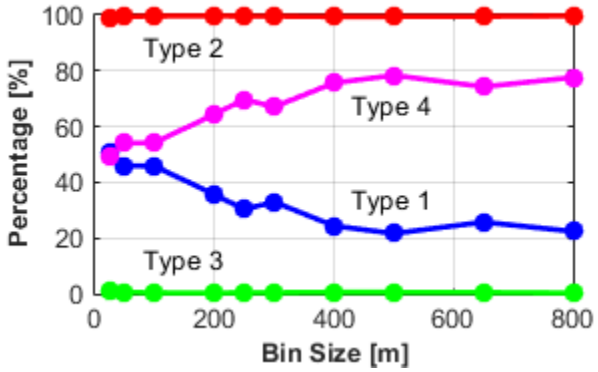

Figure A-3. Normalized percentage of Polish J Index bins belonging to each classification as a function of bin size.

In contrast to OTGI, the Polish J Index equivalency results (Figure A-3) do exhibit significant variation as a function of bin size. The percentage of bins belonging to Type 1 decreases as the bin size increases, while, in conjunction, the percentage of bins belonging to Type 4 increases. Therefore, bins containing track geometry irregularities defined by the Polish J Index equate less to those defined by (Class 5) Transport Canada minimum safety threshold exceedances when larger bin sizes are used. Even at the smallest bin size analyzed (25m), the Polish J Index recovers track geometry irregularities in only 50% of the bins that also contain at least one (Class 5) threshold exceedance. The Polish J Index maximizes the Type 2 percentage (neither the Class 5 safety thresholds nor the TQI imply the existence of a track geometry irregularity) at all bin sizes. As a consequence, the Type 3 percentage is minimized. Therefore, the Polish J Index

provides little additional track geometry variability insight. Where a more focused targeting of sections of track exhibiting the largest track geometry variation based on OTGI may be possible by increasing the OTGI threshold defining irregular track geometry, a similar approach for the Polish J Index may possible by decreasing the corresponding Polish J Index threshold.

Similar to the Polish J Index, the Type 1 and Type 4 Swedish Q Index equivalency results (Figure A-4) vary with bin size. For bin sizes less than or equal to 100m, the percentage of Type 1 bins is consistently greater than 80%. However, as the bin length increases from 100 m to 250 m the Type 1 percentage decreases to approximately 50% and remains within that range for all larger bin sizes. While the trends in the Swedish Q Index Type 1 and Type 4 percentages are similar to those observed in the Polish J Index, the Type 2 and Type 3 datasets mirror the behaviour observed for the OTGI; the Type 2 and Type 3 percentages exhibit little variation with changing bin sizes and the Type 3 percentage is maximized. Recall that a maximized Type 3 percentage is indicative of the TQI implying irregular track geometry in absence of (Class 5) threshold exceedances.

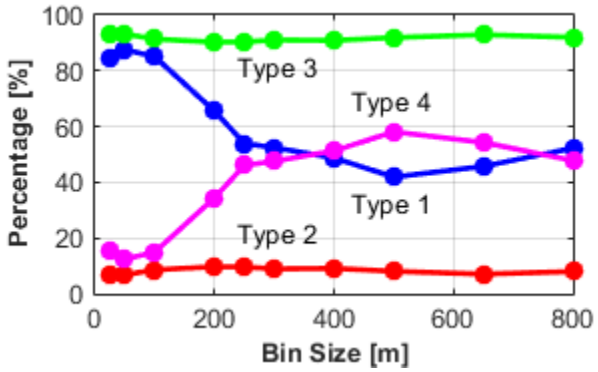

Figure A-4. Normalized percentages of Swedish Q Index bins belonging to each classification as a function of bin size.

These results demonstrate that the ability of the Swedish Q Index to yield additional track geometry variability information varies as a function of bin size. The Swedish Q Index implies the existence of irregular track geometry in many bins that do not contain an (Class 5) threshold exceedance (Type 3) at all bin sizes. This is beneficial at small (≤100m) bin sizes, where the Type 1 percentage is also maximized; thereby implying that the variability in the Type 3 bin is similar to the variability in bins containing a (Class 5) threshold exceedance (Type 1). When larger bin sizes are used, the Type 1 percentage decreases. While the Swedish Q Index still implies the existence of irregular track geometries in absence of (Class 5) threshold exceedances, the equivalency to bins containing a (Class 5) threshold exceedance is limited. Therefore, it is difficult to assess what additional information is being provided by the Swedish Q Index at larger bin sizes since the base track geometry irregularity record is not being reproduced.

A.8. Conclusion

Track geometry data recorded across a 335 km section of mainline track carrying an annual load of 50 GTM have been analyzed in terms of Class 5 Transport Canada minimum safety thresholds and three TQIs; the OTGI, the Polish J Index and the Swedish Q Index. This section of track analyzed is not Class 5 but the applied minimum safety thresholds have been artificially tightened to Class 5 standards in order to maximize the number of detected thresholds exceedances. The results demonstrate that the OTGI equates well with the (Class 5) threshold exceedance record and may be able to provide additional information identifying track geometry irregularities independent of length of track used to define the standard deviation and mean. Track geometry irregularities implied by the Polish J Index equate with, at most, half of the bins containing a (Class 5) threshold exceedance and the relationship worsens with increasing bin size. Furthermore, little additional track geometry variability insight is provided by the Polish J

Index. The Swedish Q Index equates well with the (Class 5) threshold exceedance record and appears capable of providing additional track geometry condition information at bin sizes less than 100 m in length. However, the equivalency and the ability to provide additional insight in track geometry variability quickly decreases with increasing bin length.

While the comparison of the results from the various methods incorporated only a single track geometry survey, similar trends and patterns have been observed in other surveys from both different years and different times of year. Furthermore, TQI-implied irregular track geometries are based on amplitude thresholds proposed in the literature. It is possible that a revision of these thresholds may yield improved equivalency results, a greater agreement between the Class 5 Transport Canada regulations and the TQIs as well as the improved identification of additional sections exhibiting irregular track geometry.

A.9. Acknowledgements

The funding for this work was provided by the Canadian Rail Research Lab (CaRRL). CaRRL is supported by the Natural Sciences and Engineering Research Council of Canada, CN, CP, AAR/TTCI, Transport Canada/NRC and Alberta Innovates. The author's wish to thank CN for providing the track geometry data and both Mr. Kevin Day and Mr. Tom Edwards for their insightful comments and critiques during the preparation of this manuscript.

A.10. References

Berawi, A.R.B., Delgado, R., Calçada, R., and Vale, C. 2010. Evaluating track geometrical quality through different methodologies, International Journal of Technology, **1**: 38-47.

Canadian National. 2014. 2013 annual report. Canadian National Railway Company, Montreal QC.

Clark, R. 2004. Rail flaw detection: Overview and needs for future developments, NDT&E International, **37**: 111-118.

El-Sibaie, M. and Zhang, Y. 2004. Objective track quality indices, Transportation Research Record, **1863**: 81-87.

Federal Railroad Administration. 2014. Track and rail and infrastructure integrity compliance manual. Federal Railroad Administration, Washington DC, USA.

Sadeghi, J. 2010. Development of railway track geometry indexes based on statistical distribution of geometry data, Journal of Transportation Engineering, **136**(8): 693-700.

Sadeghi, J. and Askarinejad, H. 2010. Development of improved railway track degradation models, Structure and Infrastructure Engineering: Maintenance, Management, Life-Cycle Design and Performance, **6**: 675-688.

Transport Canada. 2012. Rules respecting track safety. Canada, Ottawa.